Modelling and Numerical Simulation of Fluid Flow and Heat Transfer in Thermoplates

zur Erlangung des akademischen Grades eines
DOKTORS DER INGENIEURWISSENSCHAFTEN (Dr.-Ing.)
der Fakultät für Maschinenbau
der Univesität Paderborn

genehmigte
DISSERTATION

von
Dipl.-Ing. Boban Maletić
aus Bijeljina, Bosnien und Herzegowina

Tag des Kolloquiums:	20. Februar 2009
Referent:	Prof. Dr.-Ing. Jovan Mitrović
Korreferent:	Prof. Dr.-Ing. Eugeny Kenig

Contents

List of Publications

1. Mitrović, J. and Maletić, B., 2005, Effect of thermal assymetry on heat transfer in a laminar annular flow, Chemical Engineering and Technology, 28, 1144-1150.

2. Mitrović, J. and Maletić, B., 2006, Effect of thermal asymmetry on heat laminar forced convection heat transfer in a porous annular channel, Chemical Engineering and Technology, 29, 750-760.

3. Mitrović, J., Maletić, B. and Bačlić, B.S., 2006, Some peculiarities of the asymetric Graetz problem, International Journal of Engineering Science, 44, 436-455.

4. Mitrović, J. and Maletić, B., 2006, Numerical simulation of fluid flow and heat transfer in thermoplates, Proceedings of the 13th International Heat Transfer Conference IHTC-13, HEX-10, Sydney, Australia.

5. Mitrović, J. and Maletić, B., 2007, Heat transfer with laminar forced convection in a porous channel exposed to a thermal asymmetry, International Journal of Heat and Mass Transfer, 50, 1106-1121.

6. Mitrović, J. and Maletić, B., 2007, Numerical simulation of fluid flow, heat transfer and pressure drop in thermoplates, Proceedings of the 5th International Conference on Heat Transfer, Fluid Mechanics and Thermodynamics HEFAT2007, MJ3, Sun City, South Africa.

7. Mitrović, J. and Maletić, B., 2007, Numerical simulation of fluid flow and heat transfer in thermoplates, International Journal of Heat Exchangers, in Press.

8. Maletic Maletić, B. and Mitrović, J., 2008, Influence of the thermoplate geometry on the heat transfer, Proceedings of the 5th European Thermal-Sciences Conference EUROTHERM 2008, HEX27, Eindhoven, The Netherlands.

List of Figures

List of Tables

List of Symbols

Latin symbols

Symbol	Unit	Meaning
A	m^2	wall surface
A_n	$-$	constants
a	m	amplitude, plate width
$a_{i,j}, a_P, a_{nb}$	different	coefficients in discretised equations
b	m	plate spacing
C	$-$	constant
C_r	$-$	Courant number
c_p	$\mathrm{J{\cdot}kg^{-1}{\cdot}K^{-1}}$	specific heat capacity at constant pressure
c_v	$\mathrm{J{\cdot}kg^{-1}{\cdot}K^{-1}}$	specific heat capacity at constant volume
D, D_n	$-$	constants
d	m	average plate distance
d_h	m	hydraulic diameter
E_n	$-$	constants
${}_1F_1(x, y, z)$	$-$	hypergeometric function
$\boldsymbol{f}$	$\mathrm{m{\cdot}s^{-2}}$	gravitational force vector
H	m	height
$H(x)$	-	Heaviside step function
$H_x(y)$	$-$	Hermite polynomial
h	$\mathrm{W{\cdot}m^{-2}{\cdot}K^{-1}}$	heat transfer coefficient
h_m	$\mathrm{W{\cdot}m^{-2}{\cdot}K^{-1}}$	average heat transfer coefficient
i, j, k, l, m	-	summation indices
i	$\mathrm{J{\cdot}kg^{-1}}$	specific internal energy
k	$\mathrm{W{\cdot}m^{-1}{\cdot}K^{-1}}$	thermal conductivity, iteration number
L	m	length, half of the wave-length
l	m	cell length
M	$\mathrm{kg{\cdot}kmol^{-1}}$	molar mass
M	$-$	number of boundary cell faces
m	kg	mass
$\dot{m}$	$\mathrm{kg{\cdot}s^{-1}}$, $\mathrm{kg{\cdot}h^{-1}}$,	mass flow rate
N	$-$	total number of welding spots, number of numerical cells
Nu	$-$	Nusselt number

Symbol	Unit	Meaning
n	m	coordinate normal to the surface
$\boldsymbol{n}$	$-$	normal vector
P	W	pumping power
Pe	$-$	Péclet number
Pr	$-$	Prandtl number
p	Pa, bar	pressure
$\dot{\boldsymbol{Q}}$	W	heat flow rate
$\dot{\boldsymbol{q}}$	$\mathrm{W{\cdot}m^{-2}}$	heat flux vector
R	m	welding spot radius
Re	$-$	Reynolds number
S	$\mathrm{m^2}$	cross-sectional flow area
s_L	m	distance between welding points in x-direction
s_T	m	distance between welding points in x-direction
T	K	thermodynamic temperature
t	s	time
U	m	circumference
$\bar{u}$	$\mathrm{m\ {\cdot}s^{-1}}$	average velocity component in x-direction
u, v, w	$\mathrm{m\ {\cdot}s^{-1}}$	components of the velocity vector $\boldsymbol{w}$
$\tilde{u}^*,\ \tilde{v}^*$	$\mathrm{m{\cdot}s^{-1}}$	initial guess velocity components
V	$\mathrm{m^3}$	Volume
$\dot{V}$	$\mathrm{m^3{\cdot}s^{-1}}$	volume flow rate
$\boldsymbol{w}$	$\mathrm{m{\cdot}s^{-1}}$	velocity vector
$\bar{w}$	$\mathrm{m{\cdot}s^{-1}}$	average velocity component in z-direction
x, y, z	m	coordinates
X, Y, Z, Z_*	$-$	dimensionless coordinates
x_0, z_0	m	coordinates of the welding spots centres
Z_{A*}	$-$	dimensionless coordinate of the vertical asymptote
Z_{0*}	$-$	dimensionless coordinate of the adiabatic point

Greek symbols

α	$-$	weighting parameter, $0 \leq \alpha \leq 1$
δ	m	maximal plate distance
ε	m	width of the numerical cell in x-direction
Θ	$-$	dimensionless temperature
$\bar{\Theta}$	$-$	average dimensionless temperature
ϑ	°C	temperature
$\bar{\vartheta}$	°C	average temperature
κ	$\mathrm{m^2{\cdot}s^{-1}}$	thermal diffusivity

Symbol	Unit	Meaning
λ	$-$	tolerance
λ_n	$-$	eigenvalues
μ	Pa· s	dynamic viskosity
ν	m^2/s	kinematic viskosity
ξ	m	coordinate
$\pi = 3.141...$	$-$	Ludolph's constant
ρ	$kg{\cdot}m^{-3}$	density
$\boldsymbol{\tau}$	Pa	stress tensor
Φ	s^{-2}	dissipation funktion
ϕ	$-$	general scalar variable
$\varphi_n(X)$	$-$	eigenfunctions
φ	$^\circ$	phase shift angle
ω_n	$-$	n^{th} rooth of the equation $tan(\omega) = \omega$

Subscripts

A	vertical asymptote
i, I	summation index
IN	value at the inlet
j, J	summation index
L	longitudinal, spacing in x-direction
m	average value
n	summation index
nb	neighbouring cells
OUT	value at the outlet
S	a narrow strip of the thermoplate surface $y = f(x, z)$
$SW1$	a narrow strip of the lower thermoplate surface
$SW2$	a narrow strip of the upper thermoplate surface
T	transversal, spacing in z-direction
W	value at the wall
$W1$	value at the lower wall, $X = -1$ or $y = -f(x, z)$
$W2$	value at the upper upper wall, $X = +1$ or $y = +f(x, z)$
0	adiabatic point
∞	value in the fully developed region

Symbol	Unit	Meaning

Superscripts

0		value at starting time level t
$*$		initial guessed value

1 Introduction

Thermoplates are efficient heat transfer devices, which are used in several branches of engineering practice, e.g. as condensers or evaporators in thermal process technology and cooling technique. In comparison to shell-and-tube heat exchanges, their installation is relatively simple, and the periphery is drastically reduced.

A thermoplate consists of two metallic sheets, which are spot-welded over the whole surface according to an appropriate pattern, whereas the edges - except for connecting tubes - are continuously seam-welded. By applying a hydro-form technique, a channel having a complex shape is established between the sheets. One fluid is conducted through this channel, the other one through the channel created by two neighbouring thermoplates that are assembled in parallel at certain spacing thus making a thermoplate heat exchanger. The complex geometry of the inside channel of such a plate provides the flowing fluid a pronounced three-dimensional character.

In the simulations, the geometrical parameters, such as the welding pattern, the surface shape, the streamwise welding spots pitch, s_L, the transversal pitch, s_T, and the maximal distance between the metallic sheets, δ, have been varied, whereas the radius, R, of the welding spots and the channel length, L, were kept constant. The Reynolds number, Re, that is, the fluid inlet velocity, u_{IN}, and the distance, δ, has also been varied. The fluid inlet temperature, T_{IN}, and the wall temperature, T_W, were taken to be constant.

A parallel plate channel, and from some points of view, its equivalents, duct flow and annular gap, can be considered as the simplest thermoplate having even walls. Although a fabrication of such a channel without welding spots seems scarcely possible in sizes required in common practice, the parallel plate channel will serve in this work as a model for comparison with thermoplates.

The fluid flow was considered to be laminar, incompressible, at steady-state and three-dimensional. Water of constant physical properties is adopted for the numerical experiments. The velocity and the temperature fields are governed by the equations of continuity, momentum and energy.

The objective of the numerical experiments is to numerically obtain the sets of the geometrical parameters that, in interaction with process parameters, should pave the way for optimal heat transfer of the inside fluid which is assumed to pass the thermoplate as a single phase.

For the case of fluid flow and heat transfer in a parallel plate channel it was possible to find an analytical solution to the energy equation. In this connection the Mathematica software was used. In the numerical simulations of fluid flow and heat transfer in thermoplates, the commercial software StarCD was employed. The calculations have largely been performed on the PC^2 Paderborn center for parallel computing.

2 State of the Art

2.1 Thermoplates

A thermoplate considered in this work consists of two metallic sheets of the same thickness, which are spot-welded over the whole surface area according to an appropriate pattern, whereas the edges - except for connecting tubes - are continuously seam-welded. By applying a hydro-form technique, a channel having a complex shape is established between the sheets, Figure 2.1. One fluid (working fluid) is conducted through this channel, the other one (process fluid) through the channel confined by two neighbouring thermoplates.

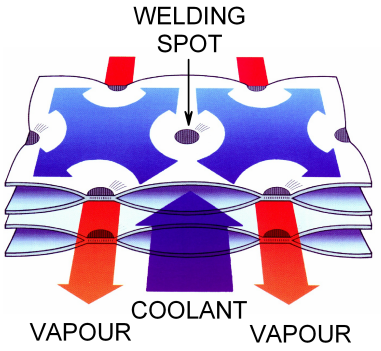

Figure 2.1: Fluid flow arrangement in thermoplates (DEG-Engineering [64]).

Different types of thermoplates were defined by Behrend [3], Figure 2.2. If the metallic sheets are of the same thickness, the so-called double embossed thermoplate is generated. The single embossed thermoplate is developed using the metallic sheets of different thicknesses, where only the thinner sheet is deformed due to hydroforming, while the other, thicker one, remains even. More than two sheets can also be used thereby producing thermoplates of very complex geometry, types triple and quadro. In the case that the firm sheets are to be used, or have to be thicker for some reasons, the hydro-form technique is not suitable anymore, and the plates are to be pre-formed, i.e. dimpled, before they are welded. Depending on its shape and use, thermoplates are named by some producers: immersion plates, clamp-on plates, pillow plates, plate coils and so on.

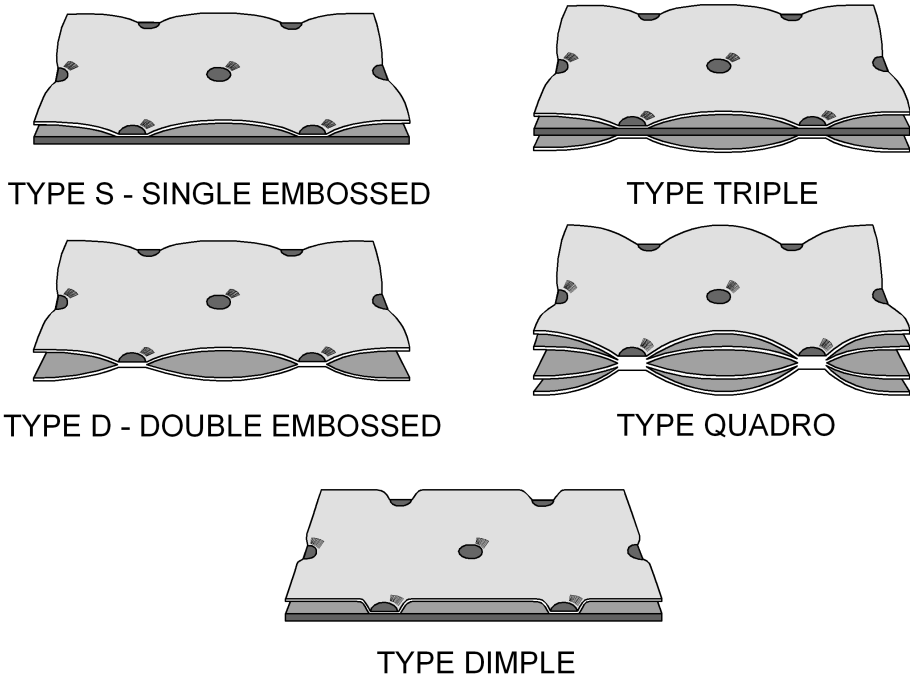

Figure 2.2: Different types of thermoplates, Behrend [3].

A number of thermoplates can be assembled in parallel at certain spacing thus making a thermoplate bank assembly or a thermoplate heat exchanger, Figure 2.3.

Such heat exchangers are encountered in several branches of engineering practice, e.g. as condensers or evaporators in thermal process technology and cooling technique and in recirculating systems where automatically controlled temperatures are needed. They are also used in any industries, where cooling or heating in a restricted space is required, such as: dairy industry, chemical industry, wine or chocolate industry, etc. Because of very low pressure drop of the fluid, usually vapour, that flows around the thermoplates, their use as head condensers of distillation plants is especially suitable,

Figure 2.3: Thermoplate assembly (OMEGA heat transfer technology [66]).

see the contribution of Mühlthaler [39], Figure 2.4.

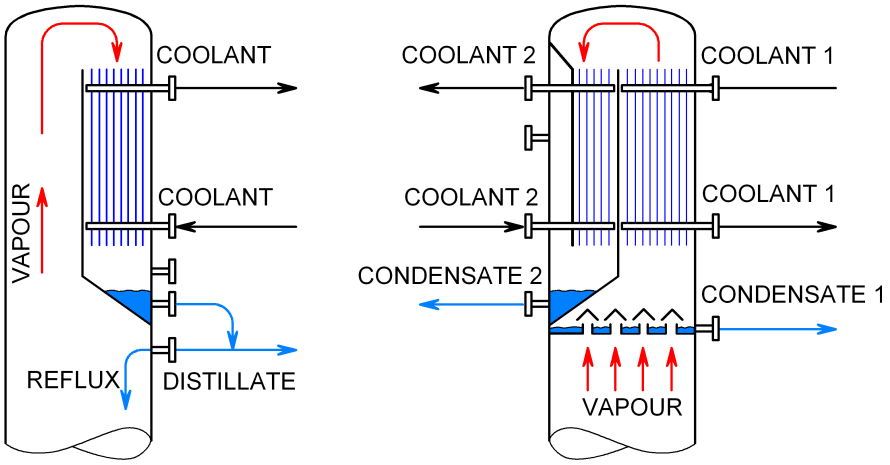

Figure 2.4: The use of thermoplate heat exchangers as a head condenser, Mühlthaler [39].

Both fluid spaces in the heat exchanger of this type are completely separated. The thermoplate heat exchangers, by some manufacturers also called plate-and-shell heat exchangers, are similar to the plate-and-frame heat exchangers, Figure 2.5, by name, but from the constructional point of view they are more similar to the shell-and-tube heat exchangers. Unlike other plate heat exchangers (Figure 2.5), the plates of the thermoplate heat exchangers do not touch each other, they are self-supporting and do not cause any forces, that have to be carried by the next plate or housing, Figure 2.3. Because of fully welded construction there are usually no gasket problems, which makes this type of heat exchangers suitable for high pressure applications. In comparison to shell-and-tube heat exchangers, their installation is relatively simple, and the periphery is drastically reduced for the same heat exchanger duty.

One big disadvantage of thermoplates lies in the fact that their thermo-fluid characteristic is scarcely explored, which prevents a reliable design of the corresponding heat exchangers. All literature contributions concerning thermoplates can be classified into three main groups: parallel plate channel, two-dimensional models and three-dimensional models.

2.2 Parallel plate channel

A parallel plate channel, and from some points of view, its equivalents, duct flow and annular gap, can be considered as the simplest thermoplate having even walls. Although a fabrication of such a channel without welding spots seems scarcely possible in sizes

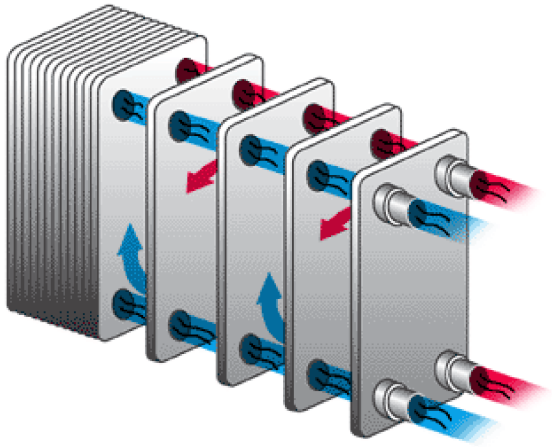

Figure 2.5: Plate-and-frame heat exchanger, (GEA FlatPlate Inc. [65]).

required in common practice, the parallel plate channel will serve in this work as a model for comparison with thermoplates. The fluid flow in this case is assumed to be a single-phase laminar forced convection.

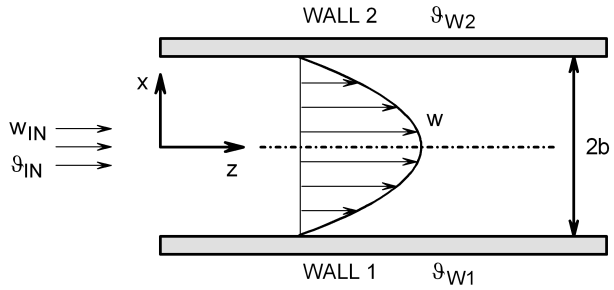

Figure 2.6: Fluid flow through a parallel plate channel.

The interest in this classical problem originates from an article by Graetz [15], who assumed a Poiseuille flow through a duct and a constant wall temperature and found an analytical solution of this heat transfer situation that was later called the symmetric Graetz problem. There are several monographs dealing with various formulations of the classical Graetz problem, e.g., by Petukhov [50], Shah and London [59], and Kakaç et al [23]. As can be taken from these monographs, the plane asymmetric Graetz problem when one plate is isothermal and the other one adiabatic was the topic of many papers. Both thermally developed and developing flows were analysed and positive and negative Nusselt numbers were observed. Such conditions, however, are rarely encountered in common practice.

There are only few papers dealing with a developing laminar flow bordered by walls of constant, but different temperatures, what is called the asymmetric Graetz

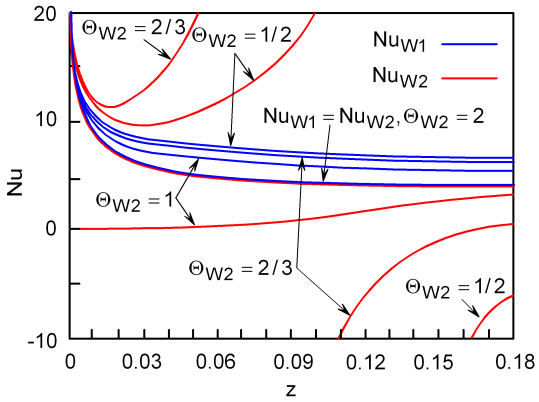

Figure 2.7: Distribution of Nusselt number allong a parallel plate channel, Hatton and Turton [19].

problem in this work, Figure 2.6. Hatton and Turton [19] solved the energy equation by separation of variables for eigenvalues in the thermally developing region of the laminar flow through a parallel plate channel, where the walls are kept at different temperatures, with the Poiseuille's velocity field. In the paper, it is shown that the Nusselt number of one plate can jump from infinite positive to infinite negative becoming zero further downstream and again positive, Figure 2.7. However, the authors did not show how the positions where the Nusselt number is infinite and zero depend on the boundary conditions. Furthermore, neither the conditions for this behaviour to establish nor the case of a small thermal asymmetry have been investigated. Such data are unavoidable for calculating the heat transfer under these conditions. A detailed study of the asymmetric Graetz problem which includes the effects, that have not been analysed in the literature yet, will be shown in Chapter 3. Some important details of that study were published by Mitrović, Maletić and Bačlić [32].

The same heat transfer situation in an annular gap was treated numerically by Mitrović and Maletić [33], where not only the boundary conditions in form of the fluid and wall temperatures, but also the radii ratio of the annulus has a big influence on the heat transfer.

2.3 Two-dimensional wavy channel

A considerable amount of contributions on methods that improve the heat and mass transfer in compact exchange devices can be found in the literature. The objective of these methods is mostly to interrupt the boundary layer formed on the wall surface by bringing the fresh fluid from the core into the near wall region, thereby increasing the temperature and concentration gradients at the wall. Some examples of such techniques are off-set fins, louvers, vortex generators, communicating channels, acoustic excitation

of the flow, oscillatory inflow, use of wavy wall channels etc. The optimal solution is the one with the lowest pressure drop but the largest heat and mass transfer rate. However, also other criteria such as ease of production and scaling have to be considered in particular cases [70].

Channels with wavy walls are easy to fabricate and provide significant heat and mass transfer enhancement if operated in an appropriate range of the Reynolds number. Therefore, the wavy wall channels and pipes, Figure 2.8, have been considered in several studies as means of the heat and mass transfer enhancement, both numerically and experimentally. It is observed, that the heat transfer enhancement can not be achieved at low Reynolds numbers. On the other hand, if the flow is made unsteady, either through external forces or through natural transition to an unsteady state, a significant increase of heat transfer is possible [70].

The flow of a viscous fluid through axially symmetric pipes and symmetrical wavy channels under Stokes flow conditions was first treated analytically by Burns and Parks [6]. The solution, used to calculate the flux through the channel wall for a given wave velocity or pressure gradient, was obtained by expressing the stream function as a Fourier series. Using a simple perturbation approach and collocation method, Selvarajan et al. [57] developed a numerical procedure for the analysis of the incompressible flow through a channel whose walls describe a travelling wave motion. The flow asymmetry was observed even for very low Reynolds numbers. Deiber and Schowalter [10] analysed flow of an incompressible Newtonian fluid through a wavy walled tube. Good agreement between their numerical and experimental predictions of friction factor as a function of Reynolds number was achieved. Similar results are given by Ralph [51].

Flow characteristics in a symmetrical channel with wavy walls were investigated both numerically and experimentally by Nisimura et al. [46]. Up to $Re = 350$ the symmetrical flow was observed. Stable twin vortices are formed at the maximum cross section, where the convective mixing between the mainstream and the vortex hardly occurs and the separation and reattachment points are fixed. The situation is completely different at larger Reynolds numbers, where the mainstream is disturbed by the unsteady vortex motion. For the analysed channel geometry, the authors noted that laminar flow exists at Reynolds numbers less than 350, and an increase of the Reynolds number causes turbulent flow to develop. Separation characteristics in a channel of the same geometry studied Mahmud et al. [28] numerically. A critical Reynolds number, from which the streamlines start to separate from the wavy wall surface for the given geometrical parameters, was proposed. According to their results, the critical Reynolds number falls rapidly with the increase of the surface waviness. Some profiles of the axial velocity component for two different Reynolds number are qualitative compared in Figure 2.9. At $Re = 200$ velocity profiles with negative gradient are observed, wich indicates a flow reversal. Kim [24] visualised the flow through the wavy channel using PIV (Particle Image Velocimetry) method, Figure 2.10.

Nishimura et al. [42] investigated experimentally the flow patterns and mass transfer characteristics in symmetrical two-dimensional channels with sinusoidal and arc-shaped

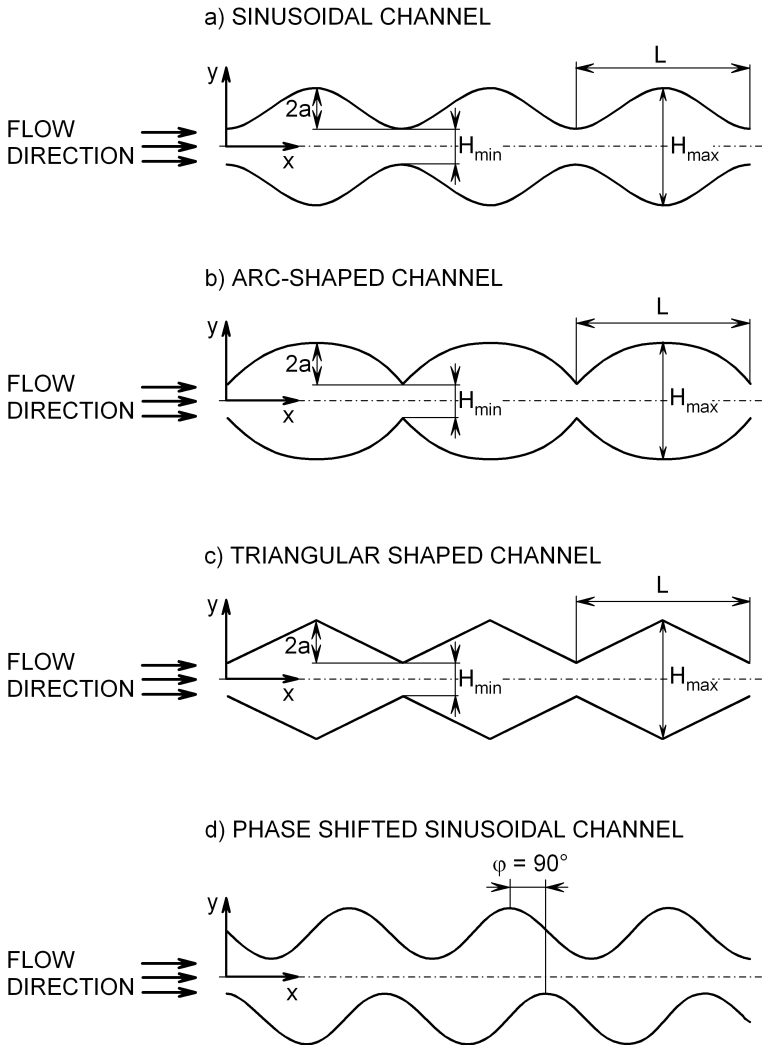

Figure 2.8: Different types of wavy channels.

walls, Figure 2.8a and b. The flow through arc-shaped channels is characterised by flow separation in each furrow, which leads to an earlier transition from laminar to turbulent flow in comparison to wavy channels. The flow separation implies a renewal of the boundary layers thus yielding the mass transfer enhancement. The arc-shaped wall has a larger mass transfer rate than the sinusoidal one because of an earlier transition to turbulence. Although the both channel geometries, the sinusoidal and the arc-shaped one, are taken to be two-dimensional, a regular three-dimensional flow is observed. Ničeno and Nobile [40] investigated numerically fluid flow and heat transfer in channels of the same geometries as used by Nishimura et al. [42] and confirmed their experimental results. Using a time-accurate, unstructured covolume method, they found that the heat transfer augmentation was only possible in unsteady regimes. Compared to the sinusoidally shaped channel, the heat transfer increase for the arc-shaped passage was

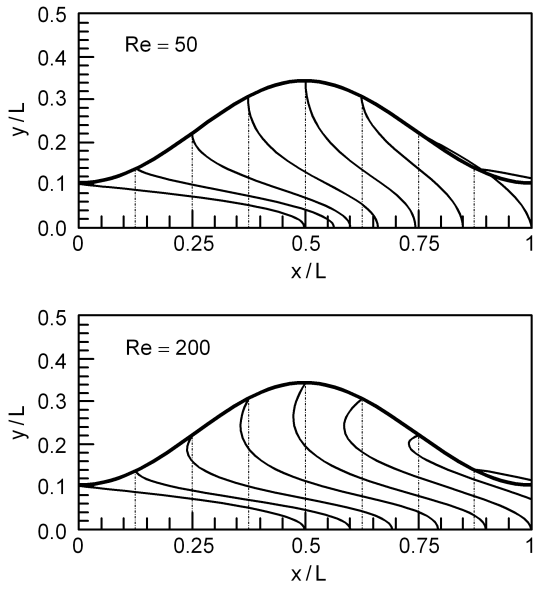

Figure 2.9: Axial velocity profiles at two different Reynolds numbers for $a/H_{max} = 0.175$ and $L/H_{max} = 1.5$, Mahmud et al. [28].

higher. However, the friction factor was also higher than that of the sinusoidal channel. Reports on similar experiments in a sinusoidal wavy walled tube were made in a further paper by Nishimura et al. [43]. As they found, the laminar-like flow and turbulent-like flow alternatively appear in transitional flow regime, indicating an intermittent flow behaviour. The increment in mass transfer in this flow regime was larger for the wavy tube than for the wavy channel.

Stone and Vanka [63] analysed a wavy channel consisting of 14 waves. They solved the Navier-Stokes equations governing a time-dependent flow and found out that the flow was steady for low Reynolds numbers, but increasing it beyond a modest value,

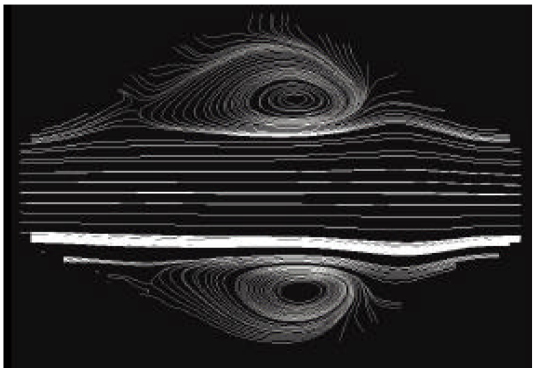

Figure 2.10: Mean streamlines at $Re = 500$ visualised by using PIV method, Kim [24].

the flow became unsteady. In this case the increased mixing between the core and near-wall fluid resulted in enhanced heat transfer and pressure drop. Hossain and Islam [21] studied sine-shaped wavy channels numerically by solving two-dimensional Navier-Stokes and energy equations implementing periodic boundary conditions. They found that the flow was steady up to a critical Reynolds number depending on the channel geometry, which confirms the results of Stone and Vanka [63]. Their results show further that decreasing channel height and increasing amplitude cause the flow to become more unstable resulting in higher heat transfer and pressure drop, but variation of wavelength has weak effect. The best heat transfer enhancement is achieved in the transitional regime. Furthermore Hossain and Islam [22] investigated numericaly in the same way the channels with sinusoidal, triangular and arc-shaped walls, Figure 2.8a, c and b, and compared them. Their results show that in the arc-shaped channel the transition between laminar and turbulent flow starts at a relatively low Reynolds number, for the sine-shaped channel it is relatively high, and for triangular channel it is in between these two. The comparison of all three channels was not possible in the same region of the Reynolds number, since the solutions for arc and triangular channels become divergent after certain Reynolds number, with the code they used. Similar study of the converging-diverging tube conducted Sparrow and Prata [61]. They adopted periodic boundary conditions in numerical experiments and achieved a very good agreement with experiments. In comparison to the straight tube, the heat transfer enhancement in corrugated tube was possible only for Prandtl numbers greater than 2.5. Wirtz et al. [72] investigated air flow though a grooved channel experimentally. The Nusselt number of the windward face was approximately twice that of the leeward face.

Russ and Beer [53] investigated a pipe with sinusoidal wavy surface, both numerically and experimentally in laminar, transitional and turbulent flow regime. The numerical and the experimental results are in good agreement, except for the transitional flow regime. The positions of the minima and maxima of the Sherwood and Nusselt numbers nearly coincide with the flow separation and the reattachment point, respectively. Saniei and Dini [55] conducted an experimental study of convective heat transfer in the turbulent regime in a wavy channel. The highest magnitude of the local Nusselt number was on the second wave and its local maxima were located upstream of the peak of each wave. The average Nusselt number of the wavy channel was always higher than the one of the even channel for the Reynolds number range. Wang and Vanka [70] studied the flow patterns and heat transfer characteristics in a sinusoidally curved converging-diverging channel numerically. Implementing a curvilinear orthogonal grid they got accurate numerical solutions. For Reynolds numbers below 180 steady laminar flow was established, while beyond this value a transition to chaotic flow with significant increase in heat transfer was observed. Laminar flow and heat transfer in a sinusoidally curved converging-diverging channel were analysed by Garg and Maji [14] using a finite difference method for solving the conservation equations. They show that the flow separates mainly in the diverging region. However, for higher Reynolds number and amplitude-wavelength ratio the flow separates in the converging region as well. The pressure distribution in the axial direction is a combination of a nearly linear and

periodic function. The pressure drop in the fully developed region is constant for each cycle and increases with Reynolds number and amlitude-wavelength ratio. The Nusselt number increases with Reynolds number as well, which is not the case in a parallel plate channel. The analysis of the same physical problem, but inside a sinusoidal wavy tube was conducted by Mahmud et al. [28] using the Finite-Volume method. They propose a correlation for calculating the friction factor as a function of surface waviness and Reynolds number. The surface waviness was formed to cause earlier flow separation, larger pressure drop and higher heat transfer rate. Heat transfer and entropy generation in a wavy channel under the influence of inclination was studied by Mahmud and Islam [29] for the case of laminar free convection and the walls having different temperature. The distributions of the average Nusselt number and of the average entropy generation number have bin given. However, the angle of inclination is not expected to have any essential effect on forced convection fluid flow.

Turbulent flow through the wavy wall channel and convective heat transfer were investigated by Dellil et al. [11]. As they reported, the two-layer model they implemented (the standard k-ε turbulence model combined with a one-equation model to resolve the near-wall viscosity-affected regions) was successful in capturing most of the important physical features of a turbulent flow with reasonable amount of memory storage and computer time. The results of their simulations show that the minimum and the maximum Nusselt numbers are located near the separation and the reattachment points, respectively, which supports the results of Russ and Beer [53]. The average Nusselt number increases with the wave amplitude until a critical value, after which it remains largely constant. However, the heat transfer enhancement is accompanied by an increase in the pressure drop.

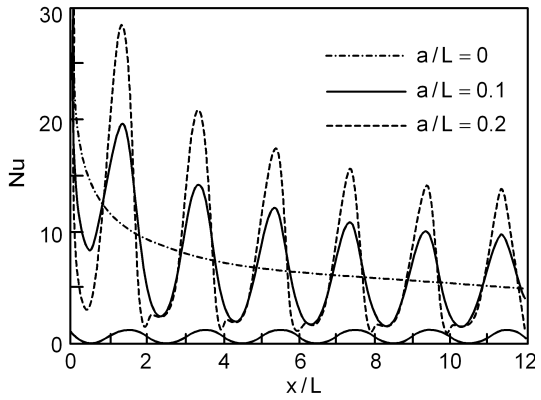

Figure 2.11: Distribution of the local Nusselt number for $Re = 500$ and $Pr = 6.93$, [69].

A very comprehensive and detailed study of a laminar forced convection in a wavy wall channel is given in a paper by Wang and Chen [69]. A simple coordinate transformation method was employed to transform the wavy channel into a parallel plate

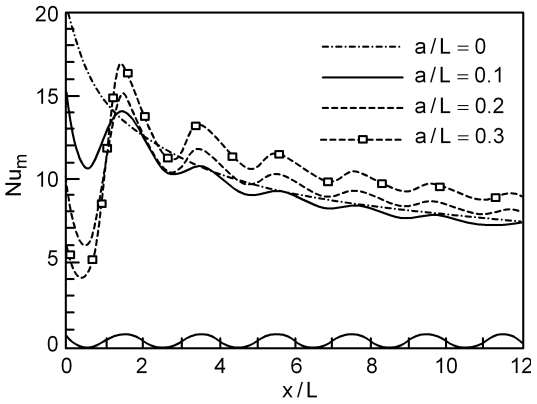

Figure 2.12: Distribution of the average Nusselt number for $Re = 500$ and $Pr = 6.93$, [69].

channel. Effects of the waviness, Reynolds number and Prandtl number on the local friction coefficient and Nusselt number were investigated. Their results show that the channel forms a highly complex flow pattern, which comprises a strong forward flow and an oppositely directed recirculating flow with each wave. The harmonic distribution of the Nusselt number has the same frequency as the wavy surface, Figure 2.11. The maxima occur in the converging section of each wave near the minimal cross-section of the channel and its positions are independent of the amplitude-wavelength ratio and the Reynolds number, Figures 2.11 to 2.13. The minima of the local Nusselt number are located downstream and upstream within a short distance of the largest cross-section of each wave. With an increase in the Reynolds number, the maxima of the Nusselt number and of the friction coefficient increase in each converging channel position, but its minima remain almost constant in the diverging section. Similar distributions of the Sherwood number obtained Nishimura et al. [47].

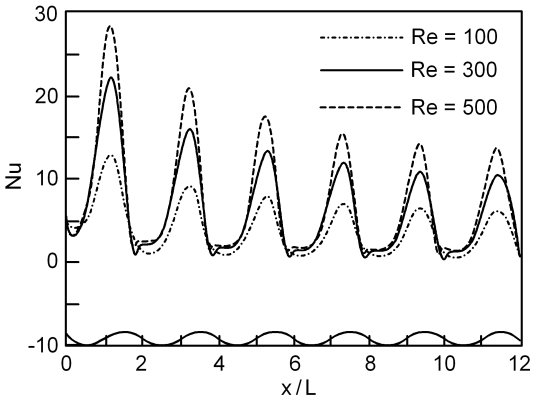

Figure 2.13: Distribution of the local Nusselt number for $a/L = 0.2$ and $Pr = 6.93$, [69].

Detailed direct numerical simulations of laminar, transitional and chaotic flow in converging - diverging wavy channels were performed by Guzmán and Amon [18]. Modern dynamical system techniques such as time-delay reconstructions of pseudophase spaces, autocorrelation functions, fractal dimensions and Eulerian-Lyapunov exponents are used for the dynamical flow characterisation and stability analysis. Their simulations indicate the presence of stable three-dimensional oscillatory flows. The value of the largest Eulerian Lyapunov exponent verifies that the flow changes its behaviour from a quasi-periodic predictable regime to an aperiodic, chaotic, unpredictable regime at Reynolds numbers between 500 and 550. In Figure 2.14 are shown the periodically fully developed streamlines obtained numerically by Guzmán and Amon [18] for different Reynolds numbers. An analysis of linear stability of two-dimensional steady flow in

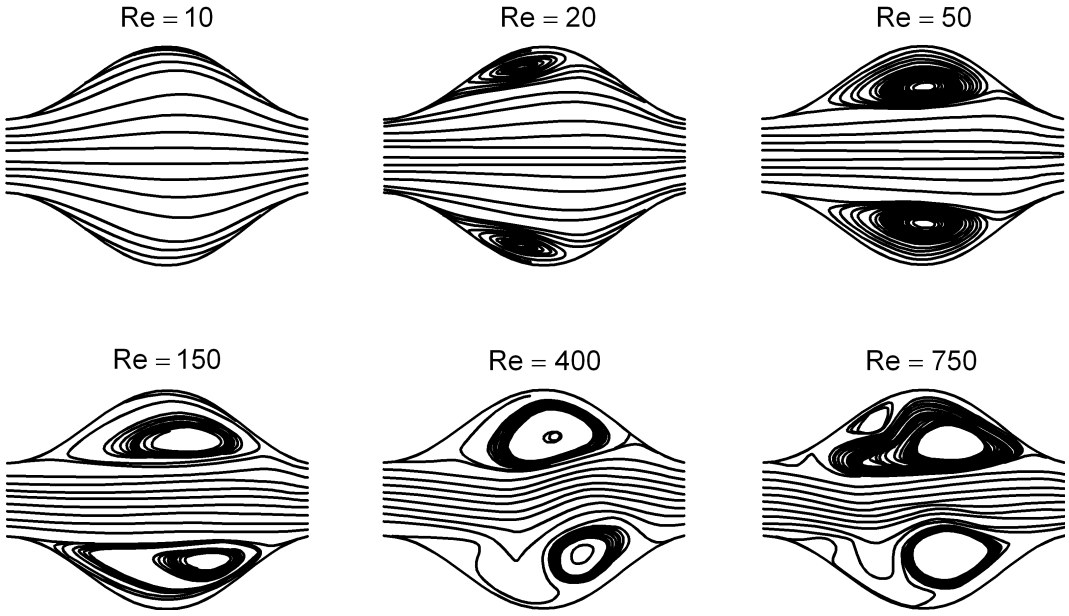

Figure 2.14: Streamlines predicted numerically by Guzmán and Amon [18] for different Reynolds numbers.

wavy channels as in Figure 2.8a and 2.8d with $\varphi = 180°$, was conducted by Cho et. al [9]. Their numerical investigation reveals that the two-dimensional steady flow becomes unstable depending on the waviness hight. Critical Reynolds numbers of the channel as in Figure 2.2d with $\varphi = 180°$ are smaller for three-dimensional disturbances and larger for two-dimensional disturbances in comparison to the symetric channel, Figure 2.2a, and in any case substantially lower than that for plane channel. Another linear stability of the flow in wavy channels analysed was investigated by Blancher et. al [5], who applied a Galerkin approach divergence-free Chebychev basis functions and trigonometric polynomials. They found the instability to set in as a Tollmien-Schlichting wave at $Re \approx 90$. It is also shown that the variations of the local heat transfer coefficient are increased with increasing Prandtl number. Lahbabi and Chang [25] used a global Galerkin method to solve the Navier-Stokes equation in wavy tubes. Their stationary

solution is stable to axisymmetric disturbance at all Reynolds numbers, but destabilises to azimuthal disturbance at a critical Reynolds number. A nonlinear analysis was carried out to characterise the Hopf bifurcation.

An experimental study of flow and heat transfer in sinusoidal wavy passages with different phase shift φ between the sidewalls was conducted by Rush et al. [52], Figure 2.8d. The two walls are in-line with each other at $\varphi = 0°$. At the other extreme, $\varphi = 180°$, converging-diverging wavy channel is established, Figure 2.8a. The experimental results confirm that flow instabilities cause a heat transfer enhancement. The fluid flow is unstable and unsteady even in the laminar flow regime. For a given Reynolds number, the fluid flow in the channels with $\varphi = 0°$ and $\varphi = 90°$ is unsteady farther upstream than in case of $\varphi = 180°$. However, the pressure drop data were not recorded in this study.

As a further means of the heat and mass transfer enhancement, the influence of the oscillatory flow in symmetric wavy walled channels was investigated experimentally by Nishimura et al. [44], Nishimura et al [45] and Nishimura and Matsune [48] and numerically by Nishimura and Matsune [49] and Lee et al. [26]. The influence of the Reynolds number and Strouhal number on the heat and mass transfer has been found to be very important.

Although the works mentioned above are performed with two-dimensional flows on a macroscopic scale, they provide the fundamental background information that is basically also valid for the numerical experiments performed for channels with a pronounced three-dimensional flow that will be presented in this work further below.

2.4 Three-dimensional wavy channel

Channels with three-dimensional wall corrugations are of much greater importance for the practical applications than the two-dimesional wavy cannels, but only few papers are dealing with fluid flow and heat transfer in such channels.

Witry et al. [73, 74] used the CFD code FLUENT and studied numerically the fluid flow, pressure drop and heat transfer of both, inside and outside fluid of a dimple thermoplate, Figure 2.15. Near the inlet and outlet of the thermoplate they analysed, a number of dimples have been removed to allow the interior flow to re-distribute itself without causing high pressure losses. The velocity and pressure distributions of the inside fluid flow are given in Figures 2.16 and 2.17, respectively. Closer inspection of the flow field around the dimples show the three-dimensionality of the problem. It can also be seen, that the high inlet pressure is lost due to the direct hit against the dimple facing the inlet and to the sudden enlargement in cross-sectional area, which indicates the need for more dimples to be removed from the region near the inlet connection tube. A rapid temperature drop, Figure 2.18, takes place in the vicinity of areas where the flow slows down. The high fluid velocities, especially near the inlet, lead to a high heat

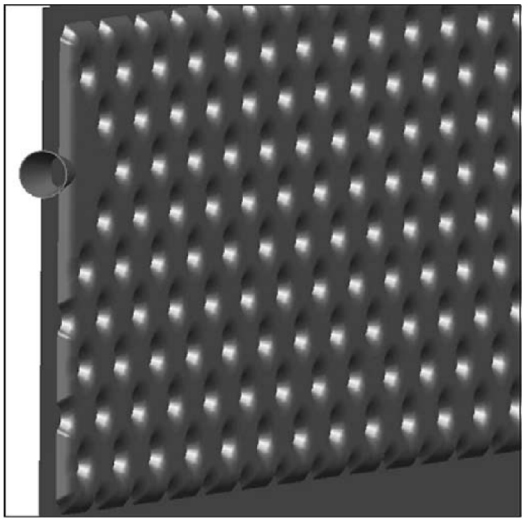

Figure 2.15: Dimple plate geometry numerically analysed by Witry et al. [73].

transfer coefficients. The values of the overall heat transfer coefficient are higher than the expected ones for tubular heat exchangers. However, the authors did not make any numerical experiment to show how the heat transfer depends on the thermoplate geometry.

Sawyers et al. [56] combined analytical and numerical techniques to study the effect of three-dimensional hydrodynamics on the enhancement of steady, laminar heat transfer in corrugated channels with walls having constant, but different temperature. Since the periodic boundary conditions have been adopted, the results refer to the developed flow. The authors took the channel with two-dimensional sinusoidal corrugations, Figure 2.19, as the base. It was found, that the heat transfer in such channels was higher than for the flat plates due to the presence of recirculation zones. In the three-dimensional case, Figure 2.20, the corrugations are sinusoidal in two orthogonal directions. A small mean flow in the transverse direction allows particles to cross between the recirculation zones and the main flow, which leads to an increase in the heat transfer.

From the literature review follows that the fluid flow with heat transfer in channels with three-dimensional wall corrugations has benn studied only by few authors. A dependency of heat transfer and pressure drop on geometrical parameter of such channels was not investigated. A Nusselt number correlation has not been given. For that reason in this thesis the fluid flow and heat transfer in the thermoplates with walls corrugated sinusoidaly in two orthogonal directions that are spot-welded according to an appropriate pattern were studied. The walls were kept at the same, constant temperature. The dependency of the heat transfer and the pressure drop on thermoplate geometry was investigated. The details will be given in Chapters 4 and 5. A part of these investigations were published in papers by Mitrović and Maletić in their papers [34, 35, 36].

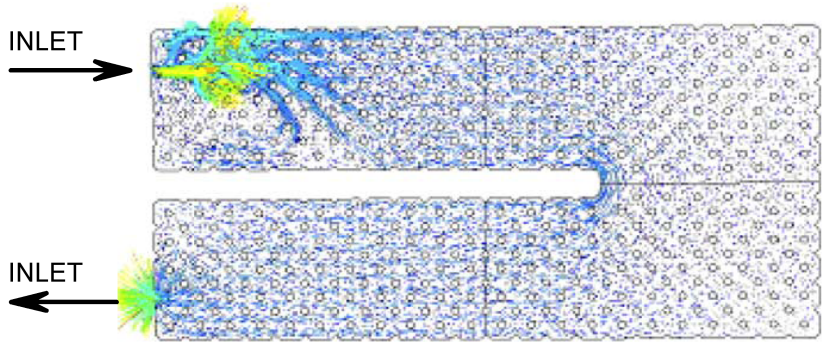

Figure 2.16: Internal flow velocity vectors in the plate radiator calculated by Witry et al. [73].

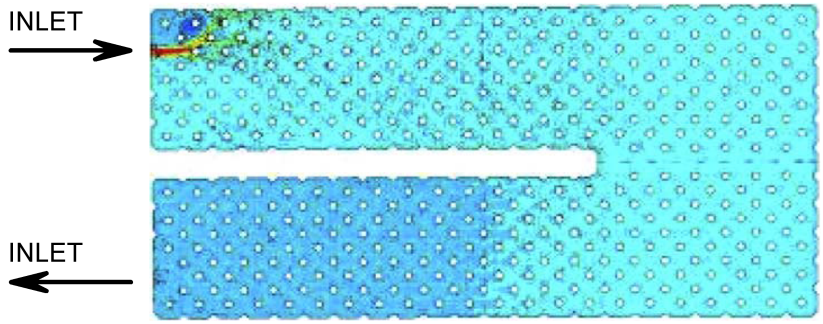

Figure 2.17: Internal flow pressure distribution in the plate radiator calculated by Witry et al. [73].

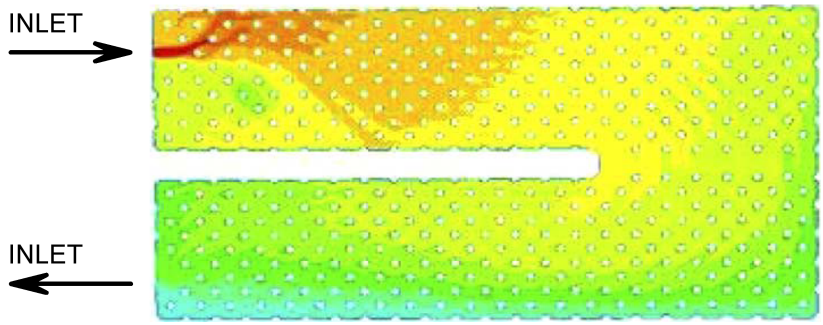

Figure 2.18: Internal flow temperature distribution in the plate radiator calculated by Witry et al. [73].

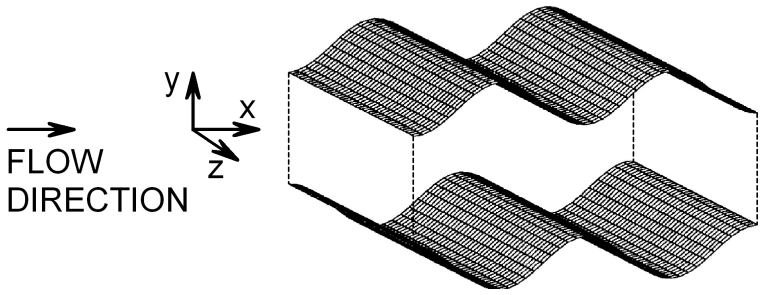

Figure 2.19: Channel with two-dimensional corrugations, Sawyers et al. [56].

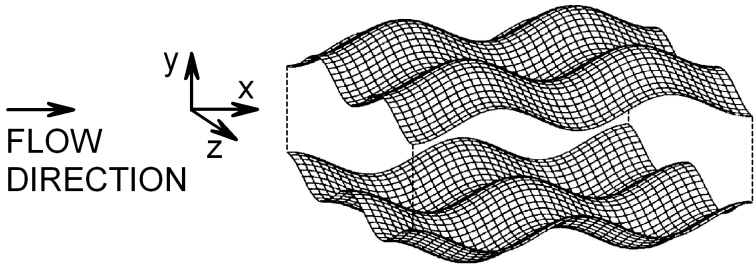

Figure 2.20: Channel with three-dimensional corrugations, Sawyers et al. [56].

3 Heat Transfer in a Parallel Plate Channel

A parallel plate channel is a simple device that basically belongs to the large channel family. It is frequently used for comparison purposes when channels of a complex geometry are to be used for numerical or laboratory experiments. For this reason, the fluid flow and heat transfer in this channel is treated next under steady-state conditions, assuming the plates to be at constant, but different temperatures.

3.1 Physical model and governing equations

The physical model of the so-called asymmetric Graetz problem is shown in Figure 3.1. Two smooth parallel plates that confine the fluid space, a distance $2b$ apart, are kept at constant but different temperatures ϑ_{W1} and ϑ_{W2}. Since the plates are infinite in the y-direction (i.e. $a >> 2b$), this represents a two-dimensional model. The steady state laminar flow is directed along the z-coordinate.

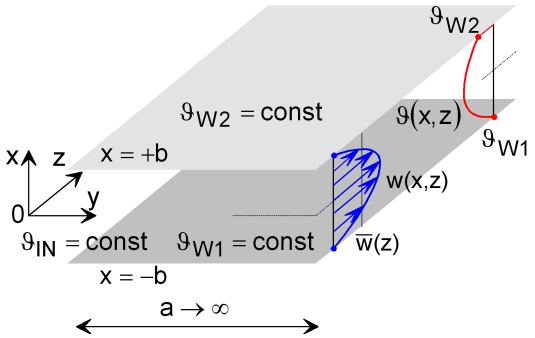

Figure 3.1: Illustration of the physical model.

As given in the monograph of Petukhov [50], the fluid velocity $w(x, z)$ along the z-axis, that takes into account the hydraulically developing region is calculated from an expression deduced by Targ,

$$w(X, Z) = \frac{3}{2}\bar{w}(1 - X^2) - 2\bar{w}\sum_{n=1}^{\infty}\frac{1}{\omega_n^2}\left(1 - \frac{\cos(\omega_n X)}{\cos(\omega_n)}\right)e^{-16\omega_n^2 Z}, \tag{3.1}$$

where the dimensionless parameters are defined in the following manner

$$X = \frac{x}{b}, \qquad Z = \frac{1}{Re}\frac{z}{d_h}, \qquad d_h = 4b, \qquad Re = \frac{\bar{w}d_h}{\nu} = 4\frac{\bar{w}b}{\nu}, \tag{3.2}$$

ω_n being the n^{th} root of the equation $tan(\omega) = \omega$.

In case of hydrodynamically developed flow, Equation (3.1) reduces to the Poiseuille parabolic velocity field

$$w(X) = \frac{3}{2}\bar{w}(1 - X^2). \tag{3.3}$$

For simplicity reasons, in many textbooks a constant velocity is adopted:

$$w(X) = \bar{w}. \tag{3.4}$$

To describe the heat transfer between parallel plates mathematically , the energy equation for stationary single phase forced two-dimensional convection is used

$$u\frac{\partial\vartheta}{\partial x} + w\frac{\partial\vartheta}{\partial z} = \kappa\left(\frac{\partial^2\vartheta}{\partial x^2} + \frac{\partial^2\vartheta}{\partial z^2}\right), \tag{3.5}$$

where κ represents the thermal diffusivity; the viscous dissipation is neglected. Since the distance between the plates is considered to be small in comparison to its length, the convection in the x-direction and the diffusion in the z-direction can be neglected. The energy Equation (3.5) becomes:

$$w\frac{\partial\vartheta}{\partial z} = \kappa\frac{\partial^2\vartheta}{\partial x^2}. \tag{3.6}$$

According to the Figure 3.1, the temperature ϑ must satisfy the following boundary conditions:

$$-b \le x \le +b \quad \text{and} \quad z = 0: \qquad \vartheta(x, 0) = \vartheta_{IN}, \tag{3.7}$$

$$x = -b \quad \text{and} \quad z > 0: \qquad \vartheta(-b, z) = \vartheta_{W1}, \tag{3.8}$$

$$x = +b \quad \text{and} \quad z > 0: \qquad \vartheta(+b, z) = \vartheta_{W2}. \tag{3.9}$$

3.2 Normalised temperature function and analytical solution

Using the expression for the hydrodynamically developed flow (3.3) and introducing the dimensionless quantities

$$\Theta(X, Z_*) = \frac{\vartheta(X, Z_*) - \vartheta_{W1}}{\vartheta_{IN} - \vartheta_{W1}}, \tag{3.10}$$

$$Z_* = \frac{8}{3}\frac{1}{RePr}\frac{z}{b}, \qquad Pr = \frac{\nu}{\kappa}, \tag{3.11}$$

the energy equation (3.6) becomes

$$(1-X^2)\frac{\partial\Theta}{\partial Z_*}=\frac{\partial^2\Theta}{\partial X^2}. \tag{3.12}$$

The boundary conditions (3.7)-(3.9) become correspondingly

$$-1\le X\le+1 \quad \text{and} \quad Z_*=0: \qquad \Theta(X,0)=1, \tag{3.13}$$

$$X=-1 \quad \text{and} \quad Z_*>0: \qquad \Theta(-1,Z_*)=\Theta_{W1}=0, \tag{3.14}$$

$$X=+1 \quad \text{and} \quad Z_*>0: \qquad \Theta(+1,Z_*)=\Theta_{W2}. \tag{3.15}$$

To separate the variables in X and Z_* directions for Equation (3.12) and to satisfy the boundary conditions (3.13)-(3.15) the following ansatz was made

$$\Theta(X,Z_*)=\frac{\Theta_{W2}}{2}(1+X)+\sum_{n=1}^{\infty}A_n\varphi_n(X)e^{-\lambda_n^2 Z_*}, \tag{3.16}$$

where the first term on the right-hand side represents the temperature profile of the thermally developed flow, $\varphi_n(X)$ are the eigenfunctions and λ_n the eigenvalues of the following eigenvalue problem:

$$\varphi_n''(X)+\lambda_n^2(1-X^2)\varphi_n(X)=0, \tag{3.17}$$

$$\varphi_n(-1)=0, \tag{3.18}$$

$$\varphi_n(+1)=0. \tag{3.19}$$

Since all φ_n functions are orthogonal to each other, the scalar product $\int_{-1}^{1}\varphi_n\varphi_m$ disappears, except for $n=m$. Multiplying (3.16) by $\varphi_m(1-X^2)$, integrating from $X=-1$ to $X=+1$ and setting back $m=n$ the expression for the A_n is deduced:

$$A_n=\frac{(\Theta_{W2}-1)\varphi_n'(+1)+\varphi_n'(-1)}{\lambda_n\left(\left(\varphi_n'\frac{\partial\varphi_n}{\partial\lambda_n}\right)_{X=+1}-\left(\varphi_n'\frac{\partial\varphi_n}{\partial\lambda_n}\right)_{X=-1}\right)}. \tag{3.20}$$

A solution of (3.17) can be obtained in form of series. However, the solution can be written in more compact form using the Kummer confluent hypergeometric function ${}_1F_1((1-\lambda_n)/4;1/2;\lambda_nX^2)$ and the Hermite polynomials $H_{(\lambda_n-1)/2}(\lambda_n^{1/2}X)$, that are already implemented in a number of commercial software packages (in this work Mathematica 5 was used) and that can be found, e.g., in books by Slater [60] or Abramowitz and Stegun [1]. The solution of (3.17) has thus the following form

$$\varphi_n(X)=D_ne^{\frac{-\lambda_nX^2}{2}}\left({}_1F_1\left(\frac{1-\lambda_n}{4};\frac{1}{2};\lambda_nX^2\right)+E_nH_{\frac{\lambda_n-1}{2}}\left(\lambda_n^{\frac{1}{2}}X\right)\right), \tag{3.21}$$

where D_n and E_n are arbitrary constants. The constants D_n can be thought to be a part of A_n, thus $D_n = 1$. Applying the boundary conditions (3.18) and (3.19) to the solution (3.21) gives:

$$ {}_1F_1\left(\frac{1-\lambda_n}{4};\frac{1}{2};\lambda_n\right) + E_n H_{\frac{\lambda_n-1}{2}}\left(-\lambda_n^{\frac{1}{2}}\right) = 0, \tag{3.22} $$

$$ {}_1F_1\left(\frac{1-\lambda_n}{4};\frac{1}{2};\lambda_n\right) + E_n H_{\frac{\lambda_n-1}{2}}\left(\lambda_n^{\frac{1}{2}}\right) = 0. \tag{3.23} $$

These expressions suffice to obtain the constants E_n and the eigenvalues λ_n as positive roots of the characteristic equation, which follows from (3.22) and (3.22), and which can be written as

$$ {}_1F_1\left(\frac{1-\lambda_n}{4};\frac{1}{2};\lambda_n\right)\left(H_{\frac{\lambda_n-1}{2}}\left(\lambda_n^{\frac{1}{2}}\right) - H_{\frac{\lambda_n-1}{2}}\left(-\lambda_n^{\frac{1}{2}}\right)\right) = 0. \tag{3.24} $$

It is useful and illustrative to rewrite the characteristic equation (3.24) as follows

$$ {}_1F_1\left(\frac{1-\lambda_n}{4};\frac{1}{2};\lambda_n\right) = 0, \tag{3.25} $$

$$ H_{\frac{\lambda_n-1}{2}}\left(\lambda_n^{\frac{1}{2}}\right) - H_{\frac{\lambda_n-1}{2}}\left(-\lambda_n^{\frac{1}{2}}\right) = 0, \tag{3.26} $$

because it can be recognised that Equation (3.25) corresponds to the classical, symmetrical Graetz problem, whereas Equation (3.26) takes into account the asymmetry of the thermal action on the fluid. The first 30 eigenvalues obtained from (3.25) and (3.26) are listed in the Table 3.1.

Hatton and Turton [19] solved also this problem for eigenvalues, which are in a satisfactory agreement with those from this work, but the solution for the eigenfunctions $\varphi_n(X)$ in their paper was not shown. This extension, Equation (3.21), was done by Mitrović, Maletić and Bačlić [32]. For $n = 3k+1$, $k = 0, 1, 2, ..., \infty$, the eigenfunctions are zero, $\varphi_n(X) = 0$, so that only the roots λ_n for $n = 3k+2$ and $n = 3k+3$, $k = 0, 1, 2, ..., \infty$ have to be considered.

In the general solution (3.21) the eigenfunctions φ_n corresponding to the eigenvalues λ_n where $n = 3k+2$ are called by Hutton and Turton [19] even eigenfunctions and they have the following properties:

$$ \varphi_n(-1) = \varphi_n(1) = 0, \qquad \varphi_n(0) = 1, \qquad \varphi_n'(-1) = -\varphi_n'(1), \qquad \varphi_n'(0) = 0, \tag{3.27} $$

whereas for $n = 3k+3$ the eigenfunctions, called odd eigenfunctions by Hutton and Turton [19], have the properties that are different from those given in Equation (3.27)

$$ \varphi_n(-1) = \varphi_n(1) = \varphi_n(0) = 0, \qquad \varphi_n'(-1) = \varphi_n'(1), \qquad \varphi_n'(0) > 0. \tag{3.28} $$

Table 3.1: Some eigenvalues λ_n of the asymmetrical Graetz problem

n	λ_n	n	λ_n	n	λ_n
1	1.00000	11	13.668	21	27.667
2	1.68169	12	15.667	22	29.000
3	3.67229	13	17.000	23	29.667
4	5.00000	14	17.667	24	31.667
5	5.66996	15	19.667	25	33.000
6	7.66881	16	21.000	26	33.667
7	9.00000	17	21.667	27	35.667
8	9.66824	18	23.667	28	37.000
9	11.6679	19	25.000	29	37.667
10	13.0000	20	25.667	30	39.667

3.2.1 Characteristic temperature distributions

Before discussing the thermal asymmetry effect on the Nusselt number, i.e. heat transfer, some typical temperature distributions are presented. Figure 3.2 shows, as an example, the development of the temperature field when the fluid enters the channel at a temperature below those of the plates, $\vartheta_{IN} < \vartheta_{W2} < \vartheta_{W1}$. The surface $\Theta = \Theta(X, Z_*)$, Equation (3.16), bordering the thermally affected fluid region is attached to the plates having the temperatures $\Theta_{W1} = 0$ and $\Theta_{W2} = 0.4$. As may be taken from the Figure, the fluid temperature decreases along the coordinate Z_*, except for the immediate start of the thermal action on the fluid near $X = 0$.

At fixed Z_*, the temperature profile shows a maximum, which moves toward the upper plate ($X = +1$, $\Theta_{W2} = 0.4$), as Z_* increases, Figure 3.3. When the temperature maximum reaches this plate, the plate becomes adiabatic with a zero heat flux at that position. For the chosen temperature Θ_{W2}, this occurs at $Z_* = 0.6816$, Figures 3.2 and 3.3.

The axial position Z_* with the zero heat flux is an important marker of the physical model. Regarding the heat transfer, the corresponding cross-section separates the channel in two regions. In the upstream region, the fluid is heated by both plates, but downstream, it is heated by the lower ($X = -1$, $\Theta_{W1} = 0$), and cooled by the upper plate ($X = +1$, $\Theta_{W1} = 1$). This interplay is illustrated in Figure 3.4, where the slopes of the dimensionless temperature at the plates are plotted along the coordinate Z_* according to Equation (3.39). The curves correspond to the wall heat flux $\dot{q}_W$ given in equations (3.30) and (3.31). For equal temperature slopes, $(\partial\Theta/\partial X)_{W1} = (\partial\Theta/\partial X)_{W2} = 0.2$, the heat is transferred at the same rate from the lower plate to the upper one through the fluid like through a solid wall, which corresponds to the thermally developed flow, see the temperature profile at $Z_* = 2$ in Figure 3.3.

As a further example, Figure 3.5 gives the temperature development for $\Theta_{W2} = 1$,

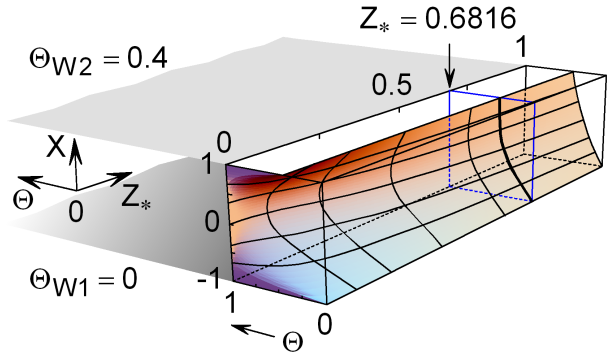

Figure 3.2: Temperature field at specified boundary conditions, $\Theta_{W1} = 0$ and $\Theta_{W2} = 0.4$, with hydrodynamically developed flow, Equation (3.3).

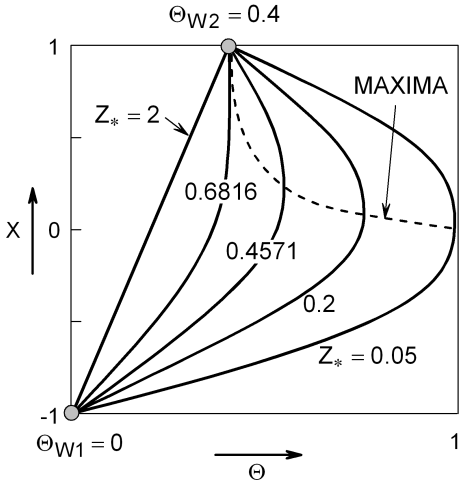

Figure 3.3: Temperature profiles for some fixed values of Z_*. At $Z_* = 0.6816$ the upper plate is adiabatic.

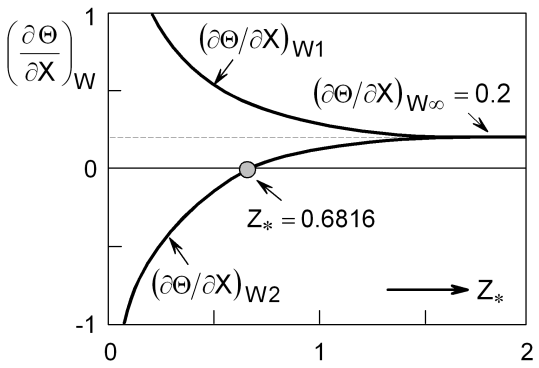

Figure 3.4: The temperature slope at the plates for $\Theta_{W1} = 0$ and $\Theta_{W2} = 0.4$.

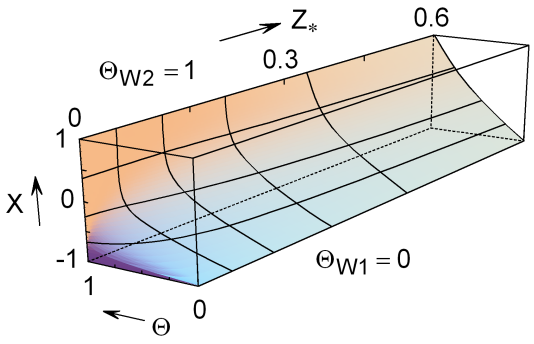

Figure 3.5: Temperature field at specified boundary conditions, $\Theta_{W1} = 0$ and $\Theta_{W2} = 1$, with hydrodynamically developed flow, Equation (3.3).

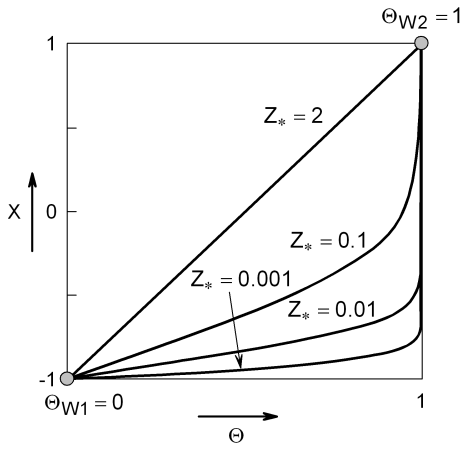

Figure 3.6: Temperature profiles for some fixed values of Z_* for $\Theta_{W1} = 0$ and $\Theta_{W2} = 1$.

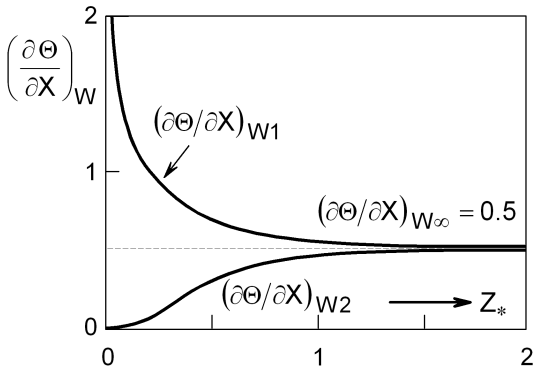

Figure 3.7: The temperature slope at the plates for $\Theta_{W1} = 0$ and $\Theta_{W2} = 1$.

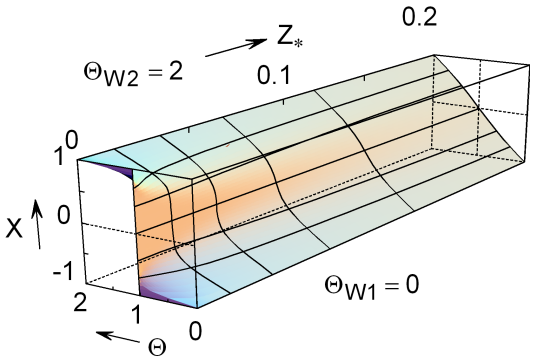

Figure 3.8: Temperature field at specified boundary conditions, $\Theta_{W1} = 0$ and $\Theta_{W2} = 2$, with hydrodynamically developed flow, Equation (3.3).

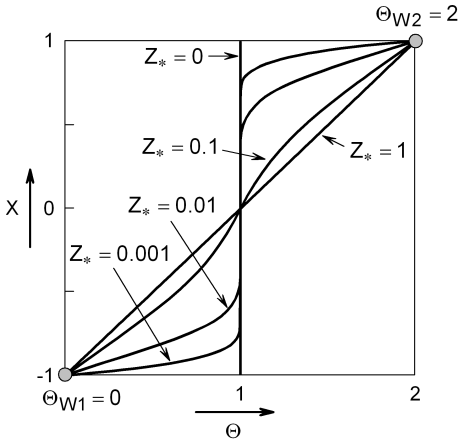

Figure 3.9: Temperature profiles for some fixed values of Z_* for $\Theta_{W1} = 0$ and $\Theta_{W2} = 2$.

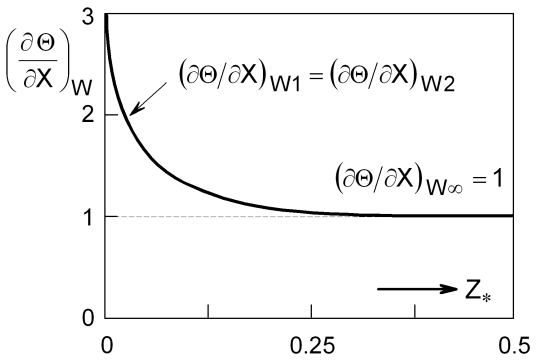

Figure 3.10: The temperature slope at the plates for $\Theta_{W1} = 0$ and $\Theta_{W2} = 1$.

that is, for the temperature of one plate equal to the fluid inlet temperature. The corresponding temperature profiles and the temperature slopes are plotted in Figures 3.6 and 3.7.

Finally, Figure 3.8 shows the development of the temperature field for $\Theta_{W2} = 2$. In this case, the fluid is heated by one and cooled by the other plate at the same rate so that the mean fluid temperature remains unchanged along the flow direction, $\bar{\Theta}(Z_*) = 1$. Some temperature profiles and the temperature slopes at the plates are displayed in Figures 3.9 and 3.10. Because of the total thermal asymmetry imposed, the temperature slopes coincide for this case.

3.3 The Nusselt Number

The local Nusselt number $Nu(z)$ is usually defined by using the local heat transfer coefficient, $h(z)$, the hydraulic diameter of the flow cross section, d_h, and the thermal conductivity of the fluid, k, as follows:

$$Nu(z) = \frac{h(z) d_h}{k}. \tag{3.29}$$

Since the plates are kept at different temperatures, the heat flux, the heat transfer coefficients and the Nusselt numbers at the upper and at the lower plate are consequently different.

At this place, it is to be noted, that some authors define an average Nusselt number of the channel, that takes into account the heat transfer at both plates, see e.g. Nield [41]. However, such average Nusselt number has in case of thermal asymmetry no practical relevance. For this reason, it is clearly distinguished between heat transfer characteristics at the upper and at the lower plate in this work.

Having in mind the boundary conditions (3.8) and (3.9), i.e. the physical model in Figure 3.1 and adopting the sign convention to give the heat flux direction according to the temperature gradient (direction of decreasing temperature), the heat flux from the lower and the upper plate, respectively, to the fluid is given by

$$\dot{q}_{W1}(z) = -k \left(\frac{\partial \vartheta}{\partial x} \right)_{x=-b} = h_{W1}(z) \left(\vartheta_{W1} - \bar{\vartheta}(z) \right), \tag{3.30}$$

$$\dot{q}_{W2}(z) = -k \left(\frac{\partial \vartheta}{\partial x} \right)_{x=+b} = h_{W2}(z) \left(\bar{\vartheta}(z) - \vartheta_{W2} \right). \tag{3.31}$$

From these equations the heat transfer coefficients at the plates are immediately

calculated by

$$h_{W1}(z) = -\frac{k}{\left(\vartheta_{W1} - \bar{\vartheta}(z)\right)} \left(\frac{\partial \vartheta(x,z)}{\partial x}\right)_{x=-b}, \tag{3.32}$$

$$h_{W2}(z) = \frac{k}{\left(\vartheta_{W2} - \bar{\vartheta}(z)\right)} \left(\frac{\partial \vartheta(x,z)}{\partial x}\right)_{x=+b}. \tag{3.33}$$

The average (mixing-cup) fluid temperature is calculated from

$$\bar{\vartheta}(z) = \frac{1}{2b\bar{w}} \int_{-b}^{+b} w(x,z)\vartheta(x,z)dx. \tag{3.34}$$

where the Poiseuille parabolic velocity profile given in Equation (3.3) was used.

With the dimensionless temperature defined in Equation (3.10), the heat transfer coefficients (3.32) and (3.33) become

$$h_{W1}(Z_*) = \frac{1}{\bar{\Theta}(Z_*)} \frac{k}{b} \left(\frac{\partial \Theta(X,Z_*)}{\partial X}\right)_{X=-1}, \tag{3.35}$$

$$h_{W2}(Z_*) = \frac{1}{\Theta_{W2} - \bar{\Theta}(Z_*)} \frac{k}{b} \left(\frac{\partial \Theta(X,Z_*)}{\partial X}\right)_{X=+1}, \tag{3.36}$$

where the average dimensionless temperature and temperature slope are

$$\bar{\Theta}(Z_*) = \frac{\bar{\vartheta}(Z_*) - \vartheta_{W1}}{\vartheta_{IN} - \vartheta_{W1}} = \frac{3}{4} \int_{-1}^{+1} (1 - X^2)\Theta(X,Z_*)dX, \tag{3.37}$$

$$\bar{\Theta}(Z_*) = \frac{\Theta_{W2}}{2} - \frac{3}{4} \sum_{n=1}^{\infty} \frac{A_n}{\lambda_n^2} \left(\varphi_n'(+1) - \varphi_n'(-1)\right) e^{-\lambda_n^2 Z_*}, \tag{3.38}$$

$$\frac{\partial \Theta(X,Z_*)}{\partial X} = \frac{\Theta_{W2}}{2} + \sum_{n=1}^{\infty} A_n \varphi_n'(X) e^{-\lambda_n^2 Z_*}. \tag{3.39}$$

The corresponding Nusselt numbers are then

$$Nu_{W1}(Z_*) = \frac{4}{\bar{\Theta}(Z_*)} \left(\frac{\partial \Theta(X,Z_*)}{\partial X}\right)_{X=-1}, \tag{3.40}$$

$$Nu_{W2}(Z_*) = \frac{4}{\Theta_{W2} - \bar{\Theta}(Z_*)} \left(\frac{\partial \Theta(X,Z_*)}{\partial X}\right)_{X=+1}. \tag{3.41}$$

In the fully developed region ($Z_* \to \infty$) the summations in equations (3.38) and (3.39) disappear and equations (3.40) and (3.41) immediately give

$$Nu_{W1} = Nu_{W1} = Nu_{\infty} = 4. \tag{3.42}$$

In comparison with the thermally developed flow, the local Nusselt numbers $Nu_{W1}(Z_*)$ and $Nu_{W2}(Z_*)$, calculated from equations (3.40) and (3.41), can dramatically change in the thermally developing region. Depending on the boundary conditions (3.13) to (3.15) the average fluid temperature $\bar{\Theta}(Z_*)$ can become equal to the wall temperature $\Theta_{W1} = 0$ or Θ_{W2} at certain position Z_*. Due to this fact and the definition of the heat transfer coefficient, the Nusselt Number Nu_{W1} or Nu_{W2} can become infinite, positive or negative, or, in other words, the Nusselt numbers can have a vertical asymptote, although the temperature slope (3.39) changes always continuously.

Furthermore, the temperature slope defined in Equation (3.39) can become equal to zero at some position Z_*, which characterises the adiabatic cross section at the upper or at the lower plate.

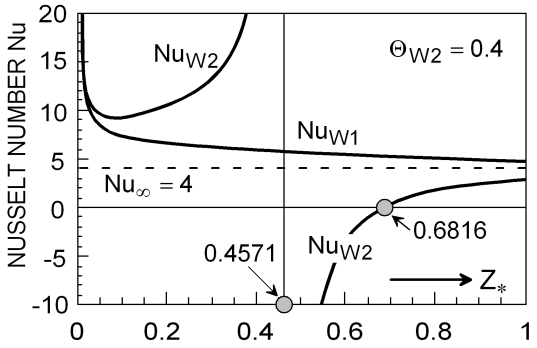

Figure 3.11: Distribution of the local Nusselt numbers $Nu(Z_*)$ along the flow direction for $\Theta_{W1} = 0$ and $\Theta_{W2} = 0.4$.

Such an example is illustrated in Figure 3.11 for $\Theta_{W2} = 0.4$, which corresponds to the temperature field and the temperature profiles shown in Figures 3.2 and 3.3. While the Nusselt number $Nu_{W1}(Z_*)$ of the lower plate ($X = -1$) is always positive and continually decreasing along the flow direction, the situation is essentially different with the Nusselt number $Nu_{W2}(Z_*)$ of the upper plate ($X = +1$). The curve representing $Nu_{W2}(Z_*)$ shows a discontinuity with a vertical asymptote. Left to the asymptote, $Nu_{W2}(Z_*) > 0$, whereas on the right, $Nu_{W2}(Z_*)$ is first negative, becoming zero and then positive. With increasing Z_*, the Nusselt numbers take asymptotically the value in the thermally developed flow, $Nu_\infty = 4$. Similar behaviour has already been reported by Hatton and Turton [19].

Figure 3.12 gives a general idea of what happens when the dimensionless temperature of the upper plate Θ_{W2} increases from a negative value up to $\Theta_{W2} = 0$ first, and than further up to $\Theta_{W2} = 1$. The situation where the fluid inlet temperature ϑ_{IN} is greater than both wall temperatures, ϑ_{W1} and ϑ_{W2}, which corresponds to $\Theta_{W2} < 0$, is displayed on the left side of the Figure 3.12. The Nusselt number Nu_{W2} of the upper plate is always positive and changes continuously, whereas the Nusselt number Nu_{W1} of the lower plate experiences a discontinuity while passing the vertical asymptote. The

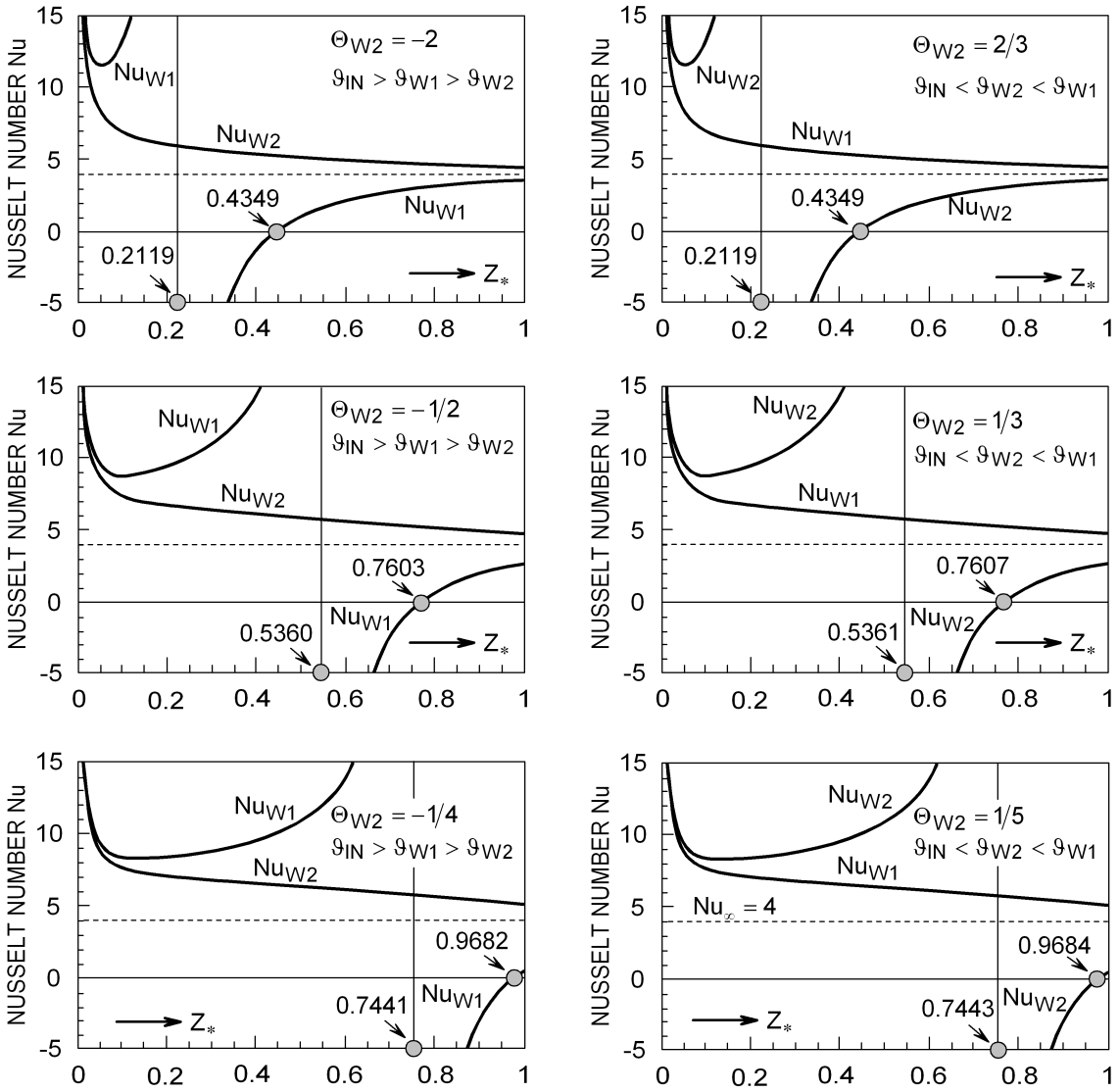

Figure 3.12: Effect of boundary conditions on Nusselt number for hydrodynamically developed flow for $\Theta_{W1} = 0$ at different Θ_{W2}.

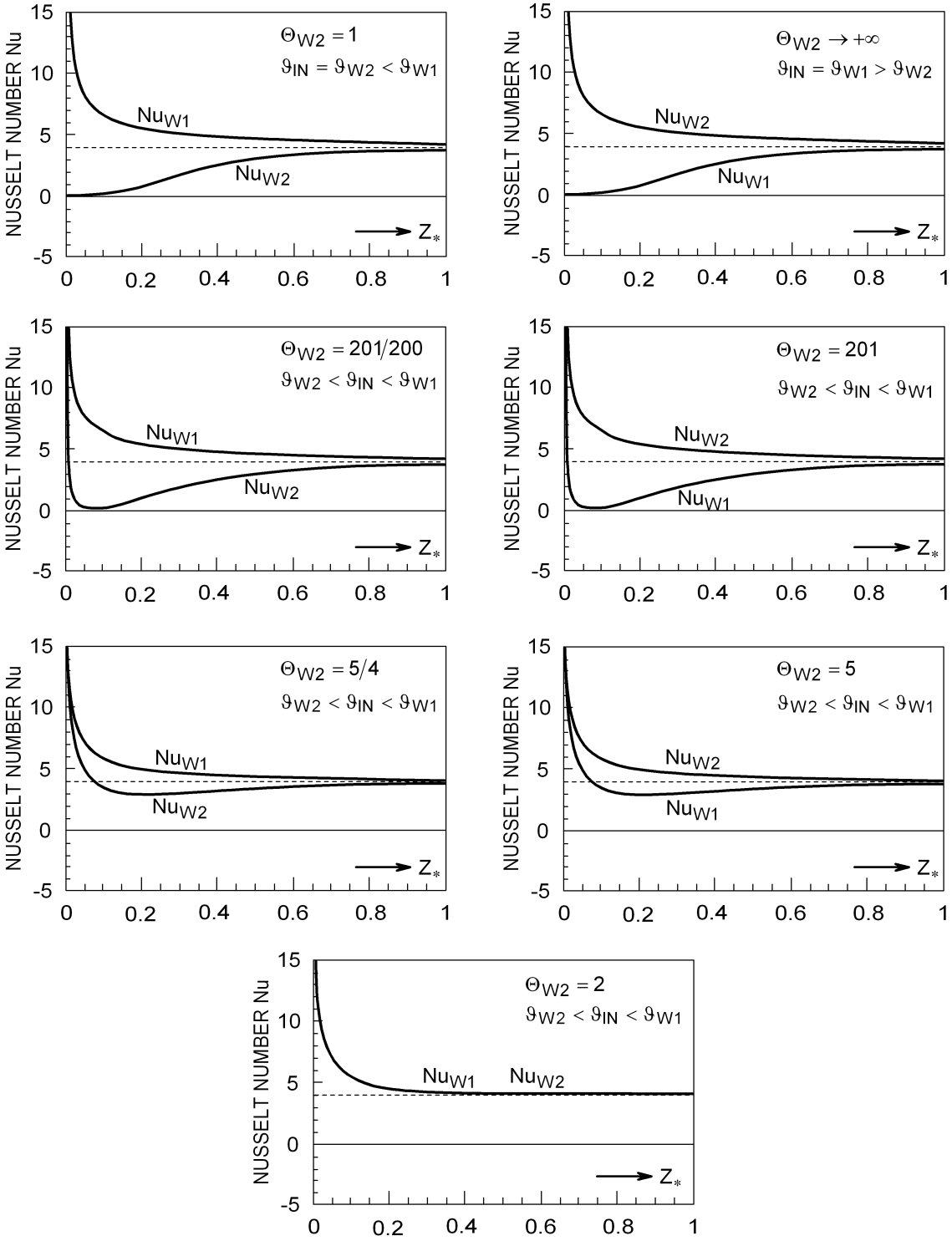

Figure 3.13: Effect of boundary conditions on Nusselt number for hydrodynamically developed flow for $\Theta_{W1} = 0$ at different Θ_{W2}.

position of this asymptote moves downstream as the dimensionless temperature of the upper plate Θ_{W2} rises in the interval $-\infty < \Theta_{W2} < 0$. The situation is very similar if Θ_{W2} rises further in the interval $0 < \Theta_{W2} < 1$, right side of the Figure 3.12. This is the case when the fluid inlet temperature ϑ_{IN} is less than both wall temperatures, ϑ_{W1} and ϑ_{W2}. The upper and the lower plate change the roles from a heat transfer point of view and now the Nusselt number of the lower plate Nu_{W1} is positive and changes continuously, whereas Nu_{W2} shows the discontinuity.

Finally, in the region $\Theta_{W2} \geq 1$, which is the case if the fluid inlet temperature ϑ_{IN} is between the plate temperatures, $\vartheta_{W1} > \vartheta_{IN} > \vartheta_{W2}$ or $\vartheta_{W1} < \vartheta_{IN} < \vartheta_{W2}$, both Nusselt numbers Nu_{W1} and Nu_{W2} are positive without discontinuities, Figure 3.13. At $\Theta_{W2} = 1$, the Nu_{W2} curve is sandwiched between two horizontal asymptotes, $Nu = 0$ and $Nu = 4$, thereby showing an inflection point. For $\Theta_{W2} \to +\infty$, the behaviour is the same as for $\Theta_{W2} = 1$, but this time, the Nusselt number Nu_{W1} is sandwiched between the horizontal asymptotes.

For $\Theta_{W2} = 0$ both plates are kept at the same temperature, which corresponds to the classical symmetric Graetz problem. In this case Nu_{W1} and Nu_{W2} are identical, positive, change continuously, becoming $Nu_\infty = 7.545$ at $Z_* \to \infty$. If there are some heat source terms in the energy equation, the average fluid temperature can exceed the wall temperature, even if the heating is symmetric. Such an example in case of porous channel is analysed as special case in the paper by Mitrović and Maletić [37].

The asymmetric Graetz problem considered in this work is discontinuous in two respects. One kind of the discontinuity represents the above discussed jump of the Nusselt number from positive to negative values. The other kind of discontinuity is the switch from one developed state to the other one, which means from the symmetric to the asymmetric thermal conditions. In context with the latter discontinuity, the question arises: How does the fluid decide at a small thermal asymmetry, $\Theta_{W2} \to 0$ or $\vartheta_{W1} \approx \vartheta_{W2}$, which one of the limiting values of the Nusselt numbers, $Nu_\infty = 4.0$ (asymmetric case) or $Nu_\infty = 7.545$ (symmetric case), is to be followed? An answer to this question is not easy to formulate, but Figure 3.14 provides a general idea of what happens when the thermal asymmetry measured in terms of Θ_{W2} is gradually decreased. The curves represent the Nusselt numbers for different thermal asymmetries, whereas the two horizontal lines give the limits of the Nusselt numbers in the fully developed heat transfer region for thermal asymmetry (lower line) and for the thermal symmetry (upper line). At a sufficiently large asymmetry (greater Θ_{W2}, $\Theta_{W2} > 0$) the fluid takes resolutely the "right" way, Figure 3.14, left side. On the contrary, at a very small asymmetry ($\Theta_{W2} \to 0$), one gets the impression as if the fluid knew very little about its fate downstream the flow. The Nusselt number Nu_{W1} first follows the thermal symmetry with $Nu_\infty = 7.545$ from below, but it apparently remembers, further downstream, the actual boundary conditions and switches down to the limit $Nu_\infty = 4.0$ at the thermal asymmetry. At the same time, the Nusselt number Nu_{W2} is either smaller than 4.0 or larger than 7.545. The values between these limits are inaccessible to Nu_{W2}. If $\Theta_{W2} \to 0$, but $\Theta_{W2} < 0$, Figure 3.14, right side, the Nusselt numbers behave in the same way, only with changed roles in

comparison to the discussed situation, where $\Theta_{W2} > 0$.

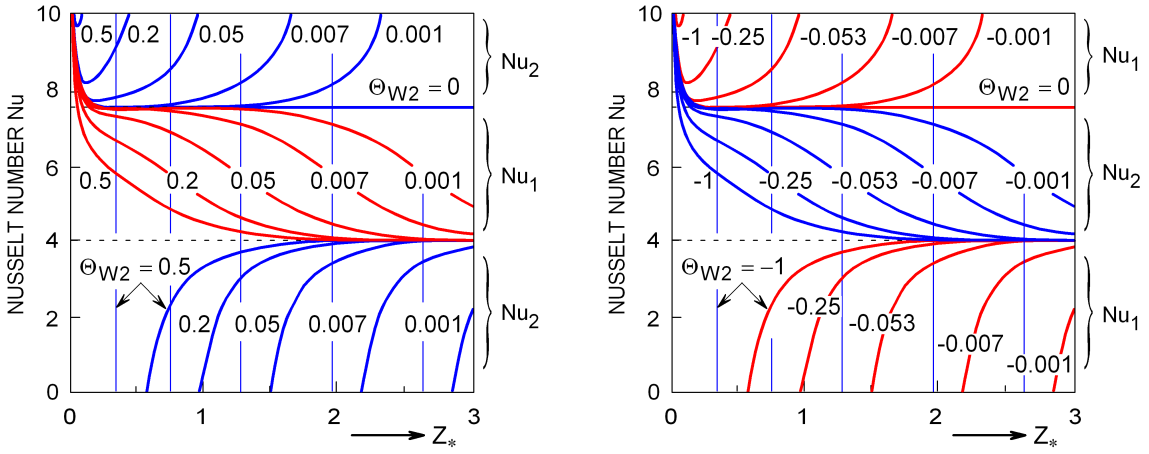

Figure 3.14: Transitions and asymptotical behaviour of the Nusselt numbers for chosen Θ_{W2}.

The thermal behaviour illustrated in Figures 3.11-3.14 has a strong impact on the calculation of the heat transfer. The assumption of a thermally fully developed flow, frequently adopted in practice, is unallowable in an asymmetric case. This is convincingly demonstrated in Figure 3.14, illustrating at the same time the complexity expected when trying to correlate the Nusselt numbers in terms of common quantities. The question as how to calculate the heat transfer coefficient in such a case becomes important, and it is by no means as trivial as it might appear. It is also obvious from Figure 3.14 that the asymmetric Graet problem represents a typical example of physical models where relatively small causes result in strong effects.

In the analysis presented so far, the hydrodynamically developed flow was adopted, i.e. the Poiseuille parabolic velocity profile, expression (3.3), was used to find an analytical solution to the energy equation (3.6). Adopting the plug flow (3.4) or the hydrodynamically developing flow given in Equation (3.1), where the solution to the energy equation (3.6) can be found only numerically, results in the same qualitative distributions of the Nusselt numbers as in Figures 3.12 and 3.13 for the hydrodynamically developed flow. Figure 3.15 displays, as an example, the velocity effect on the Nusselt number, where, for comparison reasons, all tree mentioned velocity distributions were considered. In the case of a constant velocity (plug flow, Figure 3.15a), the position of the vertical asymptote is shifted upstream in comparison to the hydrodynamically developed flow (Figure 3.15b). The almost perfect agreement of the developing (Figure 3.15c) and developed flows is rooted in the relatively large Prandtl number Pr, which affects the contribution of the sum in Equation (3.1) to the parabolic term essentially. This becomes obvious if the coordinate Z_* is introduced in this equation by replacing Z by $(3/32)PrZ_*$, as required by Equations (3.2) and (3.11). Even at a much smaller

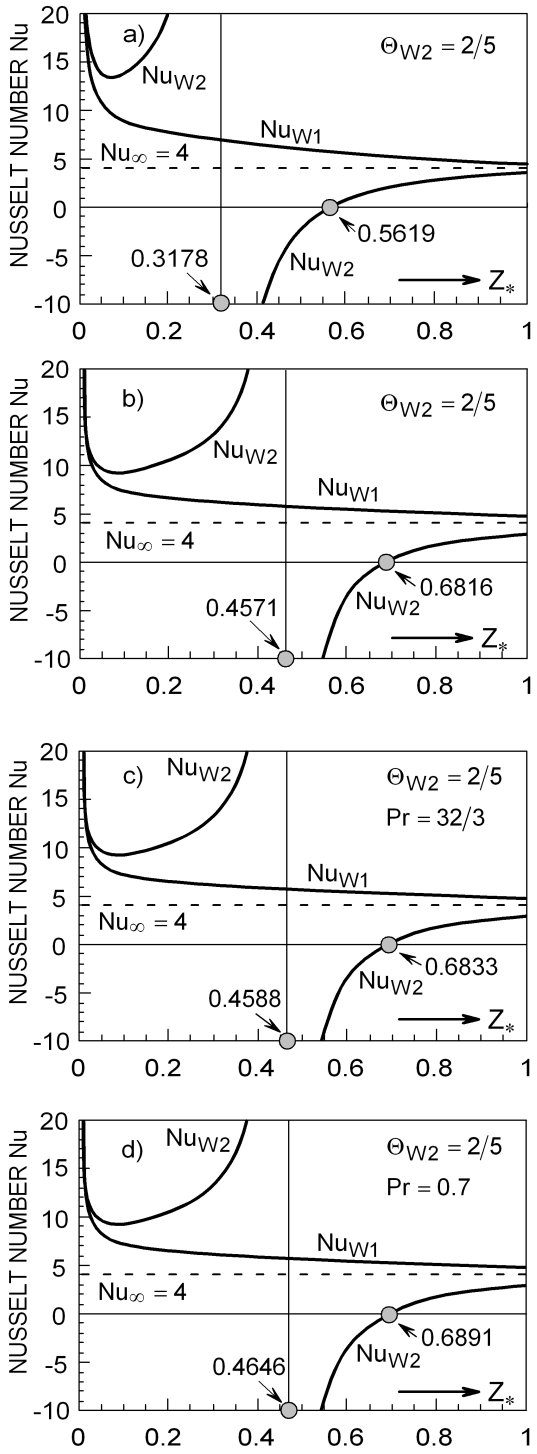

Figure 3.15: Effect of velocity distribution on the position of the vertical asymptote for $\Theta_{W2} = 2/5$. (a) $w = \bar{w} = const$, (b)$w = \frac{3}{2}\bar{w}(1 - X^2)$, (c) $Pr = 32/3$, $w = \bar{w}f(X, Z)$, Equation (3.1), (d) $Pr = 0.7$, $w = \bar{w}f(X, Z)$, Equation (3.1).

Prandtl number, the sum in Equation (3.1) is almost negligible for the conditions specified in Figure 3.15d. The results illustrated in Figure 3.15 do not qualitatively change at other parameter combinations.

The two positions where the Nusselt number becomes infinite and zero and the conditions for these phenomena to occur are of big importance, both from the practical and from the academical point of view and how they depend on the boundary conditions will by analysed in the next section.

3.3.1 Positions of the vertical asymptote and the adiabatic point

The local Nusselt number Nu_{W1} or Nu_{W2} can become infinite positive or negative, i.e. a vertical asymptote can occur at some axial position where the mean fluid temperature in the channel cross-section, Equation (3.38), becomes equal to the temperature of the lower plate, $\Theta_{W1} = 0$, or of the upper plate, Θ_{W2}. Independently of this, the temperature slope, Equation (3.39), can become zero at one of the plates, at another axial position. Consequently, the heat transfer coefficient $\alpha_{W1}(Z_*)$ or $\alpha_{W2}(Z_*)$ and the Nusselt number Nu_{W1} or Nu_{W2} can become zero, which characterises the adiabatic point.

The positions that determine the distances between the channel inlet and the cross-sections where the vertical asymptote of the Nusselt number and the adiabatic point occur are denoted by Z_{A*} and Z_{0*}, respectively. The boundary conditions (3.7) to (3.9) determine if these appearances are possible at all and where, at the lower plate or at the upper plate, and at which distance from the channel inlet. In the dimensionless form this situation is affected only by the dimensionless temperature of the upper plate, Θ_{W2}, since the dimensionless temperatures of the lower plate $\Theta_{W1} = 0$ and of the fluid at the inlet $\Theta_{IN} = 1$ are permanently constant.

The vertical asymptote of the Nusselt number and the adiabatic point establish only at the plate, the temperature of which is closer to the fluid inlet temperature ϑ_{IN} and only if the fluid inlet temperature ϑ_{IN} is smaller or greater than the plate temperatures, ϑ_{W1} and ϑ_{W2}. If $\vartheta_{W1} < \vartheta_{IN} < \vartheta_{W2}$ or $\vartheta_{W1} > \vartheta_{IN} > \vartheta_{W2}$ the vertical asymptote of the Nusselt number and the adiabatic point do not occur at any plate. In terms of the dimensionless temperature this means that there are three characteristical intervals of Θ_{W2}, namely:

- $\Theta_{W2} < 0$; in this case the vertical asymptote and the adiabatic point establish at the lower plate, $X = -1$, and for this reason the notation $\Theta_{W2(X=-1)}$ is used in this analysis,
- $\Theta_{W2} = 0$; this corresponds to the classical symmetrical Graetz problem, where the Nusselt number curves change continuously and neither the vertical asymptote nor the adiabatic point occur,
- $0 < \Theta_{W2} < 1$; the vertical asymptote and the adiabatic point establish at the upper plate, $X = +1$, and this dimensionless temperature is noted here by $\Theta_{W2(X=+1)}$,

- $\Theta_{W2} > 1$; in this interval neither the vertical asymptote nor the adiabatic point are possible at any plate.

As stated above, the vertical asymptote of the Nusselt number establishes at the lower plate, $X = -1$, if

$$\bar{\Theta}(Z_{A*}) = \Theta_{W1} = 0, \tag{3.43}$$

or with (3.38)

$$\Theta_{W2(X=-1)} = \frac{3}{2} \sum_{n=1}^{\infty} \frac{A_n}{\lambda_n^2} \left(\varphi_n'(+1) - \varphi_n'(-1)\right) e^{-\lambda_n^2 Z_{A*}}, \tag{3.44}$$

which can be solved for a real Z_{A*} only if $\Theta_{W2} < 0$.

For the upper plate, $X = +1$, similar condition is valid

$$\bar{\Theta}(Z_{A*}) = \Theta_{W2}, \tag{3.45}$$

or with (3.38)

$$\Theta_{W2(X=+1)} = -\frac{3}{2} \sum_{n=1}^{\infty} \frac{A_n}{\lambda_n^2} \left(\varphi_n'(+1) - \varphi_n'(-1)\right) e^{-\lambda_n^2 Z_{A*}}. \tag{3.46}$$

The Equation (3.46) can be solved for a real Z_{A*} if $0 < \Theta_{W2} < 1$, as stated above.

The conditions for the adiabatic point to occur are

$$\left(\frac{\partial \Theta(X, Z_*)}{\partial X}\right)_{X=-1}, \qquad \left(\frac{\partial \Theta(X, Z_*)}{\partial X}\right)_{X=+1}, \tag{3.47}$$

or using Equation (3.39)

$$\Theta_{W2} + 2 \sum_{n=1}^{\infty} A_n \varphi_n'(X) e^{-\lambda_n^2 Z_{0*}} = 0, \tag{3.48}$$

which can be solved for a real Z_{0*} if $\Theta_{W2} < 0$, which corresponds to the lower plate, $X = -1$, or if $0 < \Theta_{W2} < 1$, which corresponds to the upper plate, $X = +1$.

For $\Theta_{W2} > 1$ there are no real solutions, neither for Z_{A*} nor for Z_{0*}.

Figure 3.16 shows the positions of the vertical Nusselt number asymptote and of the adiabatic point (the reversal of the heat flux) at both plates. Plotted is the dimensionless temperature Θ_{W2} at zero heat transfer potential, $\bar{\Theta}(Z_*) = \Theta_{W1}$ and $\bar{\Theta}(Z_*) = \Theta_{W2}$, and at the zero temperature slope, $(\partial\Theta/\partial X)_{W1} = 0$ and $(\partial\Theta/\partial X)_{W2} = 0$, in dependence of the coordinate Z_*. Since $\Theta_{W1} = 0$, the thermal symmetry is reached at $\Theta_{W2} \to 0$. This means that the two positions, Z_{A*} and Z_{0*}, move downstream as Θ_{W2} tends to

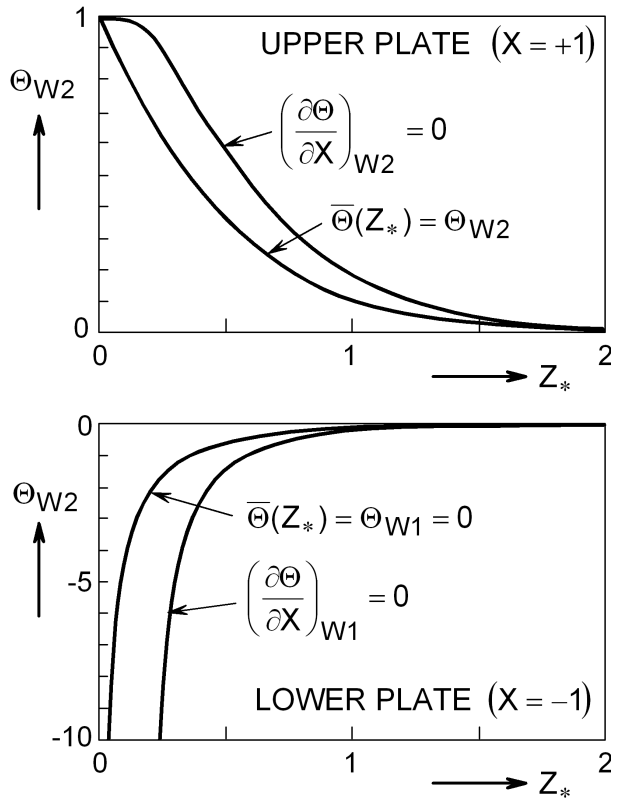

Figure 3.16: Transitions and asymptotical behaviour of the Nusselt numbers for the region $\Theta_{W2} < 1$.

zero and the thermal asymmetry diminishes. Disregarding the limiting cases $Z_* \to 0$ and $Z_* \to \infty$, the inequality $Z_{A*} < Z_{0*}$ is satisfied always.

From the physical reasoning it is irrelevant for the phenomena to occur, which of the plates has a temperature closer to the fluid inlet temperature. Consequently, the curves in Figure 3.16 are expected to be transferable into each other, and indeed, they are reciprocal. Using the properties of the eigenfunctions, equations (3.27) and (3.28), the following important relationship can be deduced

$$(1 - \Theta_{W2(X=-1)})(1 - \Theta_{W2(X=+1)}) = 1. \tag{3.49}$$

This expression describes the dependency of the dimensionless temperatures of the upper plate, $\Theta_{W2(X=-1)}$ and $\Theta_{W2(X=+1)}$, for the vertical Nusselt number asymptotes to occur at the same axial position Z_{A*}, at the lower and at the upper plate, respectively. The dependency (3.49) was first derived by Mitrović, Maletić and Bačlić [32].

4 Fluid Flow and Heat Transfer in Thermoplates

4.1 Problem formulation

The objective of this numerical study is to obtain sets of the geometrical parameters that, in interaction with process parameters, should pave the way for optimal heat transfer of the inside fluid, which is assumed to pass the thermoplate as a single phase (coolant in Figure 2.1).

The overall size of the thermoplate can vary in wide ranges and the connecting tubes can be placed and shaped in a different way. The welding spots can be arranged in a staggered or in a parallel manner and their shape and size can also vary. To investigate the influence of all these parameters on the hydrodynamics and on the heat transfer, a huge number of numerical experiments would be necessary. For each of these experiments, a huge number of the numerical cells would be needed to simulate the fluid flow and heat transfer in whole thermoplate. All this requires again a large computer capacity, a very long computational time, especially in case of transient calculations, and increases total costs of the numerical experiments.

Neglecting the influence of the connecting tubes and of the seam-welded thermoplate edges, a few symmetry planes can be introduced, which reduces the size of the numerical domain, i.e. the number of the numerical cells and the number of the geometrical parameters that are to be varied.

The geometry and dimensions of all simulated three-dimensional models are shown in Figure 4.1. The calculation domain is a strip of a thermoplate channel. The semi-circles represent the welding spots. The strip is confined in spanwise direction by the planes $z = 0$ and $z = s_T$ and in streamwise (x) direction by $x = 0$ and $x = L$.

Depending on the thermoplate type, Figure 2.2, and on the welding spot pattern (staggered or parallel), the heat transfer surface area of the thermoplate, that is considered to be a three-dimensional wavy surface, can be approximated by employing different mathematical functions. If the welding spots are arragned in a staggered manner, Figure 4.1a, this surface can be represented by trigonometrical functions in the following manner:

$$y = \pm\frac{\delta}{4}\left(1 + \cos\left(\frac{2\pi}{s_L}x\right)\cos\left(\frac{\pi}{s_T}z\right)\right), \tag{4.1}$$

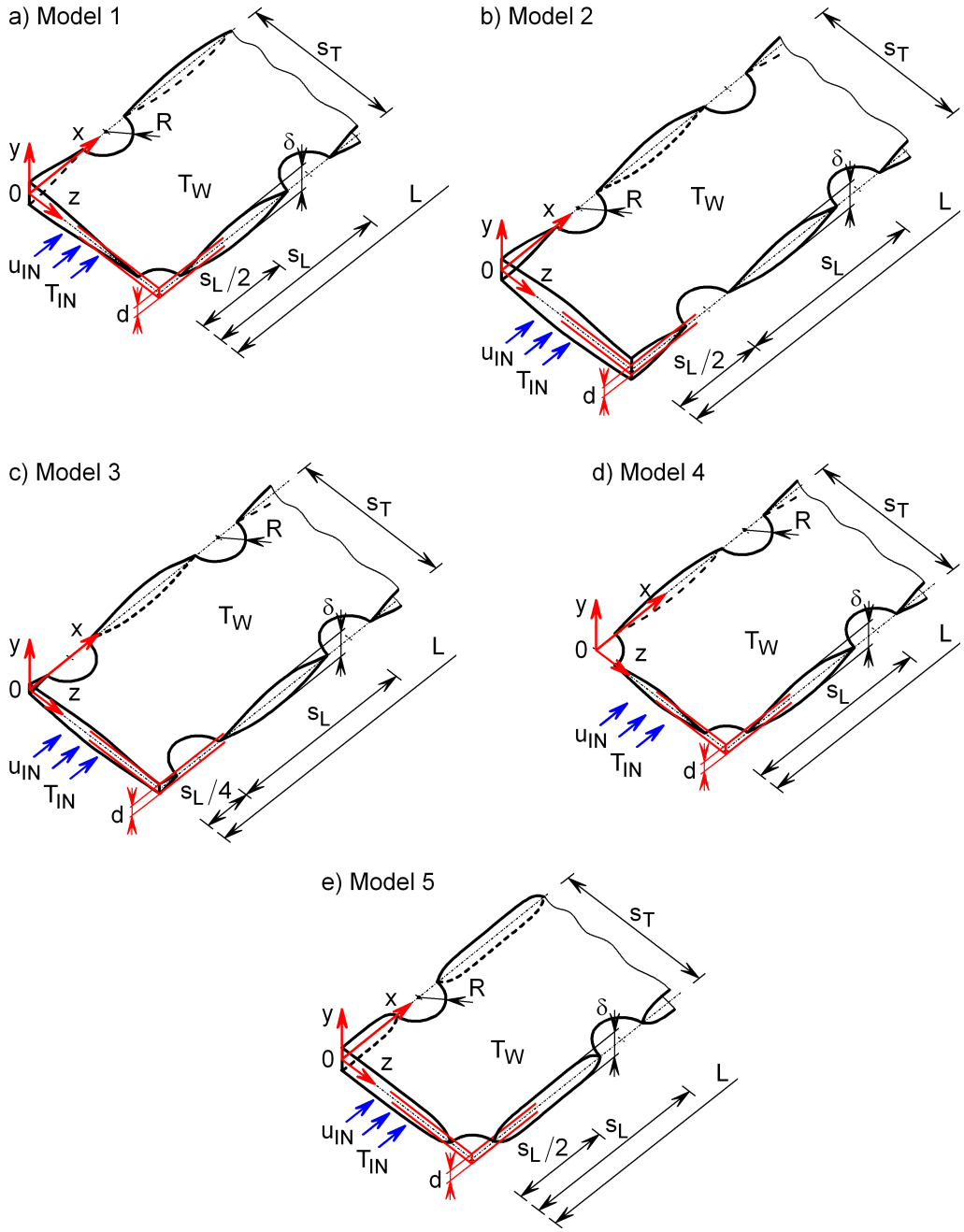

Figure 4.1: Geometry and dimensions of the three-dimensional simulated domain; a) welding spots arrangend in a staggered manner, Equation 4.1, b) parallel welding spots, Equation (4.2) with $C = s_L/2$, c) parallel welding spots, Equation (4.2) with $C = s_L/4$, d) parallel welding spots, Equation (4.2) with $C = 0$, and e) thermoplate surface defined using the exponential function (4.4).

where the sign + is used for the upper, and − for the lower surface, respectively, and the geometrical parameters δ, s_L and s_T can be taken from Figure 4.1. For welding spots arranged in parallel, Figure 4.1b, c and d, the following expression is applied

$$y = \pm\frac{\delta}{8}\left(2 - \cos\left(\frac{2\pi}{s_L}(x - C)\right) - \cos\left(\frac{2\pi}{s_T}z\right)\right). \tag{4.2}$$

The cross-section area of the model with staggered welding spots, Figure 4.1a, is nearly independent on x (in this case, it changes slightly only in the welding spots regions), while at models with parallel welding spots it changes with x-coordinate noticeable. The size of the inlet surface can be adjusted by constant C. In case of $C = 0$, Figure 4.1d, the inlet surface is minimal and if $C = s_L/2$ it is maximal, Figure 4.1b. For $C = s_L/4$ or $C = 3s_L/4$, the inlet surface of the model with parallel welding spots is in between of those with $C = 0$ and $C = s_L/2$ and is nearly same as the one of the model with staggered arangement of the welding spots, Figure 4.1c.

The computational domain is determinated in each case by the surface $y = f(x, z)$ according to the Equation (4.1) or (4.2), the planes $x = 0$ and $x = L$, the symmetry planes $y = 0$, $z = 0$ and $z = s_T$ or $z = s_T/2$ for models with staggered and parallel welding spots, respectively, and the cylindrical surfaces

$$(x - x_{0i})^2 + (z - z_{0i})^2 = R^2, \tag{4.3}$$

where x_{0i} and z_{0i} are the centres of the welding spots obtained as the roots of the equation $y = f(x, z) = 0$ representing the heat transfer wavy surface according to the Equation (4.1) or (4.2).

However, the heat transfer surface area can be described also using other types of mathematical functions, i.g.:

$$y = \pm\frac{\delta}{2}\left(1 - \sum_{i=1}^{N}\exp\left(-D\left((x - x_{0i})^2 + (z - z_{0i})^2\right)\right)\right), \tag{4.4}$$

where N represents the total number of welding spots, D is a positive constant, x_{0i} and z_{0i} are the coordinates of the welding spot centres, which can be arranged freely in this case, in a staggered, parallel or any other manner, and have to be defined previously. Choosing an appropriate value D the curvature of the heat transfer surface can be changed. Due to the asymptotic features of the exponential function, the hight of the channel defined using Equation (4.4) is always slightly smaller than δ, which can be neglected in the engineering practice, for sufficient high value of constant D. An example of the thermoplate surface defined using the exponential function (4.4) is illustrated schematically in Figure 4.1e.

In this context, it is to be noted that the mathematical contour of the thermoplate according to Equations (4.1), (4.2) and (4.4) does not ideally represent the reality, but the discrepancy as regards the thermohydraulic behaviour of the system is expected to be of a marginal importance.

The objective of this numerical analysis is to numerically find out the influence of the thermoplate geometry on the heat transfer and pressure drop. Based on the thermoplate that was used in the laboratory for the experimental research [38], whose geometry was approximated by the Equation (4.1), only one of the geometrical parameter, s_L, s_T, or δ, Figure 4.1a, and the Reynolds number have been varied firstly, whereas the other two parameters have been kept constant, as it is specified in the Table 4.1.

Table 4.1: Parameter combinations for the numerical experiments.

s_L[mm]	s_T[mm]	δ[mm]	L[mm]	Re
$28 \div 112$	36	3.4	500	$50 \div 4000$
42	$20 \div 50$	3.4	500	$50 \div 4000$
42	36	$2.5 \div 8.4$	500	$50 \div 4000$

Although there are 21 different Models at 11 different Reynolds Numbers according to the Table 4.1, which results in 231 numerical experiments, this parameter combination does not suffice for a Nusselt number and pressure drop correlations to be stated, which belongs to the objectives of this thesis as well.

For that reason, the parameter combination from the Table 4.1 has been supplemented to some extent, Table 4.2.

Table 4.2: Extended parameter combinations for the numerical experiments.

s_L[mm]	s_T[mm]	δ[mm]	L[mm]	Re
$28 \div 112$	$20 \div 50$	$2.5 \div 8.4$	500	$50 \div 3000$

Additionaly, a comparison between different thermoplate geometries and welding spots arrangements, Figure 4.1 had to be made, Table 4.3.

Table 4.3: Different model geometries.

Model	s_L[mm]	s_T[mm]	δ[mm]	L[mm]	Re
Equation (4.1), Figure 4.1a	40	35	4	300	$50 \div 2000$
Equation (4.2), Figure 4.1b	40	35	4	300	$50 \div 2000$
Equation (4.2), Figure 4.1c	40	35	4	300	$50 \div 2000$
Equation (4.2), Figure 4.1d	40	35	4	300	$50 \div 2000$
Equation (4.4), Figure 4.1e	40	35	4	300	$50 \div 2000$

Further, the influence of time fluctuations of the fluid velocity at the inlet on the heat transfer in thermoplate is to be investigated, as it is stated in Table 4.4.

Table 4.4: Inlet velocity for time dependent fluid flows.

u_{IN}[m/s]	s_L[mm]	s_T[mm]	δ[mm]	L[mm]	Re
0.1	40	35	4	300	450
$0.1\,(1 + 0.2\,(sin(100t)))$	40	35	4	300	450
$0.1 + 0.04 \sum_{n=0}^{\infty} H(t - \frac{n\pi}{100})$	40	35	4	300	450

To find out the influence of the thermally asymmetric boundary conditions on the heat transfer in thermoplates and to compare it to the heat transfer in a parallel plate channel under the same boundary conditions, Chapter 3, the models defined in Table 4.5 are to be simulated.

Table 4.5: Thermally asymmetric boundary conditions.

T_{W1}[K]	T_{W2}[K]	s_L[mm]	s_T[mm]	δ[mm]	L[mm]	Re
333	293	40	35	4	300	$50 \div 2000$
333	303	40	35	4	300	$50 \div 2000$
333	306.33	40	35	4	300	$50 \div 2000$
333	317	40	35	4	300	$50 \div 2000$
333	319.67	40	35	4	300	$50 \div 2000$
333	325	40	35	4	300	$50 \div 2000$
333	343	40	35	4	300	$50 \div 2000$
333	353	40	35	4	300	$50 \div 2000$

4.2 The physical model

The fluid flow was considered to be laminar, single phase, incompressible and three-dimensional. The velocity, pressure and temperature fields are governed by the well

known equations of continuity, momentum and energy

$$\frac{\partial \rho}{\partial t} + \nabla \cdot (\rho \boldsymbol{w}) = 0, \tag{4.5}$$

$$\rho \frac{D\boldsymbol{w}}{Dt} = -\nabla p - \nabla \cdot \boldsymbol{\tau} + \rho \boldsymbol{f}, \tag{4.6}$$

$$\rho c_v \frac{DT}{Dt} = -\nabla \cdot \dot{\boldsymbol{q}} - T \left(\frac{\partial p}{\partial T} \right)_\rho (\nabla \cdot \boldsymbol{w}) - (\boldsymbol{\tau} : \nabla \boldsymbol{w}), \tag{4.7}$$

where ρ denotes fluid density, c_v the specific heat capacity, $\boldsymbol{w}$ the velocity vector, $\dot{\boldsymbol{q}}$ the heat flux vector, $\boldsymbol{\tau}$ the stress tensor, T the temperature, p the pressure and $\boldsymbol{f}$ the body force. By the derivation of the energy equation 4.7, the equation

$$i = i(v, T), \tag{4.8}$$

was used, where i represents the specific internal energy and v the specific volume. In case of compressible flows, an additional equation, the thermal equation of state

$$p = p(v, T), \tag{4.9}$$

is needed to close the system of the equations.

In order to use the Equations (4.5) to (4.7), the stress ternsor must be expressed in terms of velocity gradients and the heat flux vector in terms of temperature gradients [4]. For Newtonian fluids the components of the stress tensor $\boldsymbol{\tau}$ in the Cartesian coordinate system are:

$$\tau_{xx} = -2\mu \frac{\partial u}{\partial x} + \frac{2}{3}\mu(\nabla \cdot \boldsymbol{w}), \tag{4.10}$$

$$\tau_{yy} = -2\mu \frac{\partial v}{\partial y} + \frac{2}{3}\mu(\nabla \cdot \boldsymbol{w}), \tag{4.11}$$

$$\tau_{zz} = -2\mu \frac{\partial w}{\partial z} + \frac{2}{3}\mu(\nabla \cdot \boldsymbol{w}), \tag{4.12}$$

$$\tau_{xy} = \tau_{yx} = -\mu \left(\frac{\partial u}{\partial y} + \frac{\partial v}{\partial x} \right), \tag{4.13}$$

$$\tau_{yz} = \tau_{zy} = -\mu \left(\frac{\partial v}{\partial z} + \frac{\partial w}{\partial y} \right), \tag{4.14}$$

$$\tau_{zx} = \tau_{xz} = -\mu \left(\frac{\partial w}{\partial x} + \frac{\partial u}{\partial z} \right). \tag{4.15}$$

Here are u, v and w components of the velocity vector $\boldsymbol{w}$ in x, y and z direction respectively and μ the dynamic viscosity.

Using the Fourier's low of heat conduction for constant k

$$\dot{\boldsymbol{q}} = -k\nabla T, \tag{4.16}$$

where k represents the thermal conducivity, and properties of the stress tensor (4.10 to 4.15) the governing equations (4.5) to (4.7) become:

$$\frac{\partial \rho}{\partial t} + \frac{\partial(\rho u)}{\partial x} + \frac{\partial(\rho v)}{\partial y} + \frac{\partial(\rho w)}{\partial z} = 0, \tag{4.17}$$

$$\rho\left(\frac{\partial u}{\partial t} + u\frac{\partial u}{\partial x} + v\frac{\partial u}{\partial y} + w\frac{\partial u}{\partial z}\right) = -\frac{\partial p}{\partial x} + \mu\left(\frac{\partial^2 u}{\partial x^2} + \frac{\partial^2 u}{\partial y^2} + \frac{\partial^2 u}{\partial z^2}\right) + \rho f_x, \tag{4.18}$$

$$\rho\left(\frac{\partial v}{\partial t} + u\frac{\partial v}{\partial x} + v\frac{\partial v}{\partial y} + w\frac{\partial v}{\partial z}\right) = -\frac{\partial p}{\partial y} + \mu\left(\frac{\partial^2 v}{\partial x^2} + \frac{\partial^2 v}{\partial y^2} + \frac{\partial^2 v}{\partial z^2}\right) + \rho f_y, \tag{4.19}$$

$$\rho\left(\frac{\partial w}{\partial t} + u\frac{\partial w}{\partial x} + v\frac{\partial w}{\partial y} + w\frac{\partial w}{\partial z}\right) = -\frac{\partial p}{\partial z} + \mu\left(\frac{\partial^2 w}{\partial x^2} + \frac{\partial^2 w}{\partial y^2} + \frac{\partial^2 w}{\partial z^2}\right) + \rho f_z, \tag{4.20}$$

$$\rho c_v\left(\frac{\partial T}{\partial t} + u\frac{\partial T}{\partial x} + v\frac{\partial T}{\partial y} + w\frac{\partial T}{\partial z}\right) = k\left(\frac{\partial^2 T}{\partial x^2} + \frac{\partial^2 T}{\partial y^2} + \frac{\partial^2 T}{\partial z^2}\right) + \mu\Phi \tag{4.21}$$

$$- T\left(\frac{\partial p}{\partial T}\right)_\rho \left(\frac{\partial u}{\partial x} + \frac{\partial v}{\partial y} + \frac{\partial w}{\partial z}\right), \tag{4.22}$$

where f_x, f_y and f_z represent the components of the body force vector $\boldsymbol{f}$ and the dissipation function Φ is defined as follows

$$\begin{aligned}\Phi =& 2\left(\left(\frac{\partial u}{\partial x}\right)^2 + \left(\frac{\partial v}{\partial y}\right)^2 + \left(\frac{\partial w}{\partial z}\right)^2\right) \\ &+ \left(\left(\frac{\partial u}{\partial y} + \frac{\partial v}{\partial x}\right)^2 + \left(\frac{\partial u}{\partial z} + \frac{\partial w}{\partial x}\right)^2 + \left(\frac{\partial v}{\partial z} + \frac{\partial w}{\partial y}\right)^2\right) \\ &- \frac{2}{3}\left(\frac{\partial u}{\partial x} + \frac{\partial v}{\partial y} + \frac{\partial w}{\partial z}\right)^2.\end{aligned} \tag{4.23}$$

To complete the set of the equations, the model equations (4.17) to (4.21) are

subject to the following boundary coditions:

$$x = 0 : \boldsymbol{w} = \{u_{IN}, 0, 0\}, T = T_{IN}; \qquad x = L : \frac{\partial \boldsymbol{w}}{\partial x} = 0, \frac{\partial T}{\partial x} = 0, \tag{4.24}$$

$$y = 0 : \frac{\partial \boldsymbol{w}}{\partial y} = 0, \frac{\partial T}{\partial y} = 0; \qquad y = f(x, z) : \boldsymbol{w} = 0, T = T_W, \tag{4.25}$$

$$z = 0 : \frac{\partial \boldsymbol{w}}{\partial z} = 0, \frac{\partial T}{\partial z} = 0; \qquad z = s_T : \frac{\partial \boldsymbol{w}}{\partial z} = 0, \frac{\partial T}{\partial z} = 0. \tag{4.26}$$

For the models with parallel welding spots, Figure 4.1, there is an additional symmetry plane at $z = s_T/2$, which is used to economise the calculations. In this case, instead of the conditions (4.26), following conditions are used:

$$z = 0 : \frac{\partial \boldsymbol{w}}{\partial z} = 0, \frac{\partial T}{\partial z} = 0; \qquad z = \frac{s_T}{2} : \frac{\partial \boldsymbol{w}}{\partial z} = 0, \frac{\partial T}{\partial z} = 0. \tag{4.27}$$

The small cylindrical surfaces representing the welding spots according to the Equation (4.3) are kept adiabatic

$$(x - x_{0i})^2 + (z - z_{0i})^2 = R^2 : \boldsymbol{w} = 0, \frac{\partial T}{\partial n} = 0, \tag{4.28}$$

where n represents a coordinate normal to the cylindrical surfaces.

By the conditions (4.24), the momentum and heat transfer in the streamwise direction at $x = L$ are neglected. Clearly, this simplification is not met in reality, but the errors thus introduced affect the corresponding fields only in the immediate vicinity of the channel outlet. The pressure boundary at $x = L$ was not used because of its negative inpact on the calculating time.

In the practice the walls of the thermoplate wavy channel are usually at different temperatures. The thermal asymmetry in parallel plate channel, which is used as a reference for comparison, was analysed in the Chapter 3. If the lower and the upper wall of the wavy cannel are kept at different temperatures, the symmetry plane at $y = 0$ and the boundary conditions (4.25) are invalid. Instead, the following conditions would be required:

$$y = -f(x, z) : \boldsymbol{w} = 0, T = T_{W1}; \qquad y = f(x, z) : \boldsymbol{w} = 0, T = T_{W2}, \tag{4.29}$$

where T_{W1} and T_{W2} are the temperatures of the lower and of the upper wall, respectively. Note that the lower and the upper thermoplate surface do not touch each other, because the adiabatic cylindrical surface (4.3) is placed in between. That allows the lower and the upper wall to have different temperatures, without any singularity problems.

The governing equations are solved using a commercial software StarCD by CD-adapco. A brief overview of the numerical methods used by this programme is given in Appendix A.

An example of the thermoplate model definition in StarCD using input files is illustrated in Appendix B. In this program, the thermoplate surface is approximated using Equation 4.1, without the symmetry plane at $y = 0$ and the wall temperatures cann be different and specified by user, as well as other geometrical and process parameters. Not only a thermoplate strip, but also the whole thermoplate with connecting tubes cann be modelled by choosing appropriate values of the parameters. For other thermoplate geometries or welding pattern, similar programmes have been used.

4.3 Process quantities

4.3.1 Symmetric heated channels

Once the governing equations are solved and the flow, the pressure and the temperature fields are obtained, which makes possible the definition of other very important process quantities.

The fluid bulk temperature (also called the mixing cup temperature), $T_b(x)$, and the local wall heat flux, $\dot{q}_W(x)$, averaged in spanwise (z) direction, can be calculated by

$$T_b(x) = \frac{\int_S uT dS}{\int_S u dS}, \tag{4.30}$$

$$\dot{q}_W(x) = \frac{1}{A_{SW}} \int_{A_{SW}} (\dot{\boldsymbol{q}} \cdot \boldsymbol{n}) dA_{SW}, \tag{4.31}$$

where $S = S(x)$ represents the cross-sectional flow area of the channel, $A_{SW} = A_{SW}(x)$ a narrow strip of the thermoplate surface $y = f(x, z)$ bounded by the planes $x - (\varepsilon/2)$ and $x + (\varepsilon/2)$, ε being the width of the numerical cell in the x-direction.

The heat flow rate, $\dot{Q}(x)$, and the average wall heat flux, $\dot{q}_{mW}(x)$, are obtained in a similar way

$$\dot{Q}_W(x) = \int_{A_W} (\dot{\boldsymbol{q}} \cdot \boldsymbol{n}) dA_W, \qquad \dot{q}_{mW}(x) = \frac{\dot{Q}_W(x)}{A_W} = \frac{1}{A_W} \int_{A_W} (\dot{\boldsymbol{q}} \cdot \boldsymbol{n}) dA_W, \tag{4.32}$$

where $A_W = A_W(x)$ denotes the heat transfer area according to the thermoplate surface $y = f(x, z)$, from the very beginning of the thermoplate, $x = 0$, to the current position $x + \varepsilon/2$.

The local and the average heat transfer coefficients, $h_W(x)$ and $h_{mW}(x)$, are defined by

$$h_W(x) = \frac{\dot{q}_W(x)}{T_W - T_b(x)}, \qquad h_{mW}(x) = \frac{1}{x} \int_0^x h_W(\xi) d\xi, \tag{4.33}$$

with $T_b(x)$ and $\dot{q}_W(x)$ according to Equations (4.30) and (4.31); T_W represents the wall temperature, that does not change with any coordinate in this analysis.

The average heat transfer coefficient, $h_{mW}(x)$, defined according to the Equation (4.33) can be calculated if the distribution of the local heat transfer coefficient $h_W(x)$ is known, which is the case in this numerical analysis. However, if these numerical results are to be compared with the experimental ones, some difficulties could be experienced, because, the average heat flux and the fluid temperature at the inlet and at the outlet are measured in experiments rather than the temperature distribution of the flowing fluid through the whole thermoplate and the heat flux distribution on its surface. This would be either impossible or too expensive. For that reason, another definition of the heat transfer coefficient is proposed:

$$h_{mW} = \frac{\dot{q}_{mW}}{\Delta T_m}, \tag{4.34}$$

where h_{mW} and $\dot{q}_{mW}$ denote the average heat transfer coefficient and the average heat flux for the whole thermoplate, respectively, and ΔT_m represents the average temperature difference between the thermoplate surface and the fluid. This temperature difference can be calculated as follows

$$\Delta T_m = \frac{1}{L}\int_0^L (T_W - T_b(x))\, dx = T_W - T_{bm}, \tag{4.35}$$

where L represents the thermoplate length, $T_b(x)$ the fluid temperature according to the Equation (4.30) and T_{bm} the mean fluid temperature in whole thermoplate. However, this average temperature difference (4.35) suffers from a lack of being inapplicable for comparison with exmerimental results, for the same reasons as it is the case with the average heat transfer coefficient, $h_{mW}(x)$, discussed above. An acceptable average temperature difference can be deduced from the heat transfer balance, writing it first in infinitesimal form, [38]:

$$d\dot{Q}_W = \dot{m}c_p dT = h_{mW}(T_W - T_b(x))dA, \tag{4.36}$$

and than in integral form

$$\dot{Q}_W = \dot{m}c_p(T_{OUT} - T_{IN}) = h_{mW}\Delta T_m A, \tag{4.37}$$

where $\dot{m}$ and A represent the mass flow rate of the fluid through the thermoplate and thermoplate surface, respectively. Integrating the Equation (4.36) from the inlet to the outlet gives:

$$h_{mW} = \frac{\dot{m}c_p}{A} ln \frac{T_W - T_{IN}}{T_W - T_{OUT}}, \tag{4.38}$$

where $T_b(0) = T_{IN}$ and $T_b(L) = T_{OUT}$. Combining the Equations (4.38) and (4.37) enables calculating of the average temperature difference, also called the logaritmic mean temperature difference (LMTD), as follows:

$$\Delta T_m = \frac{T_{OUT} - T_{IN}}{ln\frac{T_W - T_{IN}}{T_W - T_{OUT}}}. \tag{4.39}$$

This logarithmic mean temperature difference depends only on the fluid themperatures at the inlet and outlet, and the wall temperature. However, the temperature difference, ΔT_m, calculated according to Equation (4.39) does not take into account any changes of fluid properties and heat transfer coefficient along the channel. For that reason a generalised mean temperature difference, that would take into these changes, is often recommended, e.g. by Utamura et al. [67]. To employ this generalisation method one would need some other experimental data of the heat exchanger, and the generalised mean temperature difference would have to be calculated numerically. This is, however, beyond the scope of this thesis.

The local and the average Nusselt numbers, $Nu_W(x)$ and $Nu_{mW}(x)$, are obtained from

$$Nu_W(x) = \frac{h_W(x)d_h}{k}, \qquad Nu_{mW}(x) = \frac{h_{mW}(x)d_h}{k}, \tag{4.40}$$

with d_h as the hydraulic diameter

$$d_h = \frac{4S}{U} = 2d, \tag{4.41}$$

S being the cross-sectional flow area, U its circumference, and d the distance between the parallel plates channel having the same volume V as the actual thermoplate

$$d = \frac{V}{s_T L}. \tag{4.42}$$

Note that the hydraulic diameter d_h defined in this way does not change along the channel length.

A further quantity involved in the presentation of the results is the Reynolds number,

$$Re = \frac{\bar{u}d_h}{\nu}, \tag{4.43}$$

where $\bar{u}$ is the average axial velocity component, and ν the kinematic viscosity.

In order to obtain a thermo-fluid characteristic of the thermoplate, the local pressure, $p(x)$, averaged in the plane $y0z$ and the pumping power, P, are calculated as follows

$$p(x) = \frac{1}{S}\int_S p dS, \tag{4.44}$$

$$P(x) = (p(0) - p(x))\dot{V}, \tag{4.45}$$

where $p(0) = p_{IN}$ and $p(x)$ are the averaged inlet pressure and the average pressure at distance x from the inlet, respectively; $\dot{V}$ denotes the volume flow rate (for $x = L$ we have $p_m(L) = p_{OUT}$, L being the channel length).

4.3.2 Asymmetric heated channels

In the case of asymmetrical heating the symmetry plane at $y = 0$ and the boundary conditions (4.25) are not applicable. Instead, the conditions (4.29) have to be employed. Consequently, the quantities that are calculated at the upper and at the lower thermoplate surface, (4.31 to 4.40), will not have the same values, as in the case of the symmetrical heating, and have to be defined separately.

The local heat flux at the lower wall, $y = -f(x, z)$, and at the upper wall, $y = f(x, z)$, is defined:

$$\dot{q}_{W1}(x) = \frac{1}{A_{SW1}} \int_{A_{SW1}} (\dot{\boldsymbol{q}} \cdot \boldsymbol{n}) dA_{SW1}, \tag{4.46}$$

$$\dot{q}_{W2}(x) = \frac{1}{A_{SW2}} \int_{A_{SW2}} (\dot{\boldsymbol{q}} \cdot \boldsymbol{n}) dA_{SW2}, \tag{4.47}$$

where A_{SW1} and A_{SW2} are, similar to A_{SW}, narrow strips of the thermoplate lower surface, $y = -f(x, z)$, and of the upper surface, $y = f(x, z)$, respectively, bounded by the planes $x - (\varepsilon/2)$ and $x + (\varepsilon/2)$.

Similar, the average wall heat flux and the heat flow rate at the lower and at the upper wall are:

$$\dot{q}_{mW1}(x) = \frac{1}{A_{W1}} \int_{A_{W1}} (\dot{\boldsymbol{q}} \cdot \boldsymbol{n}) dA_{W1}, \qquad \dot{Q}_{W1}(x) = \int_{A_{W1}} (\dot{\boldsymbol{q}} \cdot \boldsymbol{n}) dA_{W1}, \tag{4.48}$$

$$\dot{q}_{mW2}(x) = \frac{1}{A_{W2}} \int_{A_{W2}} (\dot{\boldsymbol{q}} \cdot \boldsymbol{n}) dA_{W2}, \qquad \dot{Q}_{W2}(x) = \int_{A_{W2}} (\dot{\boldsymbol{q}} \cdot \boldsymbol{n}) dA_{W2}, \tag{4.49}$$

where A_{W1} and A_{W2} are the lower and the upper wall surface, respectively, in range between $x = 0$ and $x + \varepsilon/2$.

The local and the mean heat transfer coefficients at the lower and at the upper thermoplate surface become

$$h_{W1}(x) = \frac{\dot{q}_{W1}(x)}{T_{W1} - T_b(x)}, \qquad h_{mW1}(x) = \frac{1}{x} \int_0^x h_{W1}(\xi) d\xi, \tag{4.50}$$

$$h_{W2}(x) = \frac{\dot{q}_{W2}(x)}{T_{W2} - T_b(x)}, \qquad h_{mW2}(x) = \frac{1}{x} \int_0^x h_{W2}(\xi) d\xi. \tag{4.51}$$

Since there are no experimental data available on asymmetric heated thermoplates, no other definitions of the average heat transfer coefficient are considered.

Finaly, the Nusselt number at the lower and at theupper thermoplate surface are defined as follows:

$$Nu_{W1}(x) = \frac{h_{W1}(x)d_h}{k}, \qquad Nu_{mW1}(x) = \frac{h_{mW1}(x)d_h}{k}, \tag{4.52}$$

$$Nu_{W2}(x) = \frac{h_{W2}(x)d_h}{k}, \qquad Nu_{mW2}(x) = \frac{h_{mW2}(x)d_h}{k}. \tag{4.53}$$

All the process quantities defined in this section are calculated in post-processing part of the simulations with StarCD using a Fortran subroutine POSDAT.f, Appendix C. Similar program have been used for transient calculations.

The dependency of the heat transfer coefficient on the size of the numerical mesh is diskussed in Appendix D.

5 Results

Because of the complex geometry of the computational domain, all the vector quantities obtained from the governing equations are three-dimensional. This poses some difficulties on the presentation of the results. For this reason, the interesting quantities will be visualised in the following as general images and quantitatively illustrated in characteristic planes or on surfaces, for one specific channel, i.e. for one combination of the geometrical parameters $\delta = 3.4$ mm, $s_L = 42$ mm, $s_T = 36$ mm, $R = 5$ mm and $L = 500$ mm, Figure 4.1a. For other parameter combinations the similar flow behaviour was observed.

5.1 Symmetric heated channels, steady state flows

5.1.1 The velocity field

The development of the velocity field in the symmetry plane $y = 0$ at different Reynolds numbers is shown in Figure 5.1. At the smallest Reynolds number adopted in the numerical experiments, $Re = 50$, the velocity field is largely smooth with relatively small separation zones that are established behind the welding spots. Nevertheless, the velocity fluctuations both in the transversal, z, and axial, x, direction are observed.

Increasing the Reynolds number the separation zones grow in the region between the welding spots that are placed one behind another, finally reaching the next welding spot. This is already the case at $Re = 500$, Figure 5.2. With the strictly laminar flow, the fluid is recirculating and detained in these zones. The thermoplate surface area corresponding to these recirculation zones is expected to be less effective for the heat transfer.

At the Reynolds number $Re = 4000$ the fluid separation establishes between the welding spots with reattachments at the contour of the neighbouring, downstream spots, and a comparatively large portion of the channel is occupied by recirculation zones. In the middle of the channel, there is a meandering fluid core that is bounded by the recirculation zones and only touches the welding spots. Here is the velocity almost four times greater than the inlet fluid velocity.

Similar flow structures have been reported by Wang and Vanka [70], on the basis of the numerical experiments, and by Nishimura et al. [42] as well as by Rush et al. [52] in laboratory experiments, all using two-dimensional channels.

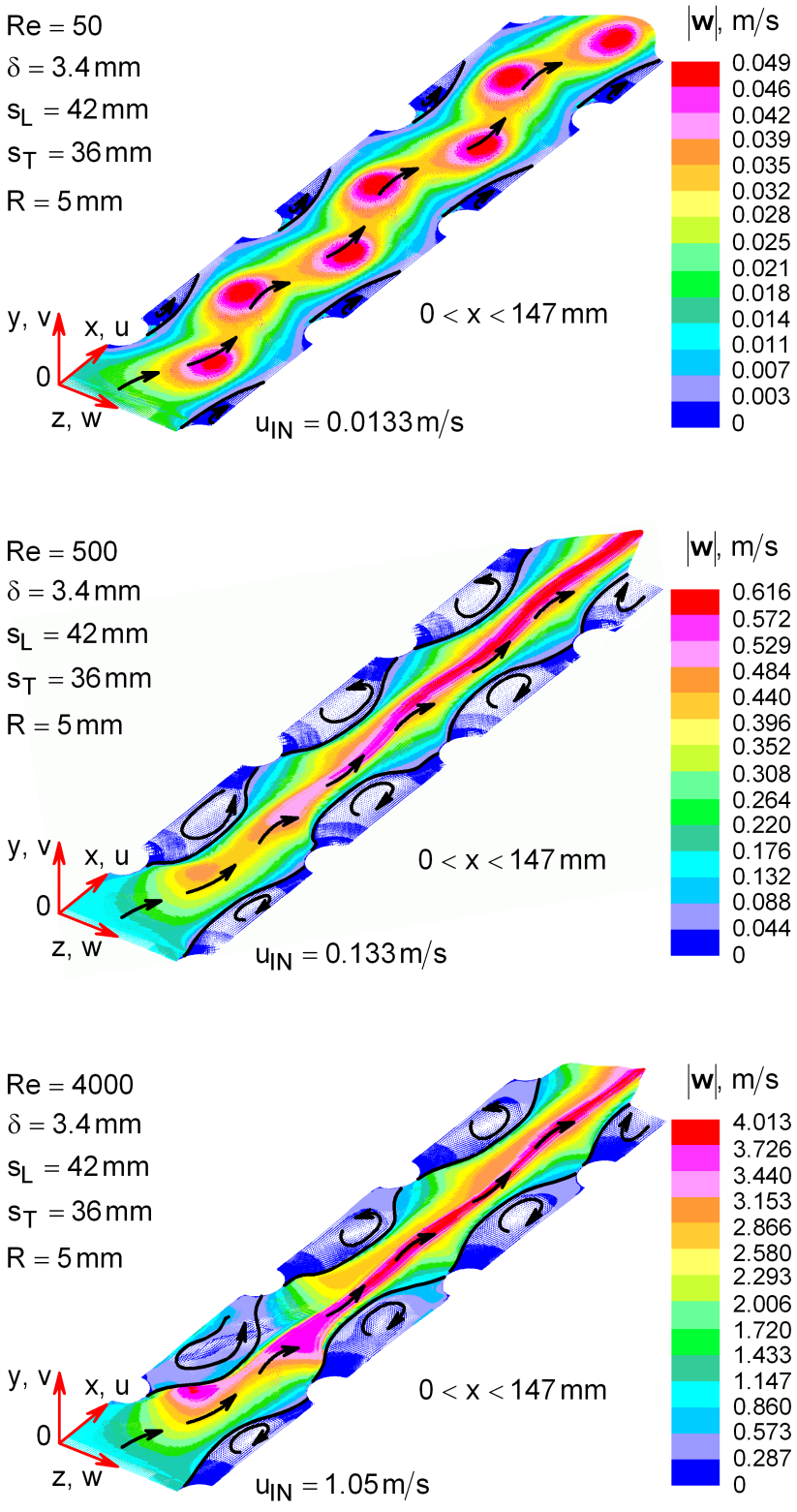

Figure 5.1: Velocity field in the symmetry plane $y = 0$ at different Reynolds numbers.

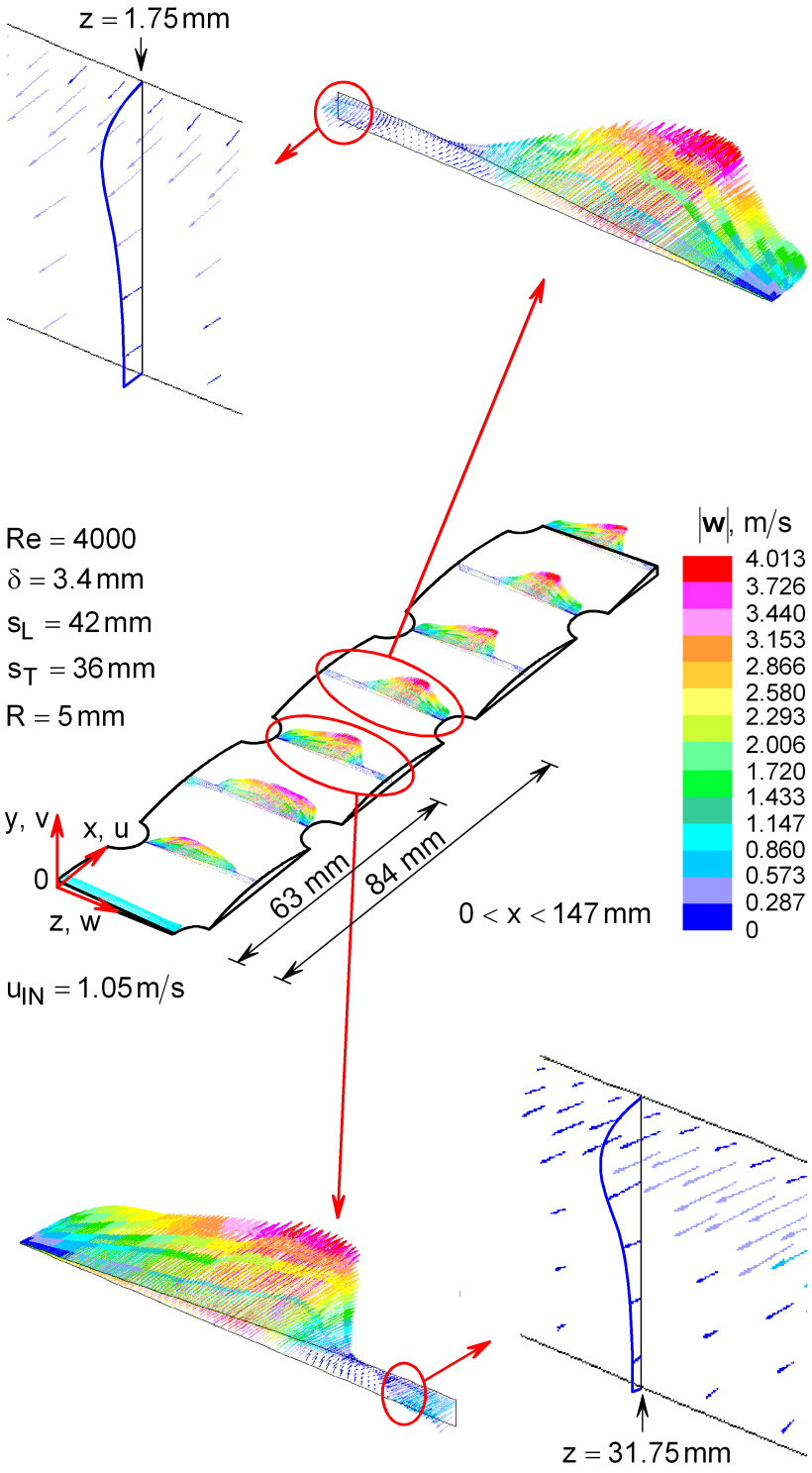

Figure 5.2: Velocity profiles in the welding spots cross-sections at $Re = 4000$.

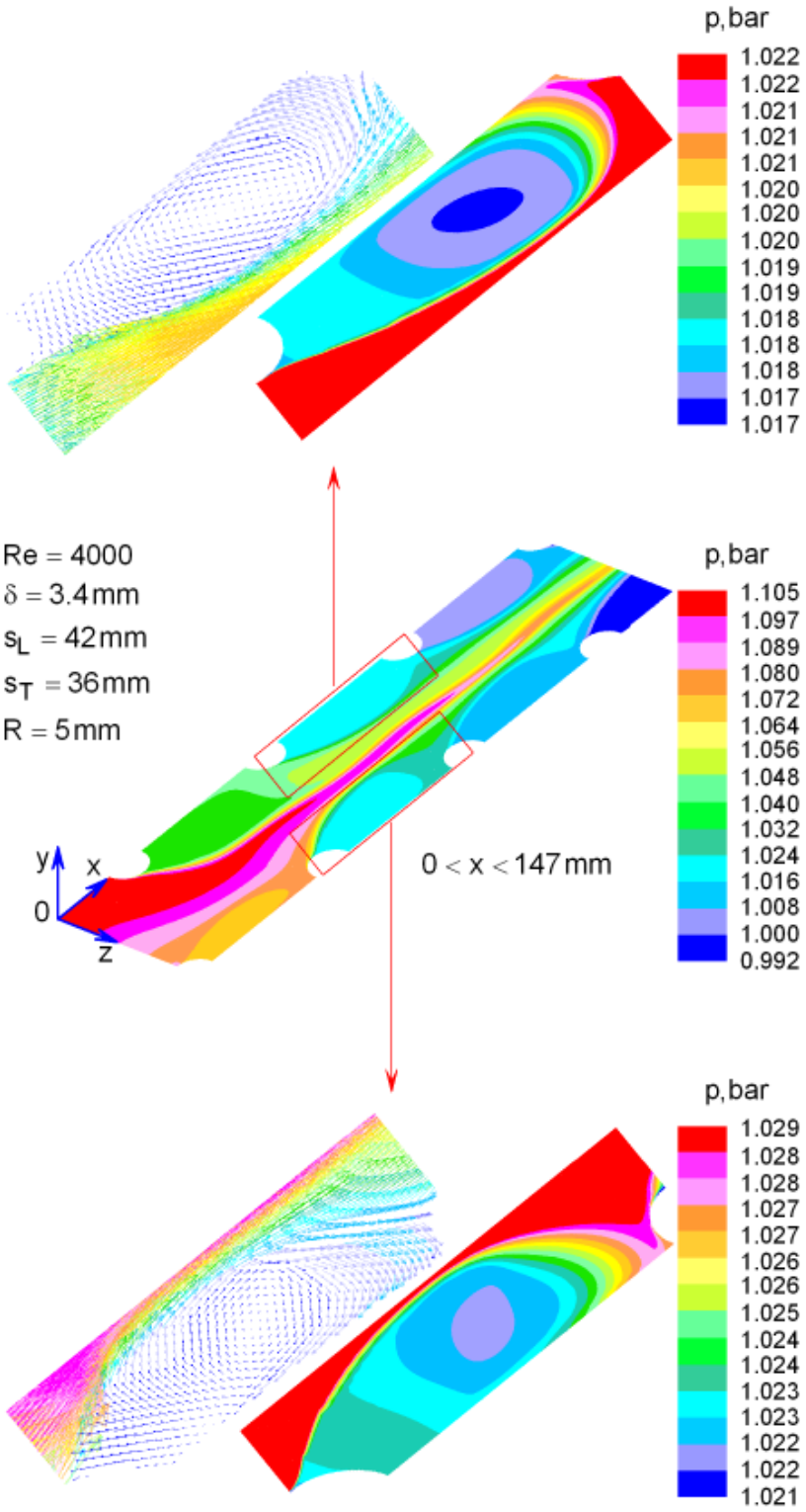

Figure 5.3: Pressure field in the symmetry plane $y = 0$ at $Re = 4000$ and its linkage with the velocity field.

As an example, Figure 5.2 provides an idea about the velocity profile in $y0z$ planes at different distance from the inlet (at the cross-sections where the welding spots are placed) for $Re = 4000$. A very strong velocity gradient is observed in the immediate vicinity of each welding spot, where the velocity jumps from zero on the welding spot rims, to a value of about 1.5 m/s. Somewhere in the middle of the channel, in the kernel flow region, the velocity reaches its maximum, and reverses on the opposite side to the welding spot in respect to z axis, where the fluid flow is dominated by an adverse pressure gradient, Figure 5.3. Interestingly, in the recirculation zones, the velocity maximum does not establish in the symmetry plane $x0z$, but is shifted towards the wall. The like is observed in the kernel flow near the boundary of the recirculation zone, Figure 5.3. This means that the velocity profiles in this case do not have a parabolic-like form with one maximum, but they have two inflection points with two local maxima and one local minimum, the latter being placed in the symmetry plane $y = 0$. Similar behaviour has also been observed by Mahmud et al. [29], Figure 2.9.

The distribution of the total pressure in the symmetry plane, $y = 0$, at $Re = 4000$, as well as its linkage to the velocity vector direction in the recirculation zones, is shown in Figure 5.3. In the middle of the channel, the pressure decreases with increasing distance from the channel inlet. However, in the recirculation zones the pressure is not monotonically decreasing function of x and it even increases with x in the regions, where the thermoplate walls converge, which is the case near the symmetry planes at $z = 0$ and $z = s_T$ next to each welding spot in upstream direction. This piecewise adverse pressure gradients cause fluid flow reversals, resulting in recirculation zones.

From Figure 5.2 one might infer that in the same cross-section turbulent flow may coexist with the laminar flow (apart from the viscous boundary layer in the near-wall regions). The extension of one flow mode occurs at the expenses of the other one, and turbulence will occupy the larger portion of the channel cross-section, the larger the Reynolds number. The curvature of the boundary is expected to support the generation of Görtler's vortices and hairpin vortex structures [16]. As a consequence, this would result in a stronger pressure drop and an improvement of heat transfer in comparison with those obtained from the purely laminar model. In this context it is to be noted that a possible laminar-turbulent flow transitions are disregarded in these simulations.

5.1.2 The temperature field and the heat flux at the thermoplate surface

Some insights into the development of the temperature field in the $x0z$ symmetry plane of the channel at different Reynolds numbers are given in Figure 5.4. The fluid enters the thermoplate at the inlet temperature $T_{IN} = 293$ K and is heated by the thermoplate walls, which are kept isothermal at $T_W = 333$ K.

At the Reynolds number $Re = 50$ the fluid temperature increases very rapidly and the thermal boundary layer penetrates the fluid bulk relatively fast, reaching the $x0z$

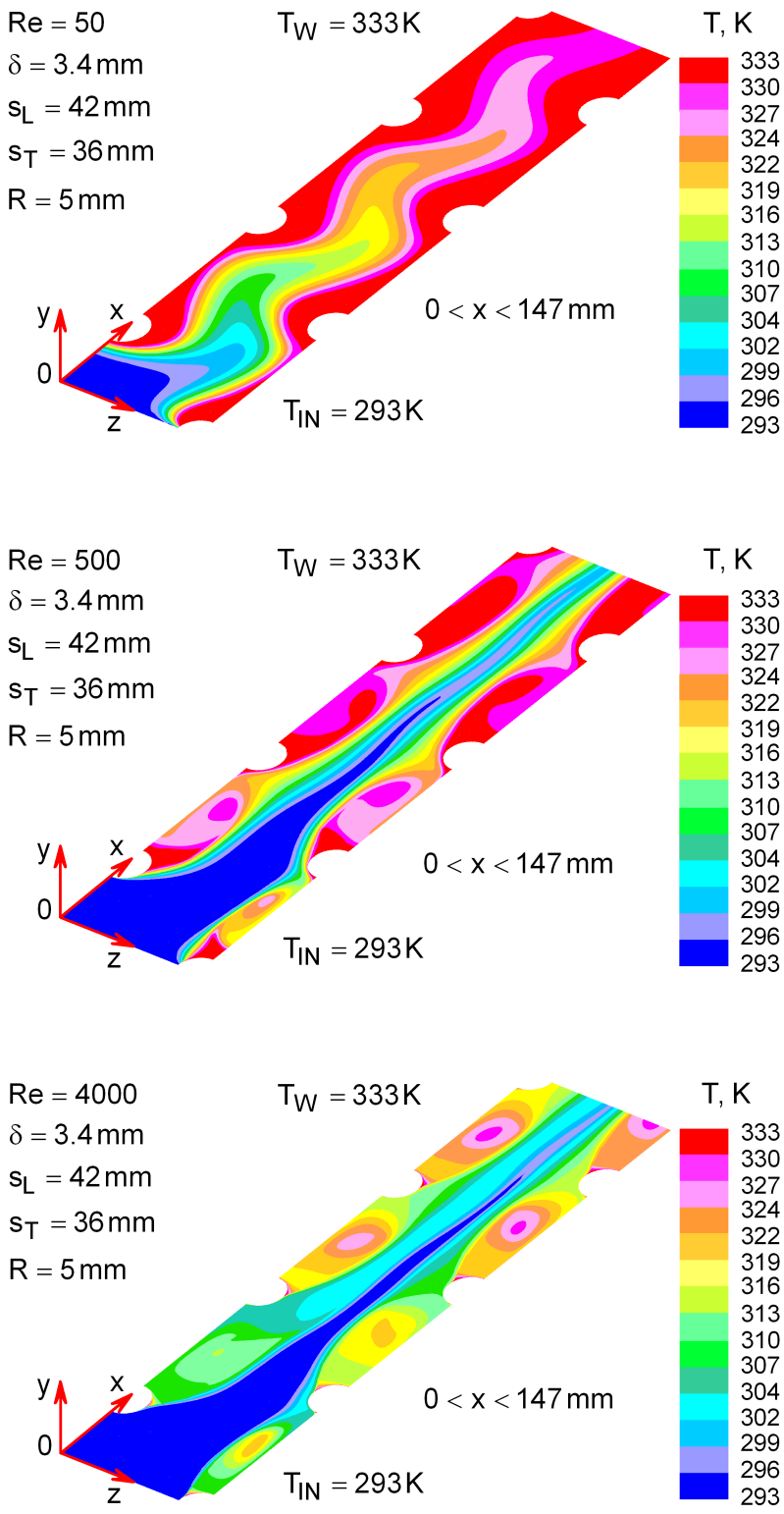

Figure 5.4: Temperature field in the symmetry plane $y = 0$ at different Reynolds numbers.

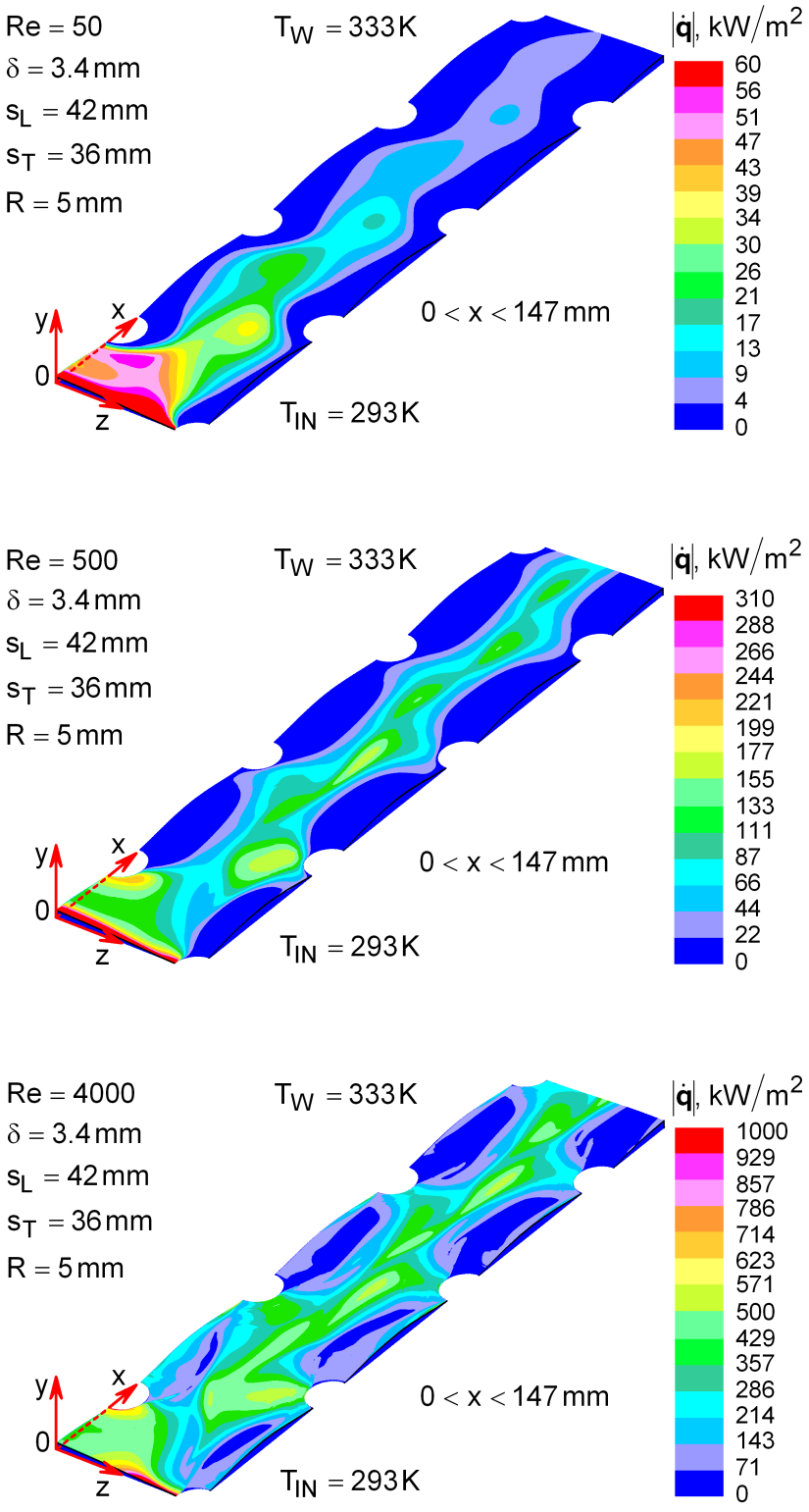

Figure 5.5: Wall heat flux at different Reynolds numbers.

plane downstream the channel inlet at a distance smaller than $s_L/2$. Near the welding spots and in the recirculation zones, the fluid approaches the temperature of the walls much faster than in the middle channel region.

Increasing the Reynolds number up to $Re = 500$, the temperature field changes significantly. In the central channel region, $z \approx s_T/2$, the fluid remains thermally unaffected by the heating plates, and the thermally developing region spreads up to $x \approx 2 \cdot s_L$. The recirculation zones are clearly recognised and the fluid reaches the temperature of the walls primarily behind the welding spots in the downstream direction and in the centres of the eddies, which is expected to reduce the heat transfer in these regions.

Further increasing of the Reynolds number up to $Re = 4000$ does not change the temperature field qualitatively. The thermally developing region occupies now a channel length of about $3 \cdot s_L$. The fluid velocity is high, so that the fluid, even in the recirculation zones is thermally active.

For better understanding of the heat transfer mechanism in thermoplates, the heat flux should be analysed in detail. Its distribution as a vector intensity, $|\,\dot{\boldsymbol{q}}\,|$, at different Reynolds numbers is illustrated in Figure 5.5. At all Reynolds numbers, the heat flux is seen to decrease in the streamwise, x, direction, becoming smaller in the recirculation zones, than in the central part of the strip. The heat flux fluctuates significantly not only in spanwise, but also in streamwise direction. The local heat flux maxima are situated upstream near the welding spots, since its local minima are placed behind the welding spots in the flow direction.

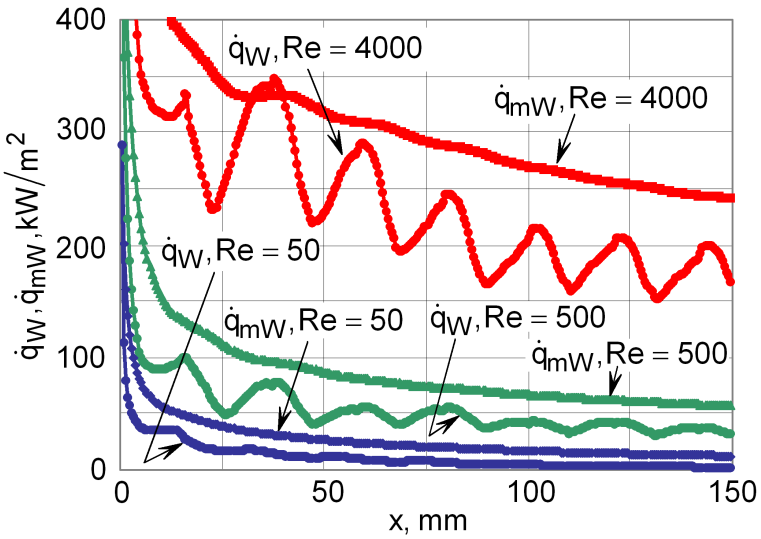

Figure 5.6: Local, spanwise averaged, heat flux, $\dot{q}_W = \dot{q}_W(x)$, and the mean heat flux, $\dot{q}_{mW} = \dot{q}_{mW}(x)$, according to Equations (4.31) and (4.32) at different Reynolds numbers.

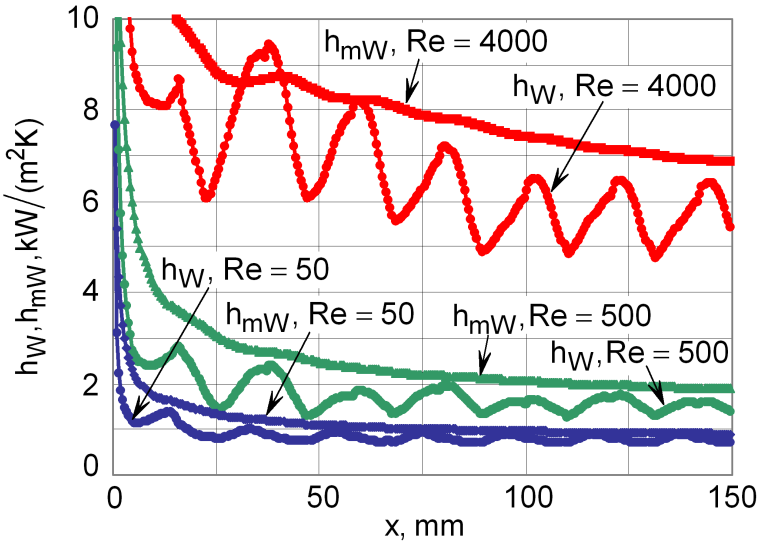

Figure 5.7: Local, spanwise averaged, heat transfer coefficient, $h_W = h_W(x)$, and the mean heat transfer coefficient, $h_{mW} = h_{mW}(x)$, according to the Equation (4.33) at different Reynolds numbers.

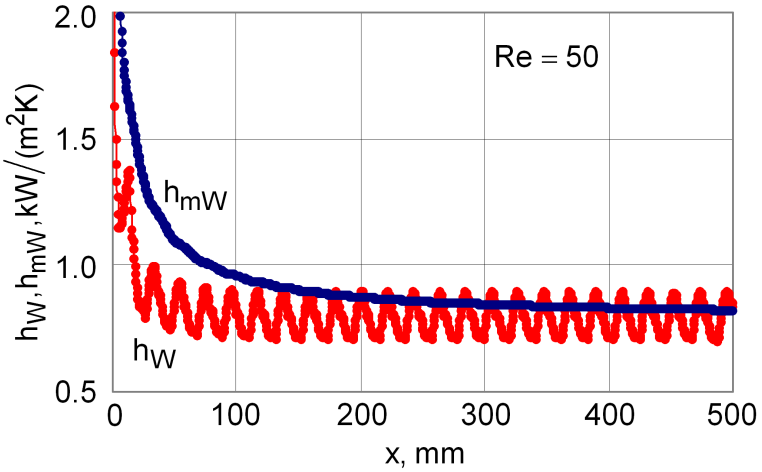

Figure 5.8: Heat transfer coefficients, $h_W = h_W(x)$ and $h_{mW} = h_{mW}(x)$, according to the Equation (4.33), with fully developed region in a 500mm long channel at $Re = 50$.

Further insights into the heat transfer fluctuations is provided by the local heat flux, $\dot{q}_W = \dot{q}_W(x)$, averaged over the width, s_T, of the strip according to Equation (4.31), the distribution of which is demonstrated in Figure 5.6 at different Reynolds numbers. When analysing these heat flux distributions, the heat flux fields shown in Figure 5.5 should be kept in mind. The quantity $\dot{q}_W(x)$ behaves damped oscillatory along the channel, decaying at the same time both in magnitude and amplitude. The positions of the maxima of $\dot{q}_W(x)$ nearly coincide (they are shifted in the upstream direction) with the axial positions of the welding spots, which was already observed in Figure 5.5. Averaging the heat flux $\dot{q}_W$ streamwise as stated in Equation (4.32), thus getting the quantity $\dot{q}_{mW} = \dot{q}_{mW}(x)$, results in a similar distribution with oscillations that are stronger damped.

The distributions of the local, spanwise over s_T averaged, heat transfer coefficient, $h_W(x)$, along the channel, and of the heat transfer coefficient, $h_{mW}(x)$, averaged over the current length, x, according to Equation (4.33), are illustrated in Figure 5.7. The curves representing $h_W(x)$ and $h_{mW}(x)$ are quite similar to those for the heat flux in Figure 5.6. The decrease of the heat transfer coefficients in the streamwise direction indicates that the channel length of $150mm$ is too short for the thermal developing region to become completed, even at the Reynolds number $Re = 50$, Figure 5.8. This heat transfer figure changes when the channel is sufficiently long and the fully developed heat transfer region is approached. Figure 5.7 illustrates this behaviour for the parameters noted in Figure 5.5.

The distributions of the local and average Nusselt number, $Nu_W(x)$ and $Nu_{mW}(x)$ defined in Equation 4.40 along the channel length are similar to the corresponding heat transfer coefficients, $h_W(x)$ and h_{mW}, respectively, and they are qualitatively comparable with the corresponding ones reported by Garg and Maji [14], Russ and Beer [53], Saniei and Dini [55] and Wang and Chen [69], Figures 2.11, 2.12 and 2.13, for two-dimensional channels.

5.1.3 Influence of the geometrical parameters

In the numerical experiments, three geometrical parameters (s_L, s_T and δ) have been varied, as well as the Reynolds number. The influence of varied geometrical parameters on the process quantities will be shown in the following sections separately. For this purpose, the geometrical parameter under consideration is varied together with the Reynolds number, whereas the remaining two geometrical parameters are kept constant.

5.1.3.1 Welding spot spacing in the flow direction

Effects of the longitudinal welding spots pitch, s_L, on the heat transfer coefficient for $500mm$ long channels at selected values of the Reynolds number and other geometrical parameters are visualised in Figure 5.9. As may be taken from the diagram, a larger

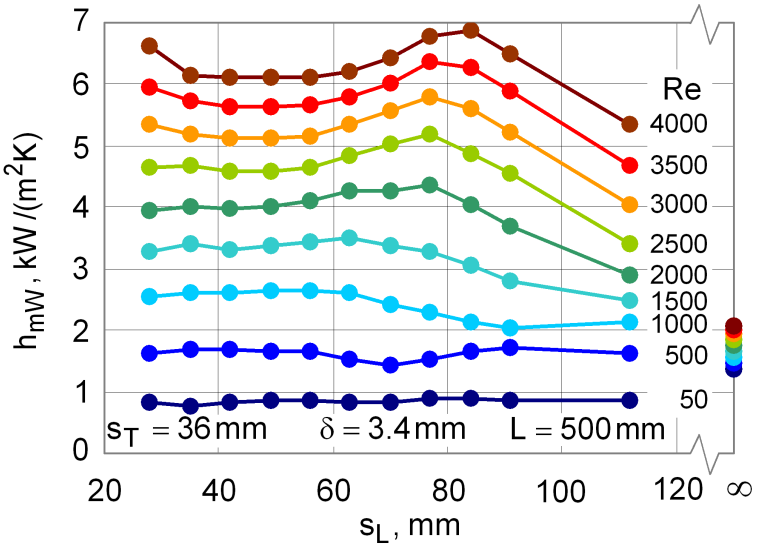

Figure 5.9: Average heat transfer coefficient, h_{mW} of 500 mm long channels at different Re as a function of longitudinal welding spots pitch, s_L; $s_L \to \infty$: parallel plates.

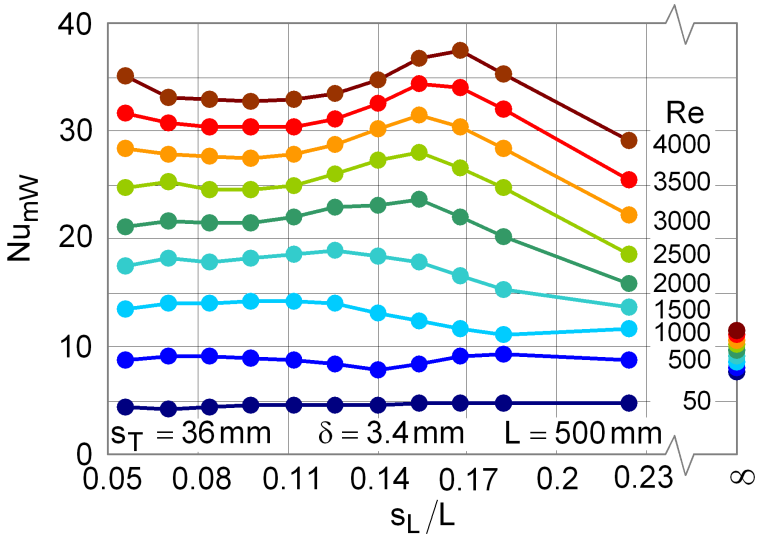

Figure 5.10: Average Nusselt number, Nu_{mW} of 500 mm long channels at different Re as a function of longitudinal welding spots pitch, s_L; $s_L/L \to \infty$: parallel plates.

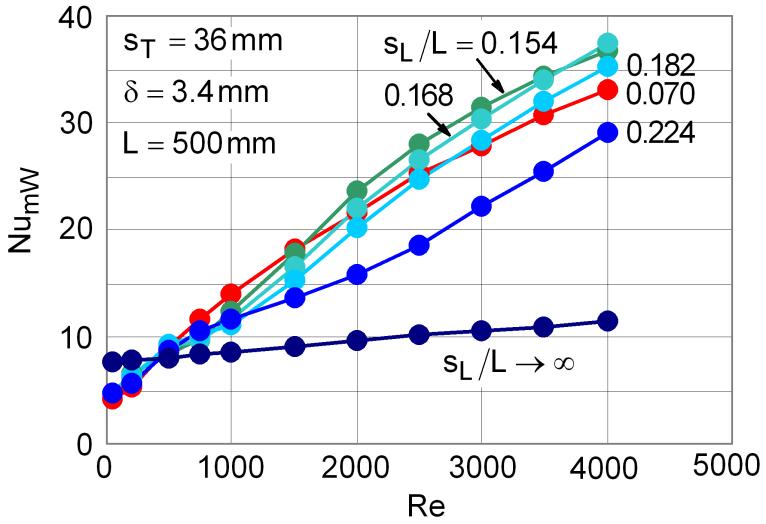

Figure 5.11: Average Nusselt number, Nu_{mW} of 500 mm long channels as a function of Re at different s_L/L; $s_L/L \to \infty$: parallel plates.

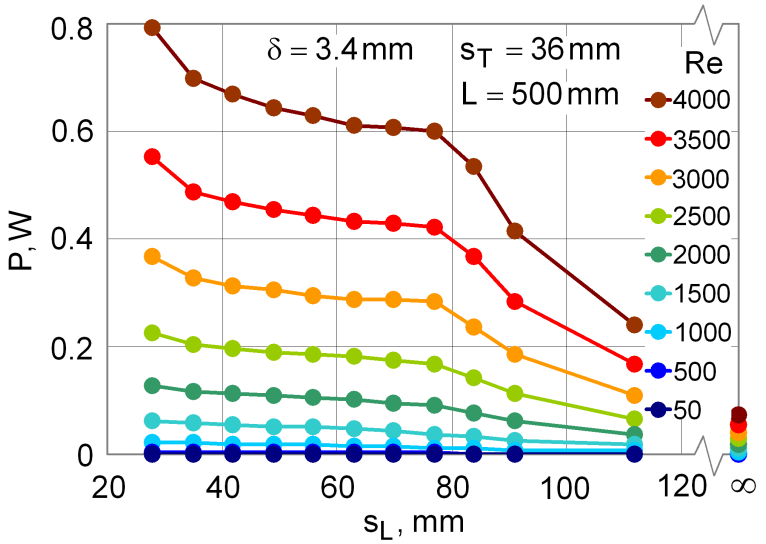

Figure 5.12: Pumping power, P, Equation (4.45), needed for forced convection through a 500 mm long channel as a function of the longitudinal welding spots pitch, s_L, at different Reynolds numbers, Re; $s_L \to \infty$: parallel plates.

Reynolds number corresponds to a larger heat transfer coefficient. At the smallest Reynolds number, $Re = 50$, the heat transfer is largely independent of s_L, whereas at other values of Re, certain dependency of h_{mW} on s_L is observed. At $s_L \to \infty$, h_{mW} tends to the value for the channel formed by plane parallel plates. These values are higher than the ones for the thermoplate at smaller Re. The situation reverses at larger Re, where the heat transfer of the thermoplate becomes better. Certain maxima of h_{mW} are observed at $s_L \approx 80$ mm at larger Reynolds numbers.

The Nusselt number, Nu_{mW} depends on the longitudinal welding spots pitch, s_L, in the same way as the heat transfer coefficient h_{mW}, since the hydraulic diameter and the kinematic viscosity remain constant when the longitudinal welding spots pitch s_L is varied, Figure 5.10.

Figure 5.11 shows the effect of the Reynolds number, Re, on the heat transfer for selected values of the geometrical parameters. The average Nusselt number Nu_{mW} of the thermoplate is larger than of the flat channel for $Re \geq 500$. At $Re \leq 500$ the secondary flows are obviously too weak to outweigh the deterioration effect of recirculation zones on the heat transfer, thus leading to lower Nu_{mW}-values in comparison to those of the flat channel.

The pumping power, P, calculated according to Equation (4.45), as a function of the longitudinal welding spot pitch, s_L, at different Reynolds numbers is visualised in Figure 5.12. The pressure drop increases with increasing Reynolds number, resulting in higher pumping power, needed for the forced convection through the channel. The pumping power is a decreasing function of the welding spot spacing s_L, at all Reynolds numbers, having its minimum when $s_L \to \infty$, which is the parallel plate channel.

5.1.3.2 Welding spot spacing in the cross direction

The distribution of the average heat transfer coefficient, h_{mW}, as a function of transversal welding spots pitch, s_T, at different Reynolds numbers for 500 mm long channels is shown in Figure 5.13. A larger Reynolds number corresponds to a larger heat transfer coefficient, as it was the case when the longitudinal welding spots pitch was varied. At all Reynolds numbers, Re, the heat transfer coefficient, h_{mW}, behaves as a decreasing function of the transversal welding spot pitch, s_T. However, at a lower Reynolds numbers, $Re \leq 500$, this dependency is hardly recognisable.

Since the the hydraulic diameter and the thermal conductivity remain constant also when the transversal welding spots pitch is varied, the dependency of the average Nusselt number, Nu_{mW}, on the spacing s_T is very similar to the distribution of the average heat transfer coefficient, h_{mW}, Figure 5.14.

The same distribution of the average Nusselt number, Nu_{mW}, as the one shown in Figure 5.14 is visualised in Figure 5.15 as a function of the Reynolds number, Re, s_L/L being a parameter.

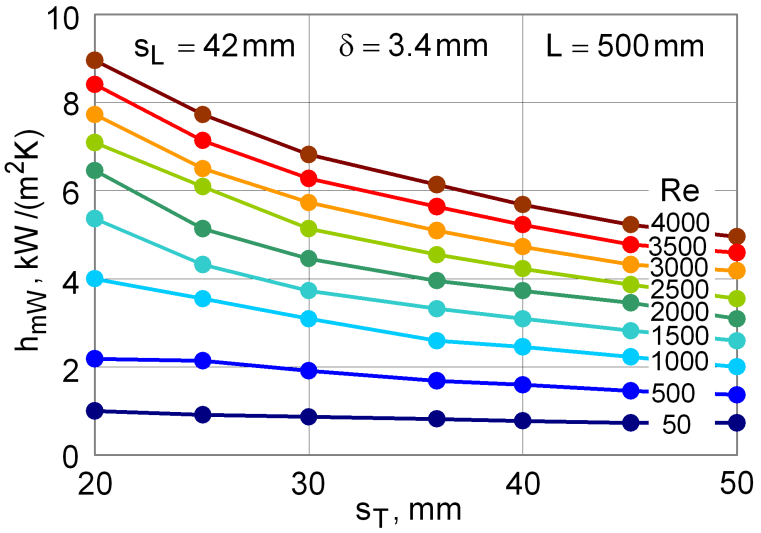

Figure 5.13: Average heat transfer coefficient, h_{mW} of 500 mm long channels at different Re as a function of transversal welding spots pitch, s_T.

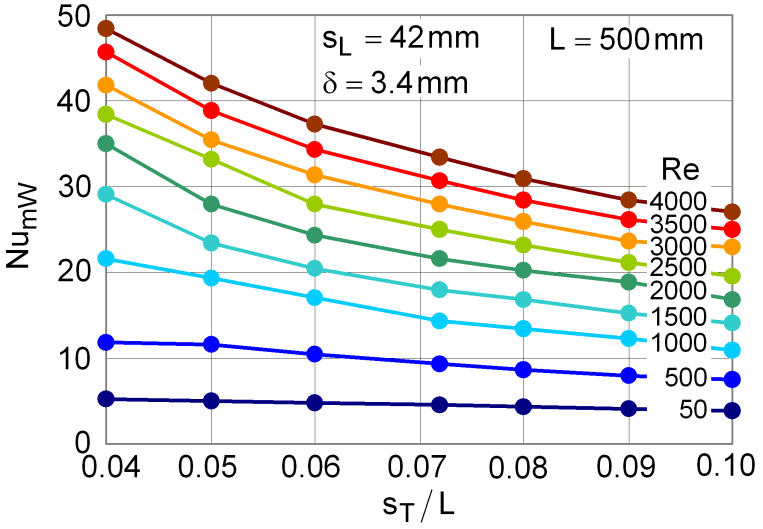

Figure 5.14: Average Nusselt number, Nu_{mW} of 500 mm long channels at different Re as a function of transversal welding spots pitch, s_T.

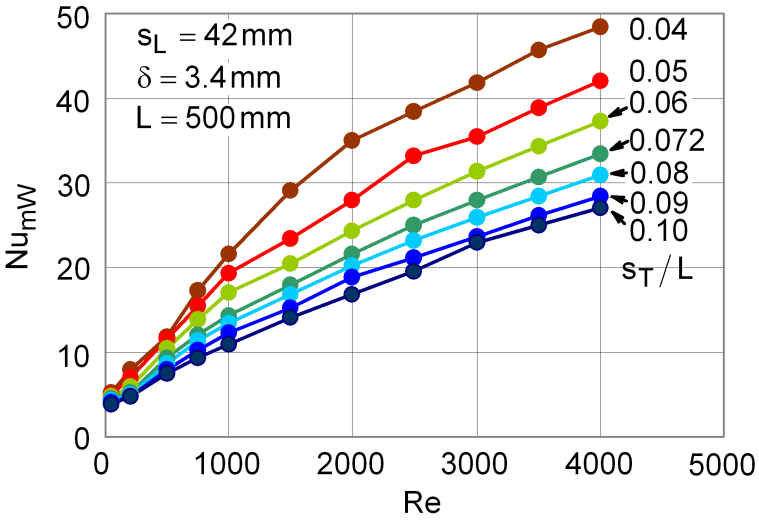

Figure 5.15: Average Nusselt number, Nu_{mW} of 500 mm long channels as a function of Re at different s_T/L.

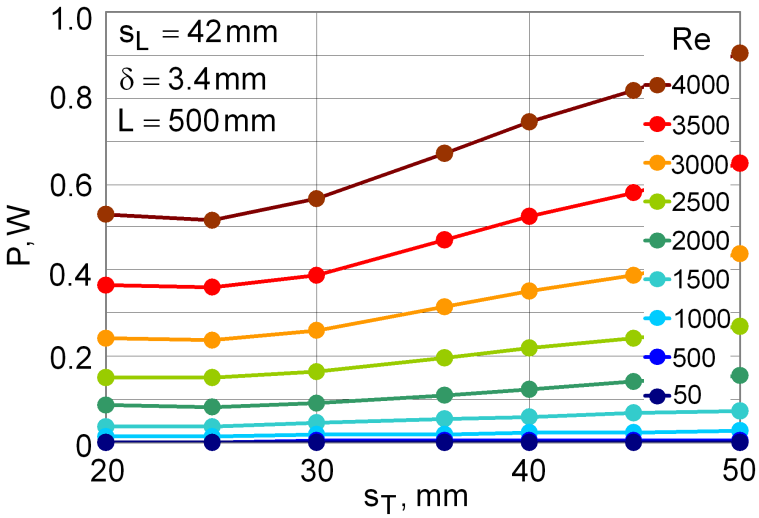

Figure 5.16: Pumping power, P, Equation (4.45), needed for forced convection through a 500 mm long channel as a function of the transversal welding spots pitch, s_T, at different Reynolds numbers, Re.

Figure 5.16 visualises the dependency of the pumping power on the transversal welding spots pitch, s_T, calculated according to Equation (4.45). At lower Reynolds numbers, $Re \leq 1000$, the pumping power increases with increasing s_T, but at larger Reynolds numbers, it is first slightly decreasing, reaching a minimum, and than increasing. In this context it is to be noted, that the pumping power is not only affected by the pressure drop when the parameter s_T is varied, as it was the case when the longitudinal welding spot spacing, s_L, was varied. Increasing the parameter s_T, the inlet cross-section area of the channel is increasing as well, which indirectly increases the volume flow rate, when the Reynolds number is kept constant. In Figure 5.16 the influence of both, pressure drop and volume flow rate is contained.

5.1.3.3 Maximal plate distance

The average heat transfer coefficient, h_{mW}, as a function of the maximal plate distance, δ, is illustrated in Figure 5.17. The heat transfer coefficient is a decreasing function of δ, which is rooted in a corresponding reduction of the fluid velocity at the given Reynolds number.

The corresponding average Nusselt number, Nu_{mW}, as a function of the ratio δ/L is shown in Figure 5.18. It is almost a linearly increasing function, but at the Reynolds number $Re = 50$ the increase is hardly observable.

At first sight, the increase of Nu_{mW} with increasing δ/L, Figure 5.18, could appear contradictory, when comparing it with the distribution of the heat transfer coefficient, Figure 5.17. The discrepancy between the heat transfer coefficient and Nusselt number is associated with the increase of the hydraulic diameter, d_h. The Nusselt number calculated according to Equation (4.40) depends not only on the heat transfer coefficient, but also on the hydraulic diameter, d_h, which directly increases by rising the plate distance δ.

The average Nusselt number, Nu_{mW}, as a function of the Reynolds number, Re, the ratio δ/L being a parameter, is illustrated in Figure 5.19.

Similar to the case, where the transversal welding spot pitch, s_T, was varied, one would expect that not only the pressure drop changes, when the the plate distance, δ, is changed, but also the volume flow rate. However, the volume flow rate remains unchanged when the plate distance, δ, i.e. the hydraulic diameter, d_h, is varied, at a constant Reynolds number. An increase of δ, i.e. d_h, causes a decrease of the average axial velocity, $\bar{u}$, which means, that the pumping power is in this case influenced only by the pressure drop, as it was the case, when the parameter s_L was varied. Figure 5.20 provides an information about the dependency of the pumping power, P, on the maximal plate distance, δ. It decreases rapidly with increasing plate distance, which is connected with the velocity and pressure drop reduction.

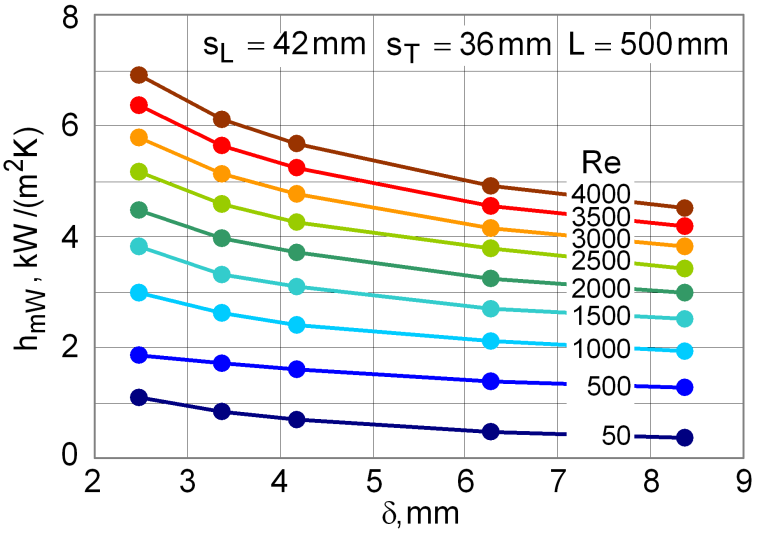

Figure 5.17: Average heat transfer coefficient, h_{mW} of 500 mm long channels at different Re as a function of maximal plate distance, δ.

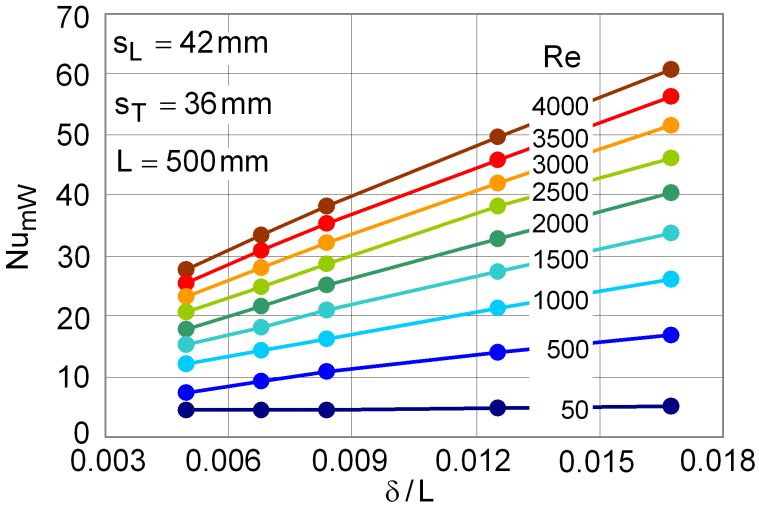

Figure 5.18: Average Nusselt number, Nu_{mW} of 500 mm long channels at different Re as a function of maximal plate distance, δ.

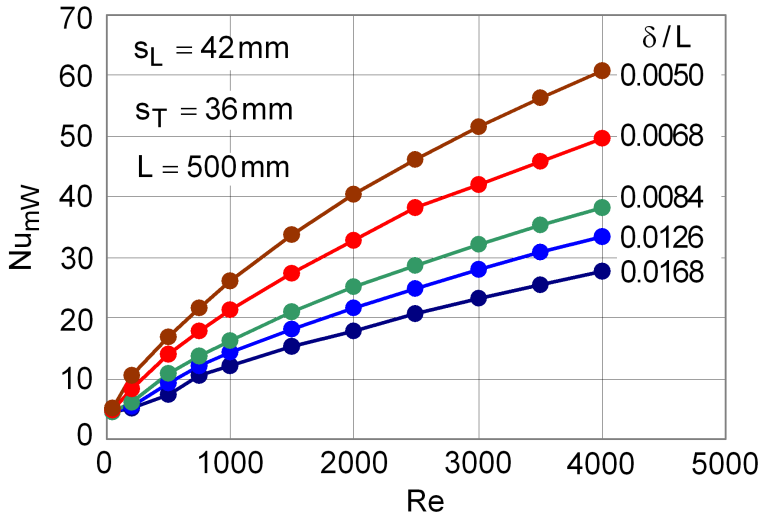

Figure 5.19: Average Nusselt number, Nu_{mW} of 500 mm long channels as a function of Re at different δ/L.

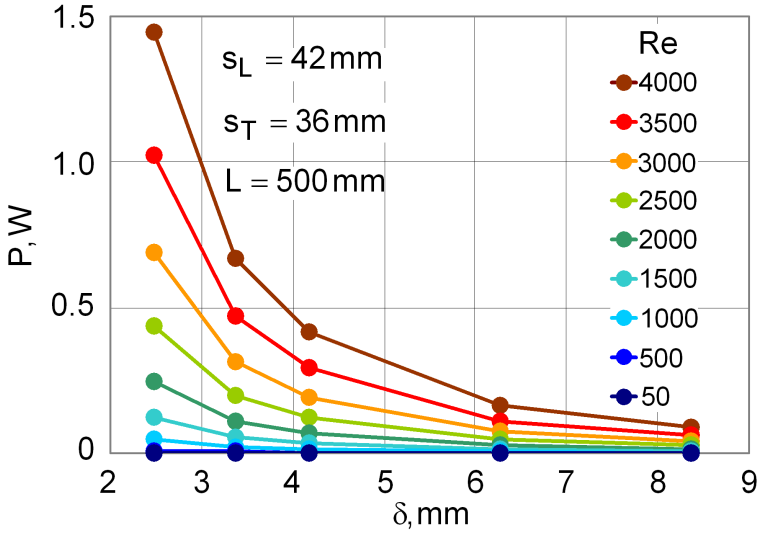

Figure 5.20: Pumping power, P, Equation (4.45), needed for forced convection through a 500 mm long channel as a function of maximal plate distance, δ, at different Reynolds numbers, Re.

5.1.3.4 Nusselt number correlation

The Nusselt number of the thermoplate is shown by the numerical experiments to depend on the Reynolds number and the dimensionless geometrical parameters δ/L, s_T/L and s_L/L.

Assuming a function of the form

$$Nu_{mW} = C_1 \left(\frac{s_L}{L}\right)^{n_1} \left(\frac{s_T}{L}\right)^{n_2} \left(\frac{\delta}{L}\right)^{n_3} Re^{n_4} Pr^{n_5}, \tag{5.1}$$

numerical results for the Nusselt number can be correlated in certain ranges of the geometrical parameters. Since the Prandtl number was kept constant in this study ($Pr = 5.97$), Equation 5.1 becomes

$$Nu_{mW} = C_2 \left(\frac{s_L}{L}\right)^{n_1} \left(\frac{s_T}{L}\right)^{n_2} \left(\frac{\delta}{L}\right)^{n_3} Re^{n_4}, \tag{5.2}$$

where the constant C_2 takes into account the influence of the Prandtl number, $C_2 = C_1 Pr^{n_5}$. The constants are to be calculated using the least square method, which is implemented in some mathematical softwares, such as Mathematica or Matlab.

Using the Equation (5.2) with the constants given in the Table 5.1, the average Nusselt numbers of the models that dimensions are defined in Table 4.1 can be correlated with the tolerance of $\pm 10\%$ for $Re \geq 500$ and $s_L \leq 63$.

Keeping the same form of the correlation equation as above, Equation (5.2), and using the constants given in Table 5.2, the average Nusselt numbers of all the simulated models, Table 4.2, can be approximated with the discrepancy of $\pm 20\%$.

Table 5.1: Constants used in Equation (5.2).

C_2	n_1	n_2	n_3	n_4
0.843	−0.03	−0.68	0.66	0.62

Table 5.2: Constants used in Equation (5.2).

C_2	n_1	n_2	n_3	n_4
0.843	−0.249	−0.322	0.66	0.607

However, in order to achieve a better accuracy in all ranges of varied parameters with, a complicated function for calculating the average Nusselt number, Nu_{mW}, for

example a five-dimensional polynomial

$$Nu_{mW} = \sum_{i=0}^{i=I} \sum_{j=0}^{j=J} \sum_{k=0}^{k=K} \sum_{l=0}^{l=L} \sum_{m=0}^{m=M} c_{i,j,k,l,m} \left(\frac{\delta}{L}\right)^i \left(\frac{s_T}{L}\right)^j \left(\frac{s_L}{L}\right)^k Re^l Pr^m, \tag{5.3}$$

would be necessary, where I, J, K, L and M represent the polynomial degree for coordinates δ/L, s_T/L,s_L/L, Re and Pr, respectively and $c_{i,j,k,l,m}$ are constants, that are also in this case to be calculated through the least squares method, based on the simulation results for the average Nusselt numbers, given in Appendix F, Table F.1.

All the numerical results for the Nusselt number can be approximated using Equation (5.3) with a deviation of $\leq 10\%$ by setting $I = J = K = L = 2$, $M = 0$ and $m = 0$, which results in 81 constants, that are to be calculated, Appendix E, Table E. This would be, however, scarcely applicable in the engineering practice.

5.1.3.5 The thermo-fluid characteristic

The complex geometry of the thermoplate channel results in a larger heat transfer coefficient in comparison to the channel with plane walls. This heat transfer improvement is to be paid by a larger pressure drop, that is to say, by a larger pumping power at given volume flow rate. To illustrate this interplay, one combines the heat flow rate, $\dot{Q}_W$, and the pumping power, P, to a thermo-fluid characteristic of the heat transfer device, see e.g. Stephan and Mitrović [62], and Webb and Kimm [71]. For instance, the ratio $\dot{Q}_W/P$ specifies the running costs of the heat transfer.

As an example, Figure 5.21 illustrates the quantity $\dot{Q}_W/P$ in dependence on the plate geometry with Re as parameter. As is obvious from this Figure, the ration $\dot{Q}_W/P$ increases with increasing s_L/L, and the curves move up with rising Reynolds number. However, at each Re, this ratio is larger for the channel having plane walls ($s_L/L \to \infty$). This behaviour is emphasized in Figure 5.22 that shows the ratio of the thermo-fluid characteristics $(\dot{Q}_W/P)_{TP}$ and $(\dot{Q}_W/P)_{FC}$ of the thermoplate and of the flat channel with plane walls as function of the geometrical parameters for selected Reynolds numbers, Re. The ratio is seen to increase with increasing s_L/L, but it still remains smaller than unity, the curve for $Re = 50$ at larger s_L/L being an exception.

In general, at larger Reynolds numbers the thermoplate is more effective than at smaller ones. Furthermore, the ratio $(\dot{Q}_W/P)_{TP}/(\dot{Q}_W/P)_{FC}$ is smaller at smaller s_L/L and larger δ/L. Its dependency on s_T/L is more complicated because of the maxima at larger Reynolds numbers.

Summarising the results on thermo-fluid characteristics, one may conclude that the flat channel formed by plane walls shows a better heat transfer characteristic, expressed in terms of pumping power, than the corresponding thermoplate. However, a fabrication of such a channel without welding spots seems scarcely possible in sizes required in common practice and, from this point of view, the parallel plate channel serves merely as a model for comparison purposes.

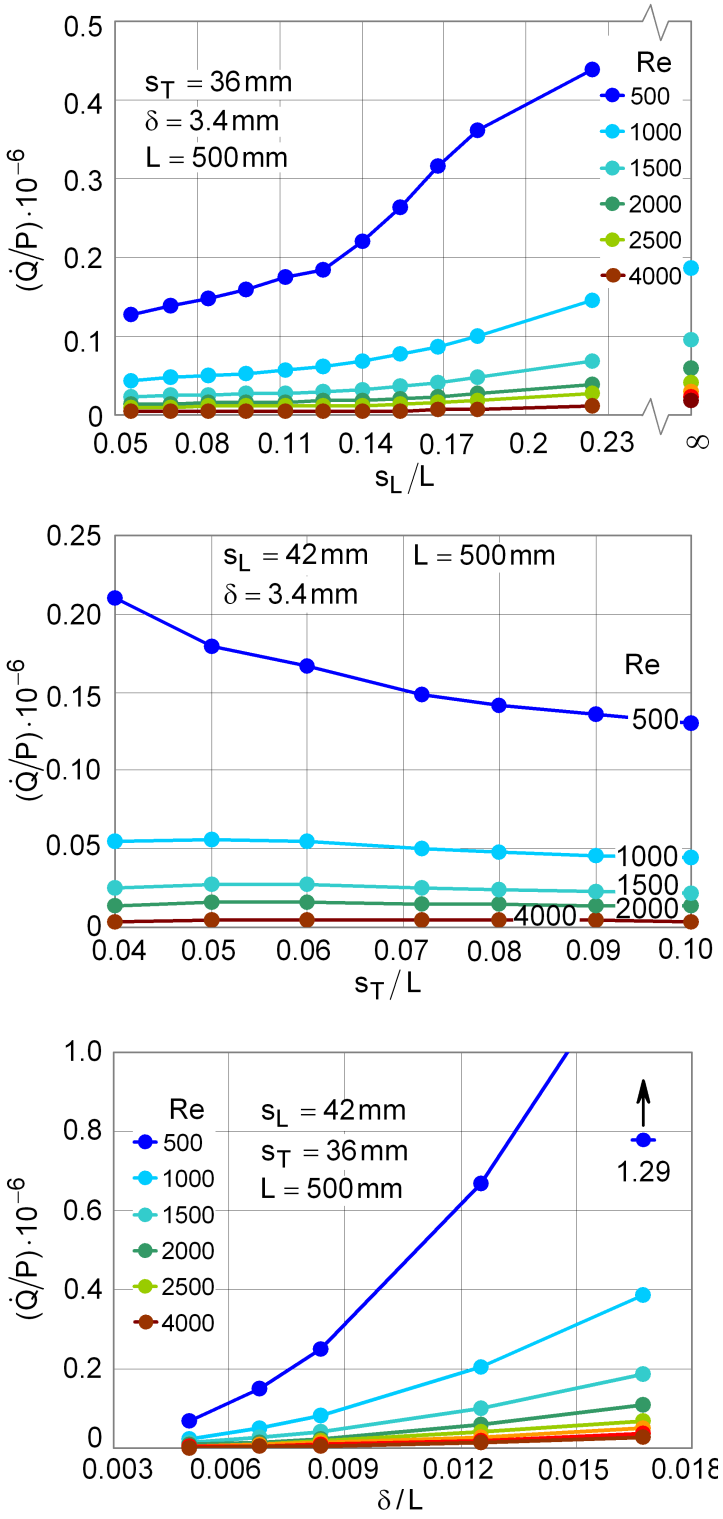

Figure 5.21: Thermo-fluid characteristic of a 500 mm long thermoplate channel as function of geometry at selected Reynolds numbers; $s_L/L \to \infty$: parallel plates .

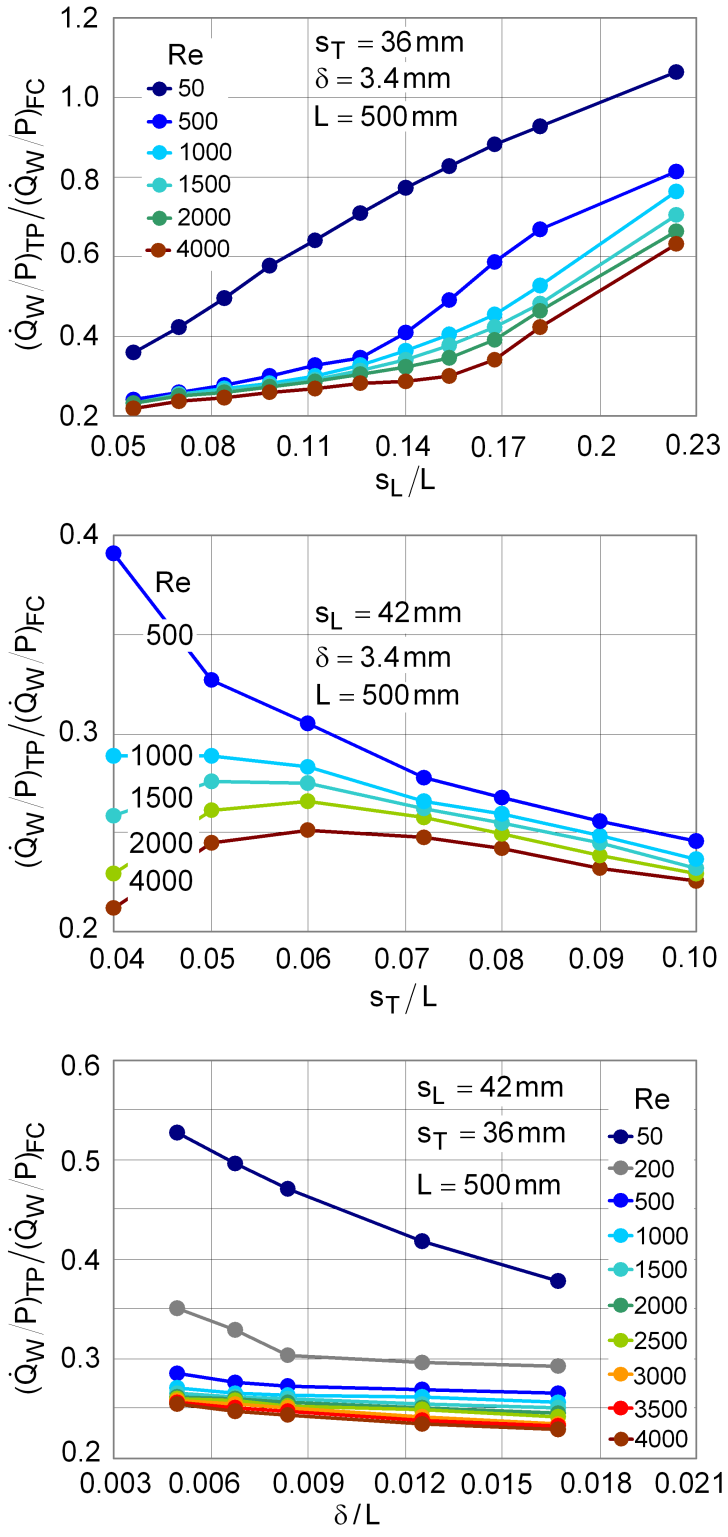

Figure 5.22: Thermo-fluid characteristic of the thermoplate compared with the characteristic of the flat channel at selected Reynolds numbers.

5.1.4 Welding spots pattern and thermoplate surface shape

The thermoplates with welding spots arranged in a staggered manner, whose surface is described by employing of the trigonometrical functions, Equation (4.1), Figure 4.1a, were analysed and described in previous chapters. However, thermoplates with different welding spots arrangements and surface shapes have not been compared yet.

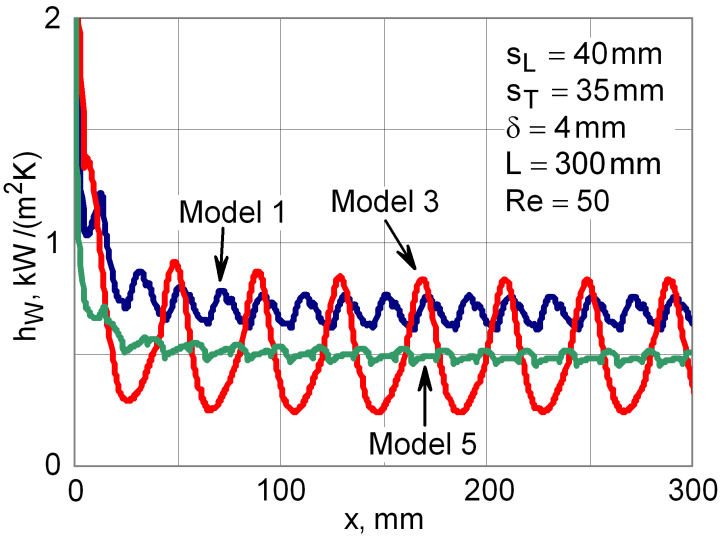

Figure 5.23: Distribution of the local heat transfer coefficient, Equation (4.33), for different models, Figure 4.1a, c and e, at $Re = 50$.

Table 5.3: Volume flow rate comparison for different models, Figure 4.1.

Model	Re									
	50		100		500		1000		2000	
	u_{IN} $[\frac{m}{s}]$	$\dot{V}$ $[\frac{mm^3}{s}]$	u_{IN} $[\frac{m}{s}]$	$\dot{V}$ $[\frac{mm^3}{s}]$	u_{IN} $[\frac{m}{s}]$	$\dot{V}$ $[\frac{mm^3}{s}]$	u_{IN} $[\frac{m}{s}]$	$\dot{V}$ $[\frac{mm^3}{s}]$	u_{IN} $[\frac{m}{s}]$	$\dot{V}$ $[\frac{mm^3}{s}]$
1	0.011	781	0.022	1557	0.112	7786	0.224	15572	0.448	31144
2	0.011	1173	0.022	2346	0.112	11728	0.223	23456	0.447	46911
3	0.011	782	0.022	1563	0.112	7817	0.223	15634	0.447	31269
4	0.011	376	0.022	753	0.112	3764	0.224	7529	0.447	15057
5	0.006	706	0.012	1412	0.062	7060	0.124	14121	0.247	28242

Figures 5.23 and 5.24 show the local heat transfer coefficient, calculated according to Equation (4.33) for models 1, 3 and 5, Figure 4.1a, c and e. These three models are compared, because not only the overall geometrical parameters such as s_L, s_T, δ

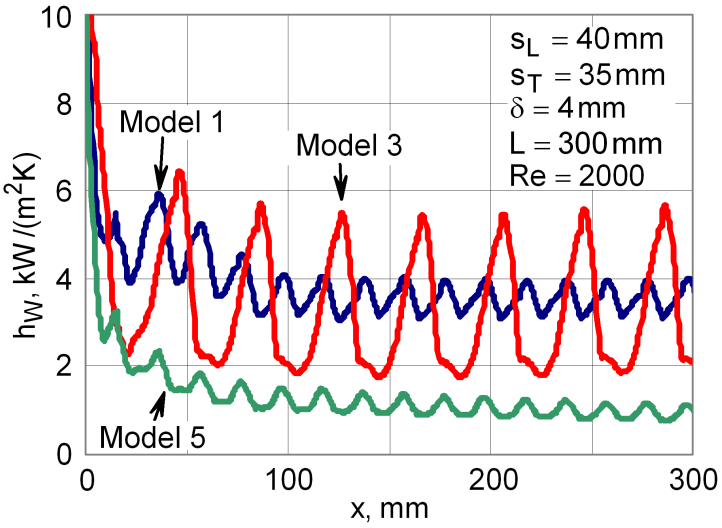

Figure 5.24: Distribution of the local heat transfer coefficient, Equation (4.33), for different models, Figure 4.1a, c and e, at $Re = 2000$.

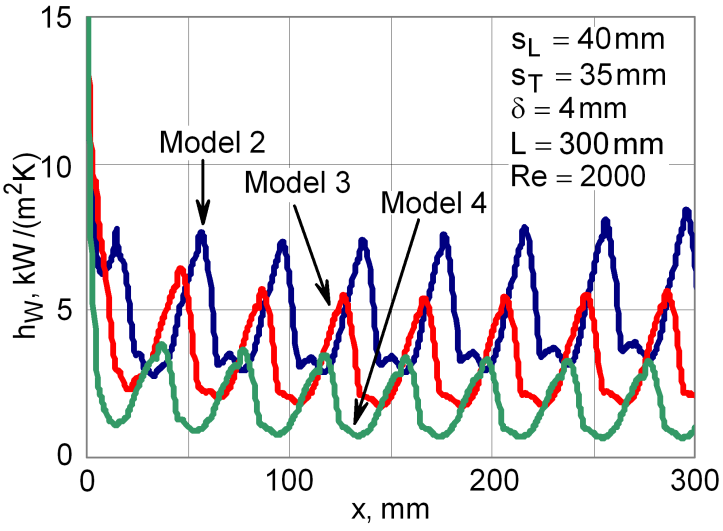

Figure 5.25: Distribution of the local heat transfer coefficient, Equation (4.33), for different models, Figure 4.1b, c and e, at $Re = 2000$.

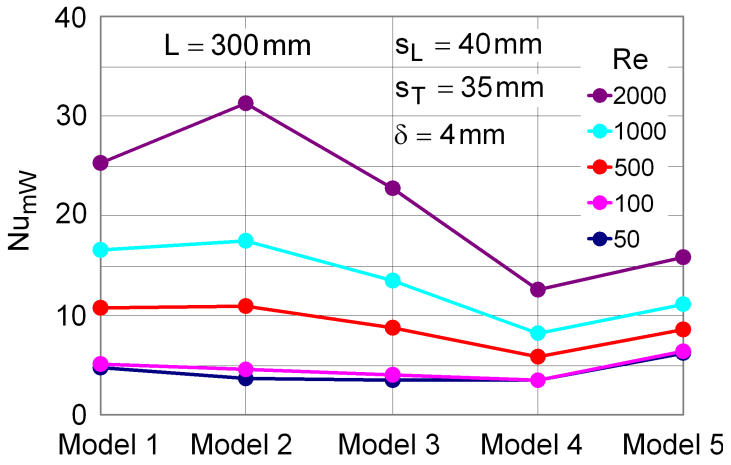

Figure 5.26: Average Nusselt number at different Reynolds numbers for different models, Figure 4.1.

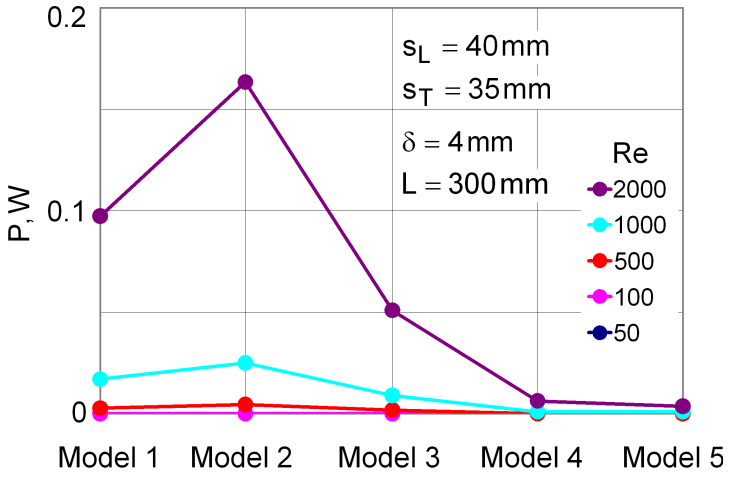

Figure 5.27: Pumping power number at different Reynolds numbers for different models, Figure 4.1.

and L, as well as the Reynolds numbers are the same, but also the volume flow rate differs not significantly, Table 5.3. The channel with staggered welding spots (model 1, Figure 4.1a) seems to be the most effective one, whereas the channel with surface approximated using the exponential function (4.4), model 5 in Figure 4.1e, gives the lowest value for the heat transfer coefficient. The local heat transfer coefficient of the channel with parallel welding spots, model 3 in Figure 4.1c, has the largest oscillation amplitude, but its average value lies in between the other two, Maletić and Mitrović [31].

The models 2, 3 and 4 have basically the same geometry. They are only shifted in

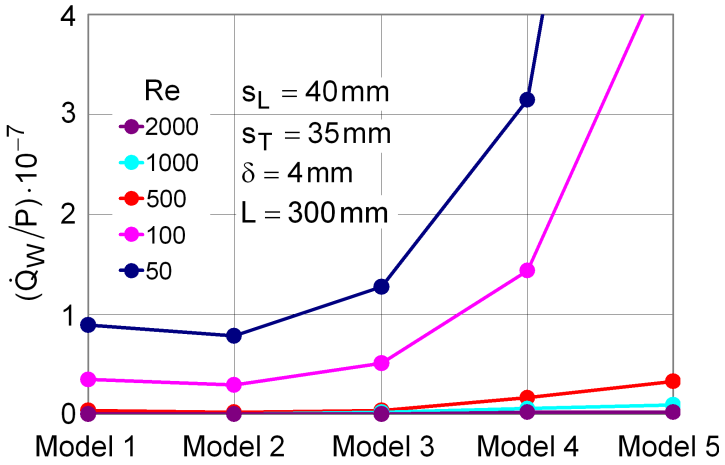

Figure 5.28: Thermo-fluid characteristic at different Reynolds numbers for different models, Figure 4.1.

x direction and have different inlet flow areas when other geometrical parameters (s_L, s_T, δ, d_h and L) are kept constant. For this reason, the volume flow rates for models 2, 3 and 4 are different at the same Reynolds number, Table 5.3, which causes differences in heat transfer coefficient, Figure 5.25.

The average Nusselt number, Equation (4.40), and pumping power, Equation (4.45), for all five simulated models (Figure 4.1) at different Reynolds numbers are given in Figures 5.26 and 5.27, respectively. From Figures 5.26 and 5.27 it can be seen, that the heat transfer enhancement has to be paid by higher pumping power.

Combining the heat transfer rate and pumping power into a thermo-fluid characteristic, as it was done in the previous section, one can get some insights into the running costs of the heat transfer in different models, Figure 5.28. Although the channel, whose heat transfer surface is approximated by Equation (4.4) does not show the best heat transfer characteristic in comparison to other models, the pressure drop in such a channel is much lower than in other channels. For that reason, the model 5, Figure 4.1e, seems to be the most effective one.

At this place it has to be noted, that the thermo-fluid characteristic defined as $\dot{Q}/P$ could be misleading, when considered alone without the heat transfer rate $\dot{Q}$ and pumping power P. Although the heat transfer rate $\dot{Q}$ and pumping power P have the same unit, the prices of these two arts of energy are often quite different and other costs, like storage costs, were not taken into account in this analysis.

5.2 Symmetric heated channels, transient flows

Models with unsteady fluid flow and heat transfer are considered in this section, as it was stated in Table 4.4. Since the simulations of the time dependent flows are rather time consuming, only three numerical experiments with the same thermoplate geometry, but different definitions of the fluid velocity at the inlet were made.

To satisfy the condition that the Courant number is always smaller than unity,

$$C_r = \frac{\bar{u}\Delta t}{\Delta l} \leq 1, \tag{5.4}$$

which is required in numerical calculations of time dependent flows, the average inlet velocity was chosen to be $\bar{u}_{IN} = 0.1\text{m/s}$, the time step size $\Delta t = 0.001$ s, which corresponds to the Reynolds number $Re = 450$ and one thousand time steps for the duration of the simulation of 1 s. Δl denotes the local cell size.

Development of the velocity field in the symmetry plane, $y = 0$, with time at different time steps, 0 s $< t <$ 1 s is visualised in Figure 5.29. At the very beginning of the time interval, $t = 0.05$ s, one can notice the fluid separation behind of each welding spot. There arise vortices, the centres of which move downstream with the time, until the recirculation zones occupy whole regions between two neighbouring welding spots. Tis happens already at $t = 0.4$ s and from this time step the fluid flow can be considered as hydraulically fully stabilised, i.e. developed with the time.

The situation is much different, if the development of the temperature field in the symmetry plane, $y = 0$ with the time is considered, Figure 5.30. Large portion of fluid remains thermally unaffected until $t = 0.2$ s, with small regions behind the welding spots being exceptions. This was expected, since the channel height and fluid velocity the in these regions are low. The temperature field develops further, also after $t = 0.4$ s, although the fluid flow was stabilised until this time step. Much the same conclusion can be deduced after analysing of the heat flux time development at the thermoplate surface, which is illustrated in Figure 5.31. The heat flux maximum is placed at the inlet, $x \approx 0$, because of the very high temperature gradient. Apart from this one, the local heat flux maxima are placed in the central section of the thermoplate,$z \approx s_T/2$, i.e. between the two rows of the welding spots, where the fluid velocity is high, and immediate before every welding spot, where the channel height converges and cold fluid flows with high velocity, resulting in higher temperature gradients.

A comparison between the average heat transfer coefficients for steady and unsteady flows is given in Figure 5.32. It can be seen that the average heat transfer coefficient for the unsteady flow tends asymptotic toward the one of steady state flow. However, the period of 2 s is not enough for the fluid flow to be completely stabilised from the thermal point of view.

Figure 5.33 illustrates the time evolution of the local heat transfer coefficient. At the beginning of the time interval, it has high values with very short developing region.

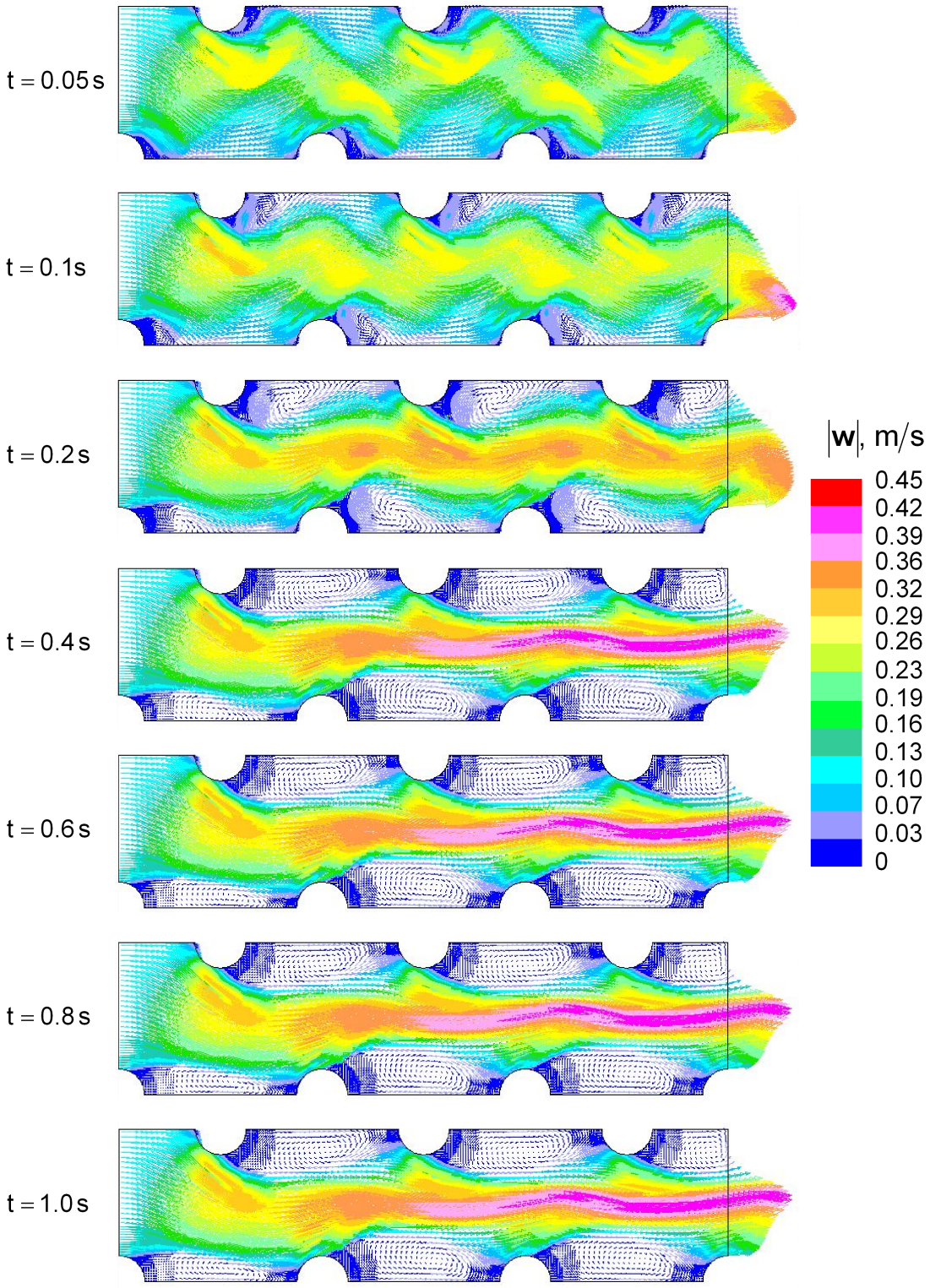

Figure 5.29: Development of the velocity field in the symmetry plane $y = 0$ with time.

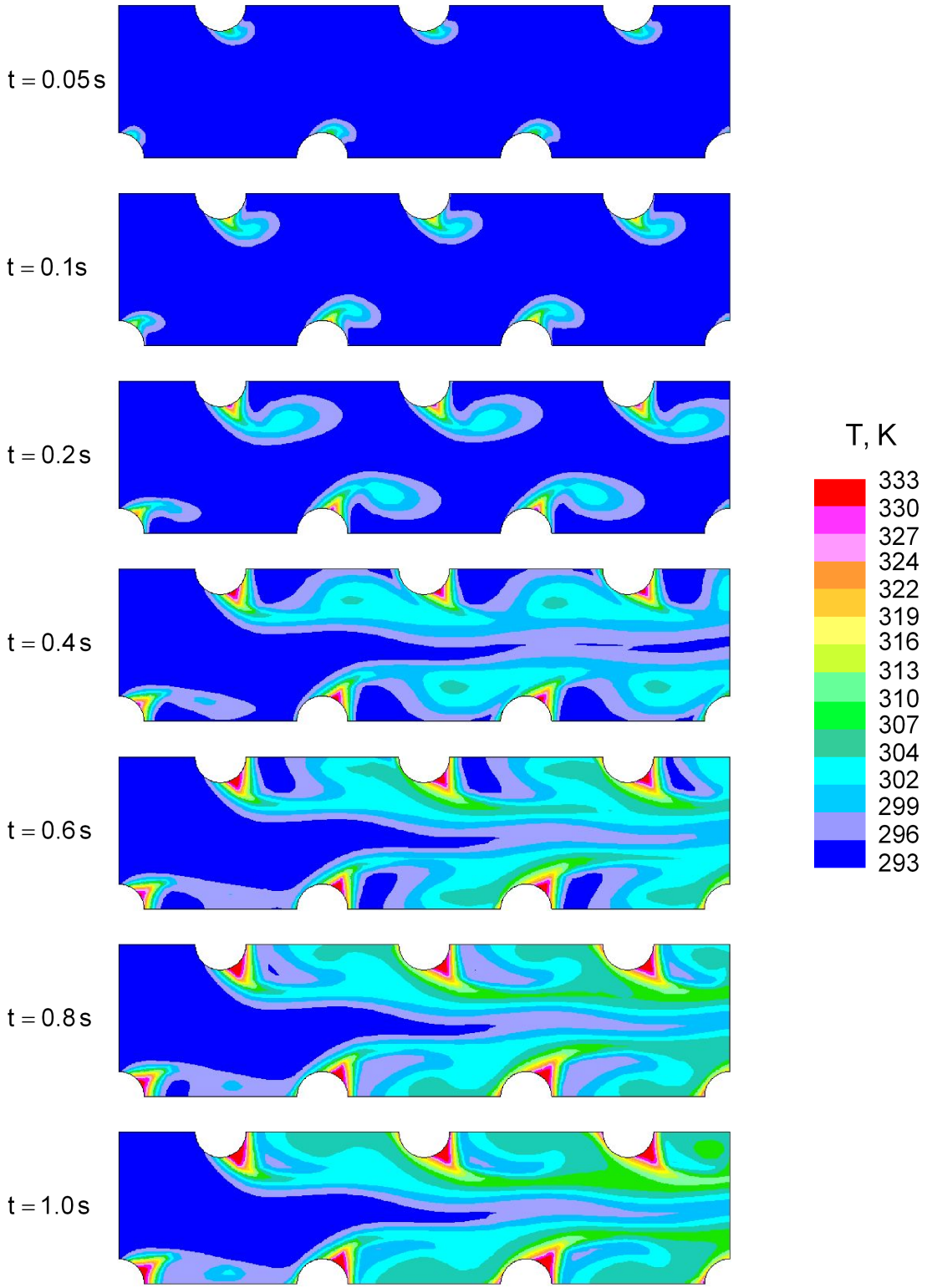

Figure 5.30: Development of the temperature field in the symmetry plane $y = 0$ with time.

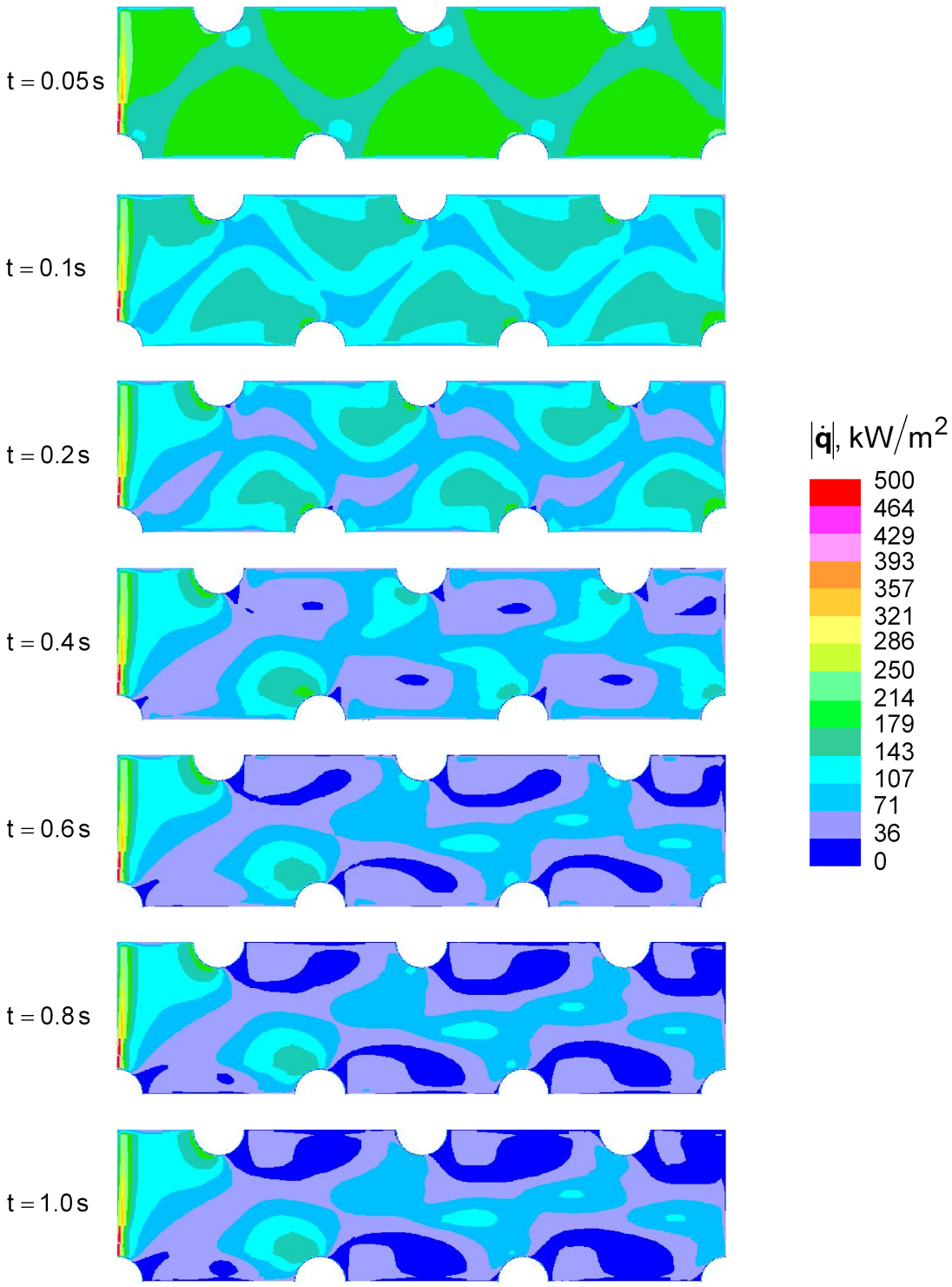

Figure 5.31: Development of the heat flux at the thermoplate wall with time.

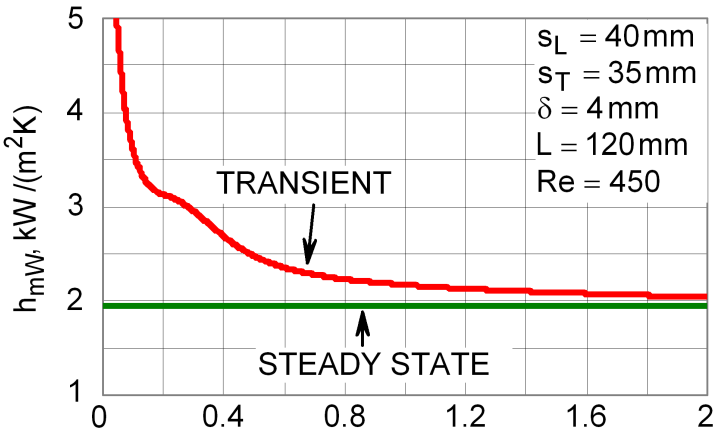

Figure 5.32: Heat transfer coefficient averaged in space for a 120 mm long model, steady and unsteady flow.

As the time passes, the developing region grows and the heat transfer coefficient values fall down with a tendency to reach the corresponding distribution of the steady state flow.

Although the boundary layer theory is only conditionally adequate to study the fluid flow and heat transfer in closed channels, under simplified conditions it can give some insights into the difference in time periods needed for the fluid flow to be stabilised hydraulically and thermally. Considering transient boundary layer along a flat plate, i.e. Blasius and Rayleigh problems, see e.g. Schlichting and Gersten [58], the velocity and temperature boundary layer thickness are described as

$$\delta_w = c_1\sqrt{\nu t}, \tag{5.5}$$

$$\delta_T = c_2\sqrt{\kappa t}, \tag{5.6}$$

where ν, κ and t denote kinematic viscosity, thermal diffusivity ant time, respectively, c_1 and c_2 are constants.

This means that the velocity and temperature boundary layers do not grow with the same velocity. If the fluid flow between two parallel flat plates is considered, the velocity and temperature boundary layers will appear at both plates. The velocity boundary layers will meet in the middle of such channel at time t_1, and the temperature layers at time t_2. Adopting $c_1 \approx c_2$, these two time periods, t_1 and t_2, will be related by the Prandtl number:

$$t_2 = \frac{c_1^2}{c_2^2}\frac{\nu}{\kappa}t_1 \approx Pr \cdot t_1. \tag{5.7}$$

Since the Prandtl number for liquids is $Pr > 1$, the temperature boundary layers obviously have to meet after the velocity boundary layers met, $t_2 > t_1$. This means, that the

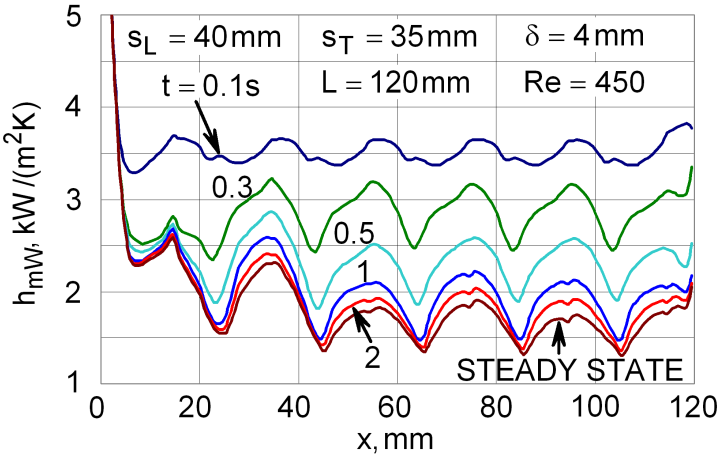

Figure 5.33: Local heat transfer coefficient for a 120 mm long model, at different time steps.

fluid flow will stabilise hydrodynamically first, and then thermally, which was observed in the numerical experiments in this section.

Analysis of unsteady boundary layer over a wavy plate gives qualitative similar results, see Saha and Debnath [54].

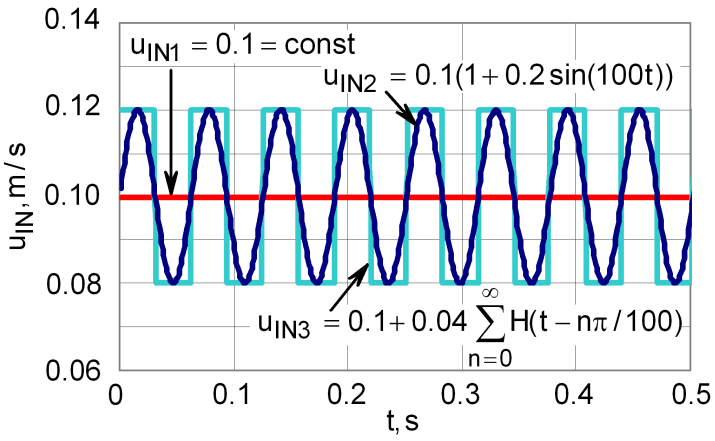

Figure 5.34: Different inlet fluid velocities.

As a further example of transient fluid flow, the fluid velocity at the inlet was varied

from a constant value with time to oscillating functions, as it was stated in Table 4.4:

$$u_{IN1} = 0.1 \quad [\mathrm{m/s}], \tag{5.8}$$

$$u_{IN2} = 0.1\,(1 + 0.2\,(sin(100t))) \quad [\mathrm{m/s}], \tag{5.9}$$

$$u_{IN3} = 0.1 + 0.04 \sum_{n=0}^{\infty} H(t - \frac{n\pi}{100}) \quad [\mathrm{m/s}], \tag{5.10}$$

where $H(t)$ represents the Heaviside step function. These three velocity distributions are visualised in Figure 5.34.

As a result, the heat transfer coefficient averaged in space, but not in time, h_{mW}, was compared and this comparison is illustrated in Figure 5.35. The curves representing the heat transfer distributions with oscillating fluid velocities at the inlet also oscillate around the one with constant velocity. Since the difference in heat transfer coefficients for transient flows averaged with time is smaller than 0.3%, it can be said, that the fluctuations of the inlet fluid velocity defined by Equations (5.9) and (5.10), where the frequency and amplitude of the velocity oscillations were kept constant, do not affect the heat transfer performance of the thermoplate.

5.3 Asymmetric heated channels

In Chapter 3 it was explained in detail how the asymmetrical boundary conditions influence the heat transfer and the Nusselt number distribution in a parallel plate channel. For that simple channel geometry the energy equation in the dimensionless form (3.12)

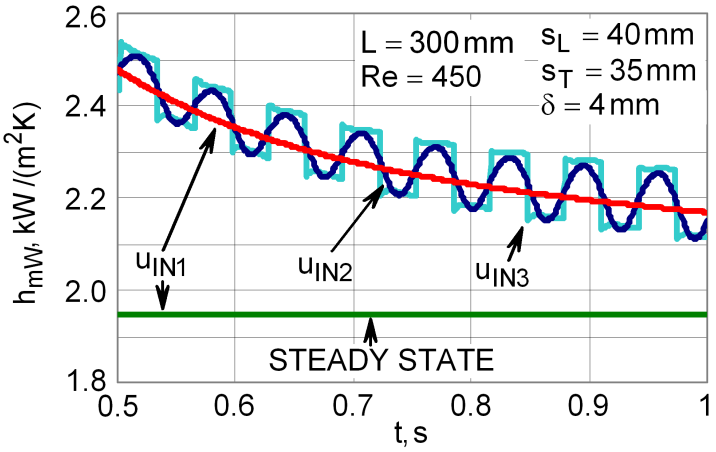

Figure 5.35: Average heat transfer coefficient (averaged in space) of a 300 mm long model for different inlet fluid velocities.

with the parabolic velocity profile could be solved analytically. Due to the definition of the heat transfer coefficient and depending on the thermal asymmetry, the Nusselt number could have a vertical asymptote or become zero.

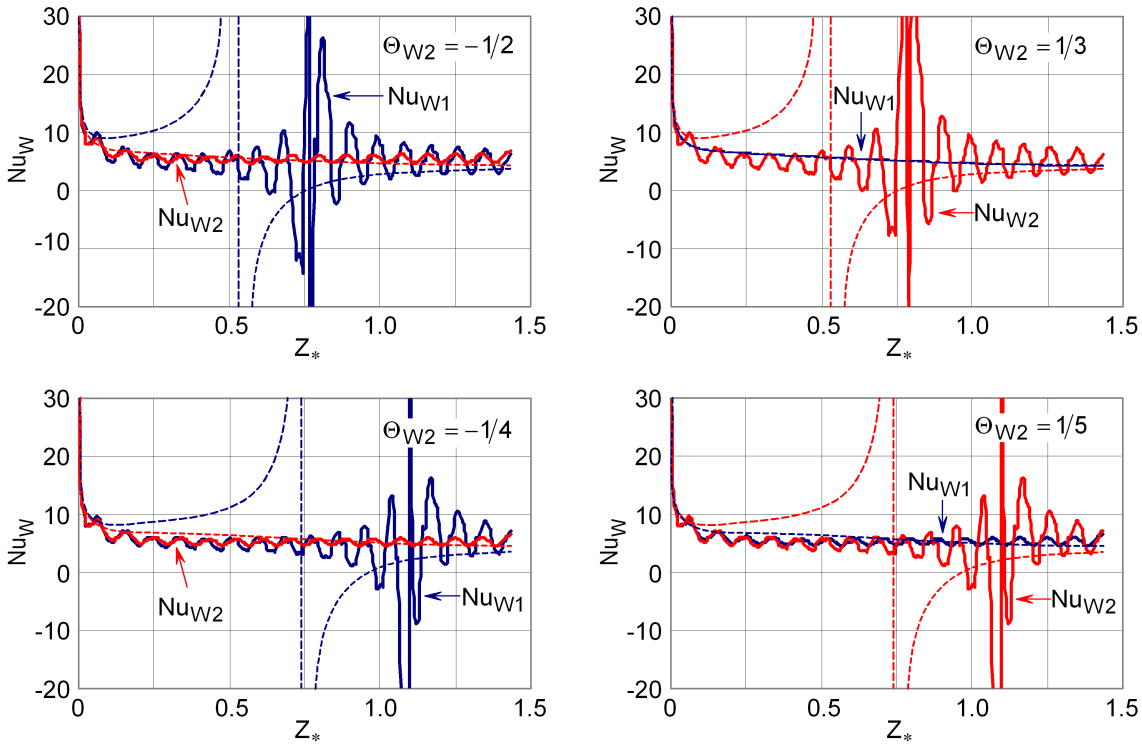

Figure 5.36: Nusselt number distributions at different Θ_{W2}; $\Theta_{W1} = 0$, $Re = 100$. The thin lines represent the corresponding distributions for the parallel plate channel, Figure 3.13.

The similarities and differences in heat transfer in the parallel plate channel and thermoplate are discussed in this section. One thermoplate with the geometrical parameters and thermally asymmetric boundary conditions specified in Table 4.5 was chosen to compare the heat transfer character in thermoplate with the one in parallel plate channel. The Nusselt number distributions for the lower and upper thermoplate wall, Nu_{W1} and Nu_{W2} respectively, are illustrated in Figure 5.36. The thin lines represent the corresponding distributions for the parallel plate channel, as it was shown in Figure 3.13, in Chapter 3.

The Figure 5.36 shows that the Nusselt number distributions, Nu_{W1} or Nu_{W2}, can have a vertical asymptote and become zero also in case of a thermoplate, that is exposed to thermally asymmetric boundary conditions, for certain combinations of the boundary conditions T_{IN}, T_{W1} and T_{W2}, i.e. Θ_{W2}, similar as in the case of the parallel plate channel. The conditions for this to happen are the same as in the case of the parallel plate channel, Section 3.3.1. Since the Nusselt number distribution in case of parallel

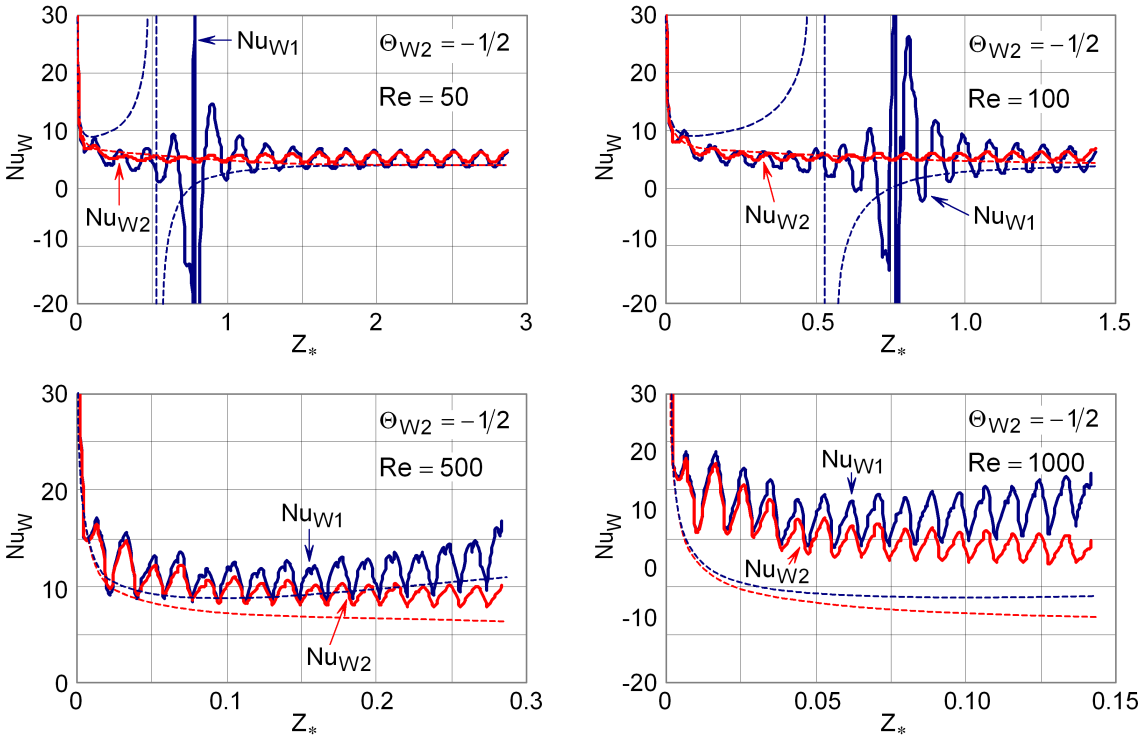

Figure 5.37: Nusselt number distributions at different Θ_{W2}; $\Theta_{W1} = 0$, $Re = 100$. The thin lines represent the corresponding distributions for the parallel plate channel.

plates could become zero only once, in case of thermoplate it can become zero more than once, due to its oscillating character.

Although the Equations (3.44), (3.46) and (3.48) can not be used to calculate the positions where the Nusselt number experiences a vertical asymptote and zero in case of thermoplate, it was observed that the dependency 3.49:

$$(1 - \Theta_{W2(X=-1)})(1 - \Theta_{W2(X=+1)}) = 1, \tag{5.11}$$

holds in case of thermoplate, as well.

In Section 3.3 it has been observed, that in case of parallel plates the Nusselt number distributions, Nu_{W1} and Nu_{W2}, falling from the infinity follow the limit of $Nu_\infty = 7.545$ (symmetric case) in the region before the asymptote, i.e. $0 < Z_* < Z_{A*}$, first, and than the limit of $Nu_\infty = 4.0$, for $Z_* \to \infty$. The numerical simulations show that the corresponding distributions of Nusselt number oscillate around the same value before and after the vertical asymptote in case of heat transfer in thermoplate, Figure 5.36. This is an advantage of the thermoplate, since it seems to be not sensitive to the thermal asymmetry, as it is the case with the parallel plate channel, and the thermal asymmetry is rather the rule than the exception in the practice.

Furthermore, the Nusselt number distributions for the parallel plate channel does not depend on the Reynolds number, because its influence is taken into account through

Z_*, Equation (3.11). The diagram is only scaled in Z_* direction when the Reynolds number is changed. The situation changes in chase of thermoplates, where the Nusselt number distribution is influenced by the Reynolds number, not only through the scaling in the Z_* direction. In case of thermoplate, the average Nusselt number value increases, when the Reynolds number is raised, Figure 5.37.

5.4 Validation through Experiments

Despite various uses of thermoplates in heat exchangers, no relevant experimental data on fluid flow and heat transfer in thermoplates have been reported in the literature, the paper by Mitrović and Peterson [38] being an exception.

Since the part I of this paper deals with single phase forced convection heat transfer and pressure drop in a thermoplate, the data published there were convenient for the comparison with the numerical results of this thesis. The thermoplate made of 0.8 mm thick stainless steel sheets was installed vertically. It dimensions (width x height x thickness) were 300 mm x 1000 mm x 5 mm, Figure 5.38. The test plate was switched as a resistance heater into an electric circuit and the measured electrical resistance of the plate was used to determine its wall temperature. The plate was electrically disconnected from the rest of the plant by means of POM (Polyoxymethylene). For other details see the paper by Mitrović and Peterson, [38].

Due to the fact, that the experiments on heat transfer and pressure drop have been made using only one thermoplate geometry, the calculated Nusselt number and pressure drop values could be validated through experiments only as function of the Reynolds number and mass flow rate, respectively, and the thermoplate geometry could not be varied.

Marlotherm oil and distilled water were used as test fluids, because the electrical resistance of these fluids is high enough to allow the application of the electrical resistance heating method. The fluid properties of the Marlotherm oil and distilled water were adopted to be temperature dependent.

From the variety of the experimental runnings, for the comparison with the numerical results were chosen only those, where the inlet fluid temperature and the thermoplate wall temperature were kept approximately constant for all Reynolds numbers, Table 5.4, (Marlotherm oil at $Pr = 8.4$ and water at $Pr = 3.9$ in paper by Mitrović and Peterson [38]).

The influence of the connecting tubes and thermoplate edges was not known in advance. For that reason two sets of the numerical runnings have been made, one with the numerical model that consists of a thermoplate strip and the second one was a model describing the whole thermoplate inclusive the connecting tubes (by employing of the symmetry planes at $y = 0$ and $z = 0$ it was enough to simulate 1/4 of the thermoplate). The fact, that the maximal plate distance (interior channel hight) δ is

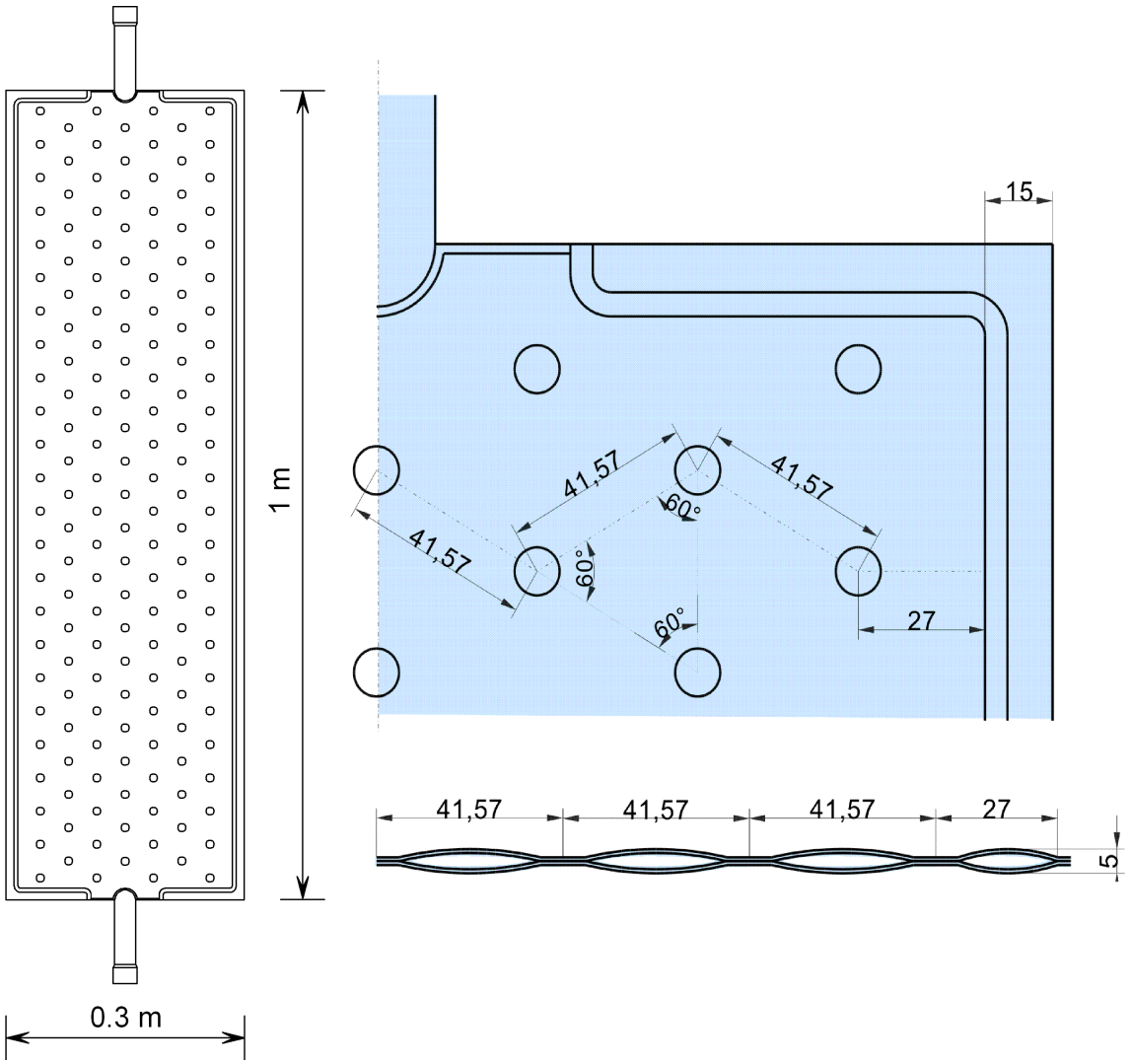

Figure 5.38: Geometry of the thermoplate used in experiments by Mitrović and Peterson, [38].

not constant in the reality, but a function of x and z coordinates, was taken into account by the numerical calculations. Still, a minor discrepancy between the real thermoplate geometry and the numerical model could not be avoided. Further, the thermoplate wall temperature, T_W, that was estimated by the experimental runnings represents rather an average temperature. This temperature was adopted for the wall boundary condition by the corresponding numerical experiments, because the exact temperature distribution over the thermoplate surface could not be measured by the available equipment. In the runnings the temperature difference $T_W - T_{IN}$ of only few degrees (less than 12K) could be established, Table 5.4, which challenges the modelling additionally. Defining a constant heat flux boundary condition at the thermoplate wall instead of the constant temperature did not result in better agreement with the experimental results.

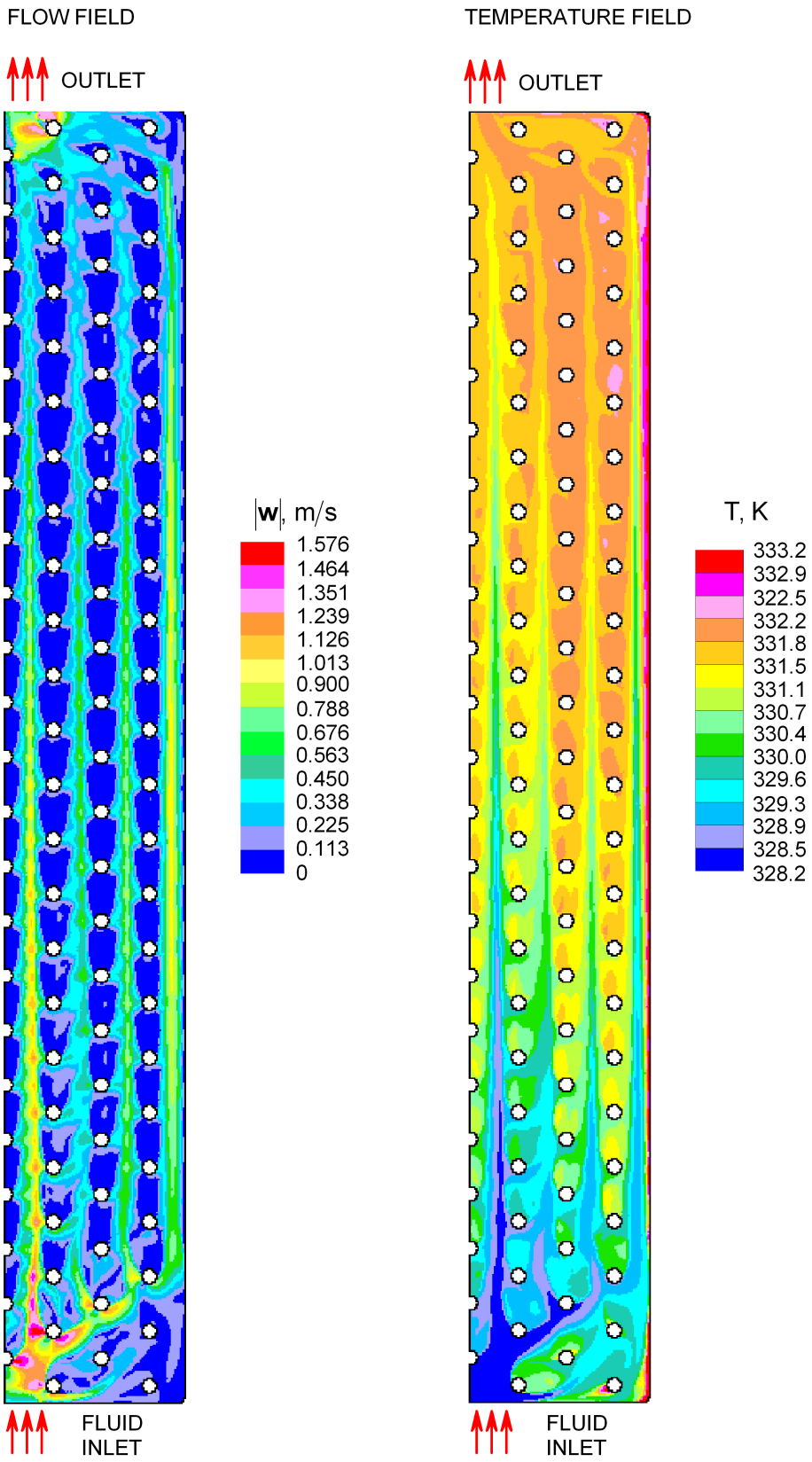

Figure 5.39: Flow field and temperature field distribution across the thermoplate; Marlotherm oil at $Re = 1860$, $\dot{m}_{IN} = 510\text{kg/h}$, $T_{IN} = 328.2\text{K}$, $T_W = 333.2\text{K}$.

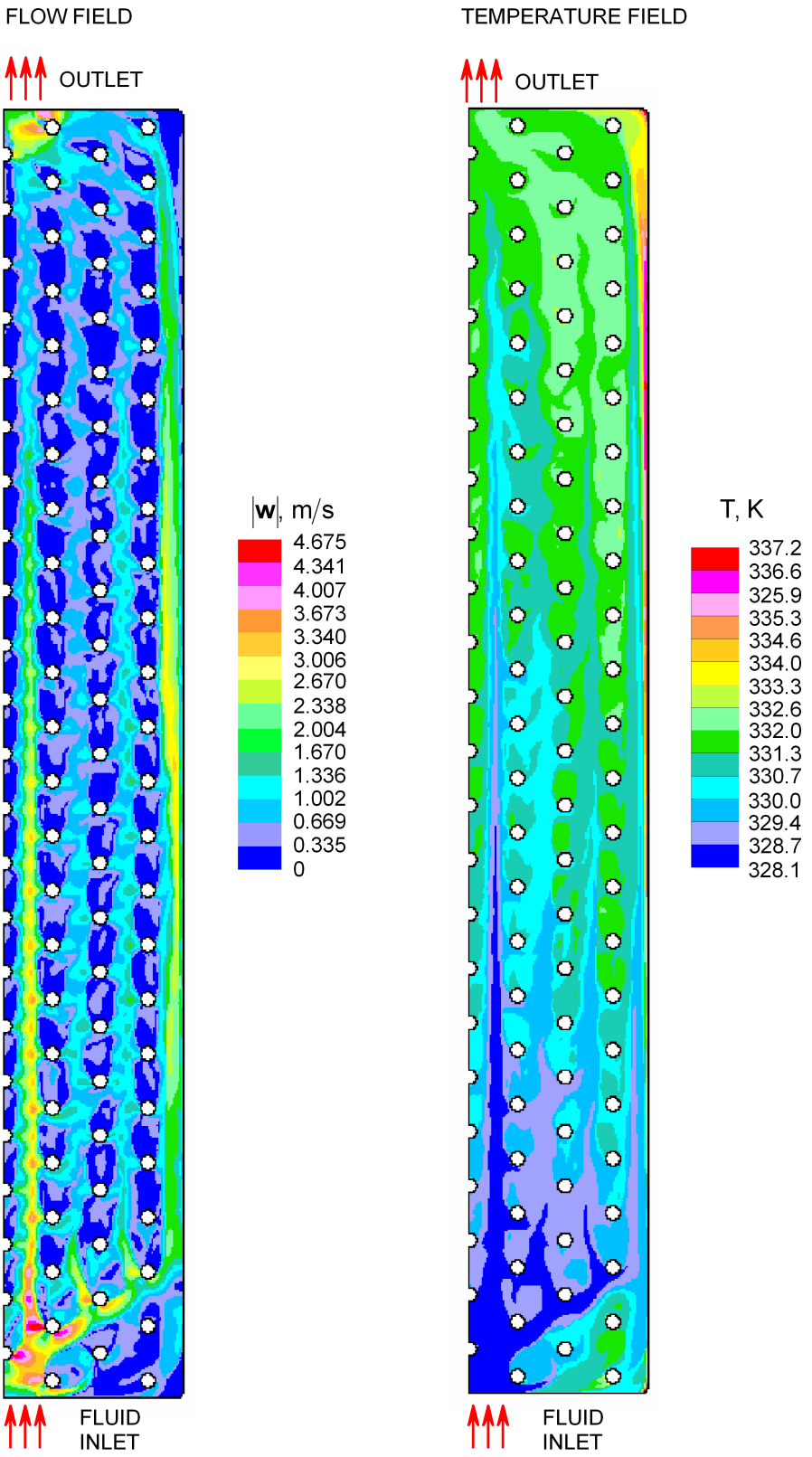

Figure 5.40: Flow field and temperature field distribution across the thermoplate; Marlotherm oil at $Re = 5416$, $\dot{m}_{IN} = 1500$kg/h, $T_{IN} = 328.1$K, $T_W = 337.2$K.

Table 5.4: Boundary conditions for the comparison with the experiments of Mitrović and Peterson.

Run	Marlotherm Oil			Water		
	$\dot{m}_{IN}$[kg/h]	T_{IN}[K]	T_W[K]	$\dot{m}_{IN}$[kg/h]	T_{IN}[K]	T_W[K]
1	510	328.2	333.2	455	314.2	325.3
2	1000	327.5	335.8	670	313.4	321.2
3	1280	327.9	336.5	837	314.6	321.0
4	1500	328.1	337.2	1016	314.8	320.1
5	2020	328.3	337.4	1238	315.8	320.5
6				1485	315.4	319.5
7				1684	315.9	319.6
8				1960	315.6	318.6
9				2199	315.9	318.9

By calculations with the thermoplate strip model, the effects of the thermoplate edges and connecting tubes could not be taken into account and had to be neglected. In this case the simplification was made that the fluid flows in with the mean velocity u_{IN} and temperature T_{IN} and passes homogeneously through the thermoplate that is kept at constant temperature T_W. Consequently, the recirculation zones that are expected to occur in the thermoplate corners and the heat transfer reduction because of this could not be captured with the thermoplate strip approach. The high temperature gradient in the developing region ($x \approx 0$) over the whole thermoplate width results in locally higher Nusselt number values (tend to the infinity), than it is expected to be in the reality. This will have an impact on the overall heat transfer.

Modeling the whole thermoplate shows that there are recirculation zones in the thermoplate corners near the inlet, but not at the other end, near the outlet, Figures 5.39 and 5.40. The fluid is heated up faster in the recirculation zones which causes reduction of the heat transfer to some extent. But on the other hand, according to the continuity equation the fluid is speeded up near the inlet, which increases the heat transfer (low temperature regions in Figures 5.39 and 5.40). These effects may compensate themselves if they are of the same order of magnitude. Depending on the Reynolds number, the former or the latter effect can outweigh. Inspecting the flow fields shown in Figures 5.39 and 5.40) it can be seen, that the fluid hits the welding points with high flow velocity near the inlet. Removing a few welding points from the near inlet region would reduce the overall pressure drop, which is the same conclusion that Witry et al. [73, 74] deduced from their numerical investigations. This could however allow the recirculation zones in the thermoplate corners to be greater.

Figures 5.41 and 5.42 illustrate calculated Nusselt number compared to the the one reported by Mitrović and Peterson [38], for the thermoplate strip and whole thermoplate model respectively. In principle, there is no big difference between these two diagrams.

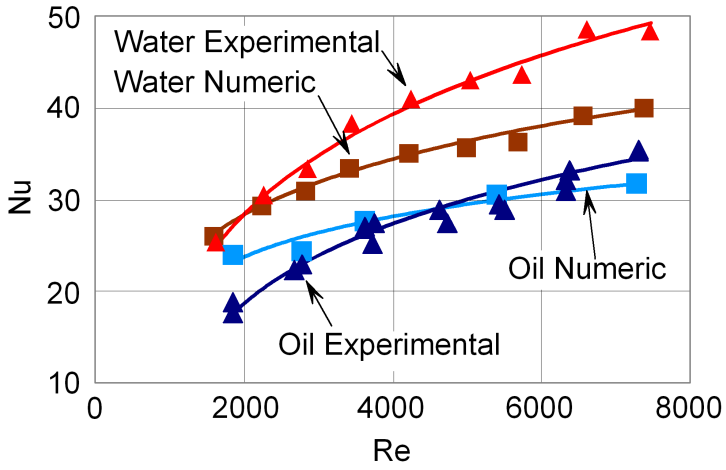

Figure 5.41: Nusselt number comparison for a thermoplate strip.

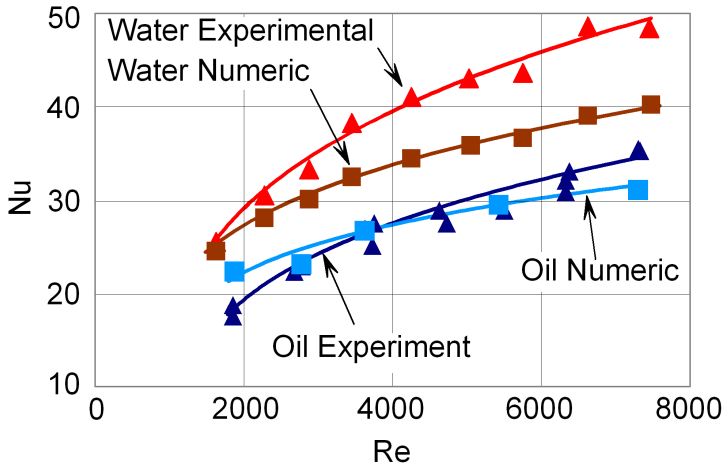

Figure 5.42: Nusselt number comparison for whole thermoplate.

The calculated Nusselt number values at lower Reynolds numbers for the thermoplate strip, Figure 5.41, are somewhat greater than those of the whole thermoplate, Figure 5.42. This means, that there is an influence of the connecting tubes and recirculation zones in the thermoplate corners only at lower Reynolds numbers, whereas at higher Reynolds numbers the heat transfer reduction is compensated by the heat transfer increase caused by the local speed up.

Further, Figures 5.41 and 5.42 show a good agreement between calculated and measured Nusselt number values for the Marlotherm oil. In case of distilled water the calculated Nusselt number is always clearly lower than the measured one, except for the low Reynolds numbers. This indicates that the turbulent effects play an important role at such regimes, which is not surprising. The differences between Nusselt number

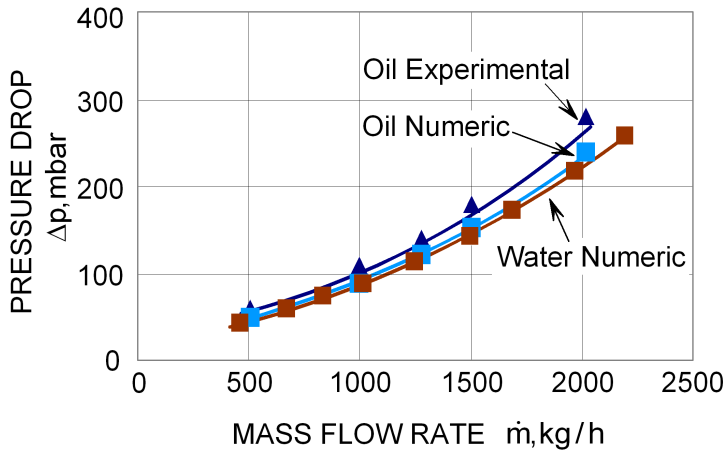

Figure 5.43: Pressure drop comparison for whole thermoplate.

behaviour for Marlotherm oil and water are associated with different fluid properties of these two fluids. Calculations with the standard k-ε model resulted in qualitative similar flow distribution but with much higher Nusselt number values in comparison to the measured ones. That was the reason for adopting the laminar model for all calculations presented in this thesis.

A comparison between calculated and measured pressure drop over the thermoplate as a function of the mass flow rate is given in Figure 5.43. Although the fluid properties of Marlotherm oil and water are different, the calculated pressure drop values are almost identical for these two fluids. The calculated values are lower than the measured ones and the discrepance increases with increasing mass flow rate. This can be attributed to the small inaccuracy in the geometry of the thermoplate connections with the inlet and outlet tube.

As it could be seen in this section, a very good agreement between the calculated and measured values for the Marlotherm oil could be achieved. For the distilled water a satisfactory agreement could not be reached at all Reynolds numbers. This makes clear that an appropriate turbulence model is anavoidable for the heat transfer quantification. Nevertheless, for the comparison purposes and finding an optimal thermoplate geometry, the methodology shown in this thesis is considered to be adequate.

6 Conclusions

This thesis deals with the forced convection and heat transfer in a parallel plate channel and in thermoplates under thermally symmetrical and asymmetrical boundary conditions.

In case of asymmetrically heated parallel plate channel the dimensionless energy equation could be solved analytically in form of Hermite polynomials and hypergeometric functions. Depending on the boundary conditions, the Nusselt number distribution at the lower or at the upper plate could experience a vertical asymtote and a zero value. A relation, that describes the dependency of the dimensionless temperatures of the upper plate, $\Theta_{W2(X=-1)}$, for the Nusselt number asymptotes to occur at the same axial position, Z_{A*}, at the lower and at the upper plate, respectively, was deduced. Further, it was shown, that a small thermal asymmetry reduces the Nusselt number from $Nu_\infty = 7.545$ (symmetric case) to $Nu_\infty = 4.0$ (asymmetric case).

The heat transfer can be increased up to four times in comparison to the parallel plate channel when thermoplates, whose surface can be described through trigonometric functions, are used. This enhancement has to be paid through higher pressure drop and pumping power. The numerical experiments reveal that the staggered welding spot pattern should be used to achieve better heat transfer. The welding spots pitch in the flow direction, s_L, does not play any important role in this case. Only at higher Reynolds numbers an optimum of $s_L \approx 80$mm occurs. The heat transfer is also improved chosing lower values for the transversal welding spot pitch, s_T, and the maximal plate distance, δ.

If the pressure drop and the pumping power are very important by the implementation of the thermoplates, a thermoplate that has even surface for the most part, as it is the case with the model 5, Figure 4.1e, is recommended. This thermoplate surface is approximated using an exponential function. Using this kind of thermoplate surface will not increase the heat transfer as much as in the case of using the model 1, Figure 4.1a, in comparison to the parallel plate channel. However, the low values of the pressure drop and pumping power result in a convenient thermo-fluid characteristic.

Contrary to the parallel plate channel, in the case of asymmetrical heating after one of the thermoplate walls experienced a vertical asymptote, thermoplates remain thermally active as in the region before the vertical asymptote. This distinguishes the thermoplates, since the thermal asymmetry is rather the rule than an exception in the practice. The higher Reynolds number results in higher Nusselt number when thermoplates are used, which is not the case with the prarallel plate channel.

A Nusselt number correlation as a function of the Reynolds number and three geometrical parameters of the thermoplate could be found, where the constants are calculated using the least squares method.

Some of the numerical results from this thesis could be compared to the laboratory experiments. A very good agreement was observed when Marlotherm oil was used as a test fluid. However, the comparison indicates, that the turbulence effects can not be neglected particularly at higher Reynolds numbers.

Bibliography

[1] Abramowitz, M. and Stegun, I.A., 1972, Handbook of mathematical functions,Dover Publications, New York.

[2] Anderson, J.D., 1995, Computational fluid dynamics, McGraw-Hill, Inc., New York.

[3] Behrend, H.-J., 1993, Thermoblechwärmetauscher und -apparate: Vielseitigkeit bewiesen, Schweizer Maschinenmarkt, 12, 95-97.

[4] Bird, R.B, Stewart, W.E. and Lightfoot, E.N., Transport phenomena (Revised 2nd Ed.), 2007, Wiley, New York.

[5] Blancher, S., Creff, R. and Quere, P.L., 1998, Effect of Tollmien Schlichting wave on convective heat transfer in a wavy channel. Part I: Linear analysis, International Journal of Heat and Fluid Flow, 19, 39-48.

[6] Burns, J.C, Parkers, T., 1967, Peristatic motion, Journal of Fluid Mechanics, 29, 731-743.

[7] CD adapco Group, 2004, Methodology StarCD version 3.24.

[8] Cherukat, P., Na, Y., Hanratty, T.J., and Mclaughlin, Y.B. 1998, Direct numerical simulation of a fully developed turbulent flow over a wavy wall, Theoretical and Computational Fluid Dynamics, 11, 109-134.

[9] Cho, K.J., Kim, M.U. and Shin, H.D., 1998, Linear stability of two-dimensional steady flow in wavy-walled channels, Fluid Dynamics Research, 23, 349-370.

[10] Deiber, J.A. and Schowalter, W.R., 1979, Flow through tubes with sinusoidal axial variations in diameter, AIChE Journal, 25, 638-645.

[11] Dellil, A.Z., Azzi, A. and Jubran, B.A., 2004, Turbulent flow and convective heat transfer in a wavy wall channel, Heat and Mass Transfer, 40, 793-799.

[12] Fan, R., 2007, Numerische Untersuchungen zum Wärmeübergang und Druckabfall in Thermoblechen, Bachelorarbeit, University of Paderborn.

[13] Ferziger, J.H. and Perić, M., 2002, Computational methods for fluid dynamics, Springer, Berlin.

[14] Garg, V.K. and Maji, P.K., 1988, Laminar flow and heat transfer in a periodically converging-diverging channel, International Journal for Numerical Methods in Fluids, 8, 579-597.

[15] Graetz, L., 1883, Ueber die Wärmeleitungsfähigkeit von Flüssigkeiten, Annalen der Physik NF, 18, 79-94.

[16] Grass, A.J., Stewart, R.J. and Mansour-Tehrani, M.,1991, Vortical structures and coherent motion in turbulent flow over smooth and rough boundaries, Philosophical Transactions of the Royal Society of London, Series A, 336, 35-65.

[17] Grimm, P., 2007, Numerische Untersuchung des Wärmeübergangs an Thermoblechen, Studienarbeit, University of Paderborn.

[18] Guzmán, A.M. and Amon, C.H., 1996, Dynamical flow characterization of transitional and chaotic regimes in converging-diverging channels, Journal of Fluid Mechanics, 321, 25-57.

[19] Hatton, A.P and Turton, J.S., 1962, Heat transfer in the thermal entry length with laminar flow between parallel walls at unequal temperatures, International Journal of Heat Mass Transfer, 5, 673-679.

[20] Heckel, W., 2007, Numerische Untersuchungen zur Wärmeübertragung in Thermoblechen, Studienarbeit, University of Paderborn.

[21] Hossain, M.Z. and Islam, A.K.M.S., 2004, Fully developed flow structures and heat transfer in sine-shaped wavy channels, International Communications in Heat Mass Transfer, 31, 887-896.

[22] Hossain, M.Z. and Islam, A.K.M.S., 2007, Numerical investigation of fluid flow and heat transfer characteristics in sine, triangular, and arc-shaped channels, Thermal Science, 11, 17-26.

[23] Kakaç, S., Shah, R.K. and Aung, W., 1987, Handbook of single-phase convective heat transfer,John Wiley & Sons, New York.

[24] Kim, S.K., 2001, An experimental study of flow in a wavy channel by PIV, Proceedings of the 6th Asian Symposium on Visualisation, Busan, Korea.

[25] Lahbabi, A. and Chang, H.C., 1986, Flow in periodically constricted tubes: Transition to inertial and nonsteady flows, Chemical Engineering Science, 41, 2487-2505.

[26] Lee, B.S., Kang, I.S. and Lim, H.C., 1999, Chaotic mixing and mass transfer enhancement by pulsatile laminar flow in an axisimmetric wavy channel, International Journal of Heat Mass Transfer, 42, 2571-2581.

[27] Li, Y., 2007, Numerische Untersuchungen zur Hydrodynamik und zum Wärmebergang in Thermoblechen, Bachelorarbeit, University of Paderborn.

[28] Mahmud, S., Islam, A.K.M.S. and Mamun, M.A.H., 2002, Separation characteristics of fluid flow insice two parallel plates with wavy surface, International Journal of Engineering Science, 40, 1495-1509.

[29] Mahmud, S. and Islam, 2003, Laminar free convection and entropy generation inside an inclined wavy enclosure, International Journal of Thermal Sciences, 42, 1003-1012.

[30] Mahmud, S., Islam, A.K.M.S. and Feroz, C.M., 2003, Flow and heat transfer characteristic inside a wavy tube, Heat and Mass Transfer, 39, 387-393.

[31] Maletić, B. and Mitrović, J., 2008, Influence of the thermoplate geometry on the heat transfer, Proceedings of the 5th European Thermal-Sciences Conference EUROTHERM 2008, HEX27, Eindhoven, The Netherlands.

[32] Mitrović, J., Maletić, B. and Bačlić, B.S., 2006, Some peculiarities of the asymetric Graetz problem, International Journal of Engineering Science, 44, 436-455.

[33] Mitrović, J. and Maletić, B. 2005, Effect of thermal assymetry on heat transfer in a laminar annular flow, Chemical Engineering and Technology, 28, 1144-1150.

[34] Mitrović, J. and Maletić, B., 2006, Numerical simulation of fluid flow and heat transfer in thermoplates, Proceedings of the 13th International Heat Transfer Conference IHTC-13, HEX-10, Sydney, Australia.

[35] Mitrović, J. and Maletić, B., 2007, Numerical simulation of fluid flow, heat transfer and pressure drop in thermoplates, Proceedings of the 5th International Conference on Heat Transfer, Fluid Mechanics and Thermodynamics HEFAT2007, MJ3, Sun City, South Africa.

[36] Mitrović, J. and Maletić, B., 2007, Numerical simulation of fluid flow and heat transfer in thermoplates, International Journal of Heat Exchangers, in Press.

[37] Mitrović, J. and Maletić, B., 2007, Heat transfer with laminar forced convection in a porous channel exposed to a thermal asymmetry, International Journal of Heat and Mass Transfer, 50, 1106-1121.

[38] Mitrović, J. and Peterson, R., 2007, Vapor condensation heat transfer in thermoplate heat exchanger, Chemical Engineering and Technology, 30, 907-919.

[39] Mühlthaler, W., 2002, Thermo-Blech Wärmeaustauscher-Systeme, Absolventen Aktuell, 13, 2-3.

[40] Ničeno, B. and Nobile, E., 2001, Numerical analysis of fluid flow and heat transfer in periodic wavy channels, International Journal of Heat and Fluid Flow, 22, 156-167.

[41] Nield, D.A., 2004, Forced convection in a parallel plate channel with asymmetric heating, International Journal of Heat and Mass Transfer, 47, 5609-5612.

[42] Nishimura, T., Murakami, S., Arakawa, S. and Kawamura Y., 1990, Flow observation and mass transfer in sinusoidal wavy-walled channel at moderate Reynolds numbers for steady flow, International Journal of Heat and Mass Transfer, 33, 835-845.

[43] Nishimura, T., Bian, Y.N., Matsumoto, K. and Kunitsugu K., 2003, Fluid flow and mass transfer in a sinusoidal wavy-walled tube at moderate Reynolds numbers for steady flow, Heat and Mass Transfer, 39, 239-248.

[44] Nishimura, T., Arakawa, S., Murakami, S. and Kawamura Y., 1989, Oscillatory viscous flow in symmetric wavy-walled channels, Chemical Engineering Science, 44, 2137-2148.

[45] Nishimura, Murakami, S. and Kawamura Y., 1993, Mass transfer in a symmetric sinusoidal wavy-walled channel for oscillatory flow, Chemical Engineering Science, 48, 1793-1800.

[46] Nishimura, T., Ohori, Y. and Kawamura, Y.,1984, Flow characteristics in a channel with symmetric wavy wall for steady flow, Journal of Chemical Engineering of Japan, 17, 466-471.

[47] Nishimura, T., Ohori, Y., Kajimoto, Y. and Kawamura, Y.,1985, Mass transfer characteristics in a channel with symmetric wavy wall for steady flow, Journal of Chemical Engineering of Japan, 18, 550-555.

[48] Nishimura, T. and Matsune, S., 1996, Mass transfer enhancement in a sinusoidal wavy channel for pulsatile flow, Heat and Mass Transfer, 32, 65-72.

[49] Nishimura, T. and Matsune, S., 1998, Vortices and wall shear stresses in asymmetric and symmetric channels with winusoidal wavy walls for pulsatile flow at low Reynolds numbers, International Journal of Heat and Fluid Flow, 19, 583-593.

[50] Petukhov, B.S., 1967, Laminar fluid flow and heat transfer in ducts (in Russian), Energiya, Moscow.

[51] Ralph, M.E., 1987, Steady flow structures and pressure drops in wavy-walled tubes, Journal of Fluids Engineering, 109, 255-261.

[52] Rush, T.A., Newell, T.A. and Jacobi, A.M., 1999, An experimental study of fluid flow and heat transfer in sinusoidal wavy passages, International Journal of Heat and Mass Transfer, 42, 1541-1553.

[53] Russ, G. and Beer, H., 1997, Heat transfer and flow field in a pipe with sinusoidal wavy surface - I. Numerical investigation, II. Experimental investigation, International Journal of Heat and Mass Transfer, 40, 1061-1081.

[54] Saha, L.M. and Debnath, L., 1973, Unsteady boundary layer flows induced by a wavy plate, Pure and Applied Geophysics, 105, 802-809.

[55] Saniei, N. and Dini, S., 1993, Heat transfer characteristics in wavy-walled channel, ASME Journal of Heat Transfer, 115, 788-792.

[56] Sawyers, D.R., Sen, M. and Chang, H.-C., 1998, Heat transfer enhancement in three-dimensional corrugated channel flow, International Journal of Heat and Mass Transfer, 41, 3559-3573.

[57] Selvarajan, S., Tulapurkara, E.G. and Vasanta Ram, V., 1998, A numerical study of flow through wavy-walled channels, International Journal for Numerical Methods in Fluids, 26, 519-531.

[58] Schlichting, H. and Gersten, K., 1997, Grenzschicht-Theorie, Springer, Berlin.

[59] Shah, R.K. and London, A.L., 1978, Laminar flow forced convection in ducts, supplement to advances in heat transfer, Academic Press, New York.

[60] Slater, L.J., 1960, Confluent hypergeometric functions, Cambridge University Press, Cambridge.

[61] Sparrow, E.M. and Prata, A.T., 1983, Numerical solutions for laminar flow and heat transfer in a periodically converging-diverging tube, with experimental confirmation, Numerical Heat Transfer, Part A, 6, 441-461.

[62] Stephan, K. and Mitrović, J., 1984, Maßnahmen zur Intensivierung des Wärmeübergangs, Chemie - Ingenieur - Technik, 56, 427-431.

[63] Stone, K. and Vanka, S.P., 1999, Numerical study of developing flow and heat transfer in a wavy passage, Journal of Fluids Engineering, 121, 713-719.

[64] URL. DEG-Engineering GmbH. `http://www.deg-engineering.de/produktee.htm`

[65] URL. GEA FlatPlate Inc.. `http://www.heatexchangers.org/info/heatexchangers/`

[66] URL. OMEGA Heat Transfer Technology. `http://www.heseco.com/platecoil.htm`

[67] Utamura, M., Nikitin, K. and Kato, Y., 2007, Generalization of logarithmic mean temperature difference method for heat exchangers performance analysis, Thermal Science and Engineering, 15, 163-173.

[68] Versteeg, H.K. and Malalasekera, W., 1995, An introduction to computational fluid dynamics - The finite volume method, Prentice Hall, Harlow.

[69] Wang, C.C. and Chen, C.K., 2002, Forced convection in a wavy-wall channel, International Journal of Heat and Mass Transfer, 45, 2587-2595.

[70] Wang, G. and Vanka S.P., 1995, Convective heat transfer in periodic wavy passages, International Journal of Heat and Mass Transfer, 38, 3219-3230.

[71] Webb, R.L. and Kim, N.-H., Principles of enhanced heat transfer (2nd Ed.), 2005, Taylor & Francis, New York.

[72] Wirtz, R.A., Huang, F. and Greiner, M., 1999, Correlation of fully developed heat transfer and pressure drop in a symmetrically grooved channel, Transactions of the ASME, 121, 236-239.

[73] Witry, A., Al-Hajeri, M.H. and Bondok, A.A, 2005, Thermal performance of automotive aluminium plate radiator, Applied Thermal Engineering, 25, 1207-1218.

[74] Witry, A., Al-Hajeri, M.H. and Bondok, A.A, 2003, CFD Analyses of fluid flow and heat transfer in patterned roll-bonded Aluminium plate radiators, Proceedings of the 3rd International Conference on CFD in the Minerals and Process Industries CSIRO, Melbourne, Australia.

A Numerical Method

As it is well-known from the literature, an analytical solution to the set of the governing equations (4.17) to (4.21) can be obtained only for very simplified flow situations. However, for the engineering practice it is often of big importance to solve this set of partial differential equations employing also complex bounadary conditions, which is only possible if a numerical method is used. For that reason, a number of numerical methods (the finite difference method, the finite volume method, the finite element method, the volume of fluid and so on) and CFD[1] codes (FLUENT, StarCD, OpenFOAM, PHOENICS, FLOW3D and others) have been developed. For the numerical calculations presented in this thesis the commertial software StarCD that uses the finite volume method was used. In the next sections a short overview of this method will be given; for more details the original literature sources such as the books by Versteeg and Malalasekera [68], Anderson [2] and Ferziger and Peric [13] are recommended.

A.1 The finite volume method

If we consider the governing Equations (4.17) to (4.21) it is clear that there is a possibility to write them in one common form introducing a general variable ϕ

$$\frac{\partial(\rho\phi)}{\partial t} + div(\rho\phi\boldsymbol{w}) = div(\Gamma_\phi grad\phi) + S_\phi. \tag{A.1}$$

The governing equations (4.17) to (4.21) are obtained from (A.1) by setting ϕ equal to 1, u, v, w or i (i.e. T) and selecting appropriate values for the diffusion coefficient Γ and the source term S_ϕ.

In the finite volume method, the Equation (A.1) is used as a basic equation for computationoal procedures. The crucial step of this method is the integration of the Equation (A.1) over a three-dimensional control volume CV yielding

$$\int_{CV} \frac{\partial(\rho\phi)}{\partial t} dV + \int_{CV} div(\rho\phi\boldsymbol{w}) dV = \int_{CV} div(\Gamma_\phi grad\phi) dV + \int_{CV} S_\phi dV. \tag{A.2}$$

Using the Gauss' divergence theorem, the convective term and the diffusive term can be rewritten as surface integral over the entire bounding surface of the control volume,

[1] **C**omputational **F**luid **D**ynamics

and for the steady state problems, the Equation (A.1) becomes

$$\int_A \boldsymbol{n}\rho\phi\boldsymbol{w}dA = \int_A \boldsymbol{n}\Gamma_\phi grad\phi dA + \int_{CV} S_\phi dV, \tag{A.3}$$

whereas for the time dependent problems, an integration with respect to time t over a small interval Δt is necessary, which yields

$$\int_{\Delta t}\frac{\partial}{\partial t}\int_{CV}(\rho\phi)dV + \int_{\Delta t}\int_A \boldsymbol{n}\rho\phi\boldsymbol{w}dA = \int_{\Delta t}\int_A \boldsymbol{n}\Gamma_\phi grad\phi dA + \int_{\Delta t}\int_{CV} S_\phi dV, \tag{A.4}$$

where the order of integration and differentiantion in the first term on the left hand side has been changed, which is allowed, if the control volume is independent on time. Steady state calculations will be considered first, and than time dependent ones.

A.1.1 Steady state calculations

The division of the domain into discrete control volumes, i.e. numerical cells, is the first important step in the finite volume method. The usual notation convention of CFD methods is shown in Figure A.1. A cell characterised by the node P is surrounded by

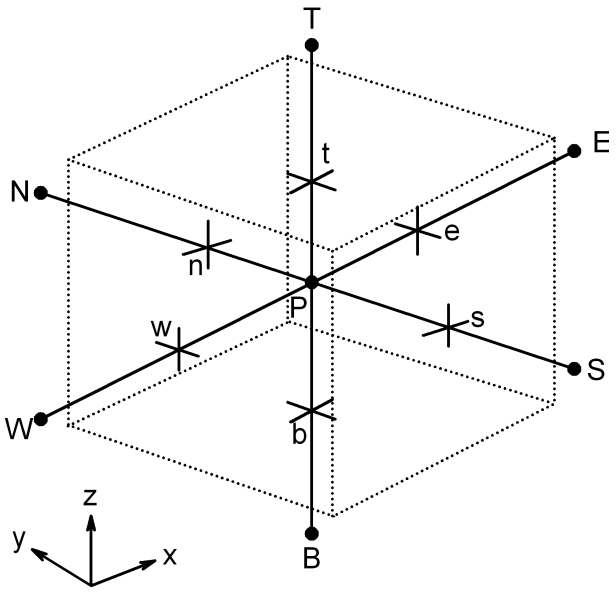

Figure A.1: A three-dimensional cell with the node P and neighbouring nodes W, E, S, N, B and T, [68].

six neighbouring cells and their nodes are identified as west, east, south, north, bottom and top (W, E, S, N, B, T). The six cell faces are denoted analogical by w, e, s, n, b and t.

The second important step of the finite volume method is the integration of the governing Equation (A.2) over a control volume to get a discretised equation at its nodal point P, which has the following general form:

$$a_P\phi_P = \sum a_{nb}\phi_{nb} + S_u = a_W\phi_W + a_E\phi_E + a_S\phi_S + a_N\phi_N + a_B\phi_B + a_T\phi_T + S_u, \quad \text{(A.5)}$$

where the source term from the Equation (A.2) is taken to have a linear form:

$$\int_{CV} S_\phi dV = \bar{S}\Delta V = S_u + S_p\phi_p, \quad \text{(A.6)}$$

and the coefficients a_i satisfy the following relation

$$a_p = \sum a_{nb} + \Delta F - S_p, \quad \text{(A.7)}$$

where F represents the convective mass flux per unit area at cell face. The calculation of the coefficients a_p, a_{nb} and F_i and the system of the algebraic equations describing the physical situation depend on the differencing scheme that is used.

A.1.1.1 Differencing schemes

A numerical solution to the transport equation is, in theory, indistinguishable from its exact solution only if the number of computational cells is infinitely large. However, in practical calculations only a finite number of cells can be used and the numerical results will only be physically realistic when the discretisation scheme has certan fundamental properties, and the most important ones are:

- Conservativeness. The flux of ϕ leaving a control volume through a certain cell face must be equal to the flux of ϕ entering the adjacent control volume through the same face, to ensure conservation of ϕ.
- Boundedness. The differencing scheme should produce such coefficients a_i, such that the matrix of the set of the algebraic equations is diagonally dominant. This ensures that in absence of sources, the internal nodal values of the property ϕ are bounded by its boundary values.
- Transportiveness. It is very important that the differencing scheme is not influenced by the direction and rate of the convective flow, which can be expressed in terms of the dimensionless cell Péclet number, that is defined as the ratio of the convective mass flux per unit area and the diffusion conductance at cell faces. For one-dimensional calculations Péclet number becomes

  $$Pe = \frac{F}{D} = \frac{\rho u}{\Gamma/\Delta x}, \quad \text{(A.8)}$$

  where Δx represents characteristic length, i.e. cell width in x direction.This interplay is ilustrated in Figure A.2 as the dependency of a countour of constant ϕ on Péclet number.

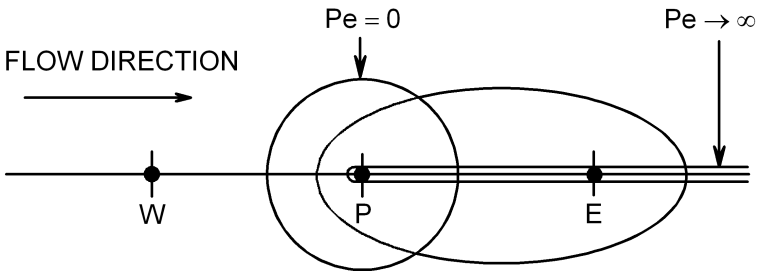

Figure A.2: Contours of constant ϕ at different Péclet numbers [68].

Depending on how the convective terms F on the cell faces are calculated, there are a few different differencing schemes:

- The central differencing scheme. To compute the cell face value the linear interpolation between the two neighbouring cell nodes is used. This differencing scheme has second-order accuracy in terms of Taylor series truncation error, but it is stable and accurate only if $Pe < 2$, which means only in diffusion-dominated low Reynolds number flows or if the grid spacing is small, because it is not able to identify the flow direction. This creates the need for other differencing schemes.

- The upwind differencing scheme. In convective flow, the cell face value is strongly influenced by the value of property ϕ at the upstream cell node. In this differencing scheme it is taken that the value at the cell face is equal to the value at the upstream node, so taking into account the flow direction, Figure A.3. This differencing scheme has only first order accuracy and produces erroneous results when the flow is not aligned with the grid lines. The error has a diffusion-like appearance and is called false diffusion. However, because of its simplicity, the upwind differencing scheme is widely used in CFD calculations.

- The hybrid differencing scheme. This differencing scheme represents a combination of the central differencing scheme for $Pe < 2$ and the upwind scheme for $Pe \geq 2$

- The power low differencing scheme is more accurate than the hybrid scheme. For $Pe \geq 10$ the diffusion is set to zero, and for $0 < Pe < 10$ the flux at the cell face is calculated according to a polynomial expression.

- The QUICK[2] differencing scheme uses a tree-point upstream-weighted quadratic interpolation for cell face values. This scheme has greater accuracy than the central differencing or hybrid schemes, but it can give some unterschoots and overshoots and in complex flow calculations the stability problems may occur.

- Other higher order schemes were developed for calculating of convective terms, but the implementation of the boundary conditions can be problematic.

[2] **Q**uadratic **U**pstream **I**nterpolation for **C**onvective **K**inetics

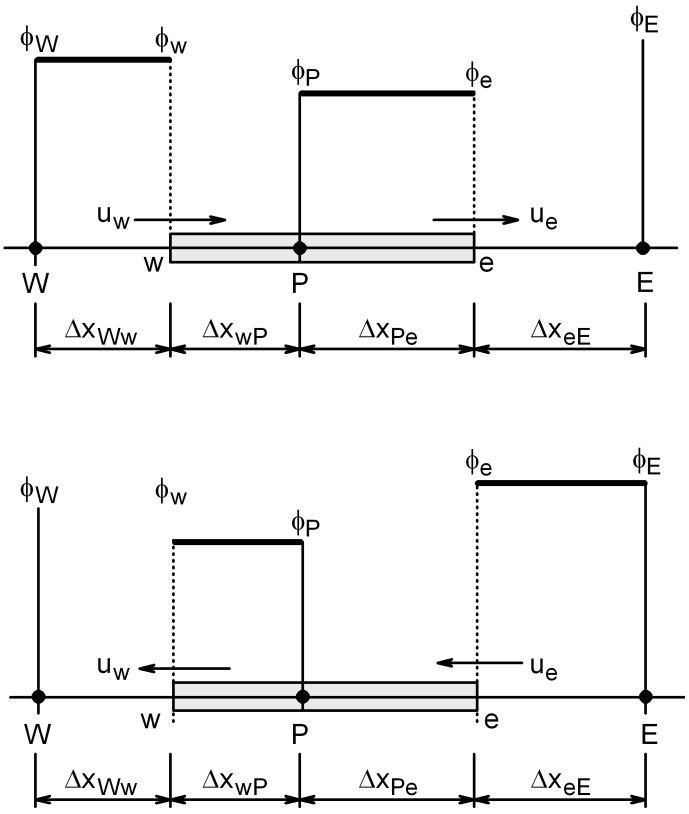

Figure A.3: The upwind differencing scheme for one-dimensional flows [68].

A.1.1.2 The SIMPLE algorithm

In the previous section (A.1.1.1) it was assumed that the velocity field was known, but in general it is not the case and the velocity field has to be computed. It is governed by the momentum equations (4.18) to (4.20) and must also satisfy the continuity equation (4.17). If the flow is compressible, the continuity equation is used as transport equation for density and the pressure can be obtained employing the equation of state (4.9). Otherwise, if the flow is incompressible, the density is constant and not linked to the pressure.

The momentum equations are coupled, contain non-linear quantities and the pressure gradient appears in all of them, without any additional equation for pressure. These problems can be solved by adopting an iterative strategy such as the SIMPLE[3] algorithm of Patankar and Spalding.

Here it is to be noted that if pressure and velocity components are calculated at the same nodes, a highly irregular pressure field, i.e. checker-board pressure field, could appear as constant [68]. One of the possibilities to solve this problem is to use a staggered

[3] **S**emi-**I**mplicit **M**ethod for **P**ressure-**L**inked **E**quations

grid for the velocity components, Figure A.4. In that way, the pressure and other scalar values are calculated at the node I, J, whereas the velocity components are calculated at other cells, i, J and I, j, whose nodes coincide with the faces of the cell I, J. There are, however, also other possibilities to solve this problem [13] and the StarCD software does not use the staggereg grid.

In this approach, where velocity and pressure fields are not known, the pressure gradient term of the momentum equations, which forms the main momentum source term, is written as an additional source term of the discretised momentum equations. In two-dimensional case the discretised momentum equations become

$$a_{i,J}u_{i,J} = \sum a_{nb}u_{n,b} - \frac{p_{I,J} - p_{I-1,J}}{\Delta x_u}\Delta V_u + \bar{S}\Delta V_u, \tag{A.9}$$

$$a_{I,j}v_{I,j} = \sum a_{nb}v_{n,b} - \frac{p_{I,J} - p_{I,J-1}}{\Delta x_v}\Delta V_v + \bar{S}\Delta V_v, \tag{A.10}$$

where ΔV_u and ΔV_v denote the volume of the u and v-cell, respectively.

The SIMPLE procedure is initiated after the velocity field $\tilde{u}^*$ and $\tilde{v}^*$ is guessed. Now the coefficients $a_{i,j}$ and a_{nb} can be calculated using any of the differencing schemes suitable for a concrete simulation. With the guessed pressure field p^* the discretised momentum equations (A.9) and (A.10) can be solved for the new values u^* and v^*

$$a_{i,J}u^*_{i,J} = \sum a_{nb}u^*_{n,b} - \frac{p^*_{I,J} - p^*_{I-1,J}}{\Delta x_u}\Delta V_u + \bar{S}\Delta V_u, \tag{A.11}$$

$$a_{I,j}v^*_{I,j} = \sum a_{nb}v^*_{n,b} - \frac{p^*_{I,J} - p^*_{I,J-1}}{\Delta x_v}\Delta V_v + \bar{S}\Delta V_v. \tag{A.12}$$

Introducing the pressure and the velocity corrections p', u' and v' the correct values for the pressure and the velocity comopnents become

$$p = p^* + p', \tag{A.13}$$

$$u = u^* + u', \tag{A.14}$$

$$v = v^* + v'. \tag{A.15}$$

Combining the equations (A.9) to (A.15), the expressions for the calculations of the velocity corrections u' and v' are obtained as follows

$$a_{i,J}u'_{i,J} = \sum a_{nb}u'_{n,b} - \frac{p'_{I,J} - p'_{I-1,J}}{\Delta x_u}\Delta V_u + \bar{S}\Delta V_u, \tag{A.16}$$

$$a_{I,j}v'_{I,j} = \sum a_{nb}v'_{n,b} - \frac{p'_{I,J} - p'_{I,J-1}}{\Delta x_v}\Delta V_v + \bar{S}\Delta V_v. \tag{A.17}$$

The main approximation of the SIMPLE algorithm is made by omitting the summation terms $\sum a_{nb}u'_{n,b}$ and $\sum a_{nb}u'_{n,b}$ in the Equations (A.16) and (A.17). The velocity components u and v are than

$$u_{i,J} = u^*_{i,J} + \frac{p'_{I-1,J} - p'_{I,J}}{\Delta x_u a_{i,J}}\Delta V_u + \bar{S}\Delta V_u, \tag{A.18}$$

$$v_{I,j} = v^*_{I,j} + \frac{p'_{I,J-1} - p'_{I,J}}{\Delta x_v a_{I,j}}\Delta V_v + \bar{S}\Delta V_v. \tag{A.19}$$

So far only the momentum equations have been considered, but the velocity components should also satisfy the continuity equation (4.17), which, combined with the eqations (A.16) and (A.17), results in the following relation

$$a_{I,J}p'_{I,J} = \sum a_{nb}p'_{n,b} + a'_{I,J}, \tag{A.20}$$

where $a_{i,j} = (\rho dA)_{i,j}$, dA representing the cell face surface and the source term $a'_{i,j}$ denotes the imbalance caused by the incorrect velocity field u^* and v^*. The Equation (A.20) can be solved for p' and is called the pressure correction equation.

Setting $p^* = p$, $\tilde{u}^* = u$ and $\tilde{v}^* = v$ this procedure is repeated until the converged solution is reached and the whole method is illustrated in Figure A.5.

The method can be improved by introducing of the unter-relaxation factors, since the correction equations often diverge.

There are also other algorithms used for solving the convection-diffusion problems with pressure linked equations, e.g. SIMPLER[4], SIMPLEC[5], PISO[6] and so on.

A.1.1.3 Convergence criteria

The StarCD solver provides the user with two types of output information, [7]. First one is monitoring values of all the dependent variables at a cell, specified by user. In case of steady state flows, necessary but not sufficient condition for achieving the solution is that the variation in the monitoring values should be less than some small tolerance specified by user. However, this information is not used for control purposes. Another type of the output information, that is used both for monitoring and control purposes is the residual. The residual at a particular cell P and iteration k for the variable ϕ, r^k_ϕ, is defined as the imbalance in the finite volume transport equation (A.5) arising from incomplete solution, i.e.

$$r^k_\phi \equiv a_P\phi^k_P - \sum a_i\phi^k_i - S_u, \tag{A.21}$$

[4]SIMPLE Revised
[5]SIMPLE Consistent
[6]**P**ressure **I**mplicit with **S**plitting of **O**perators

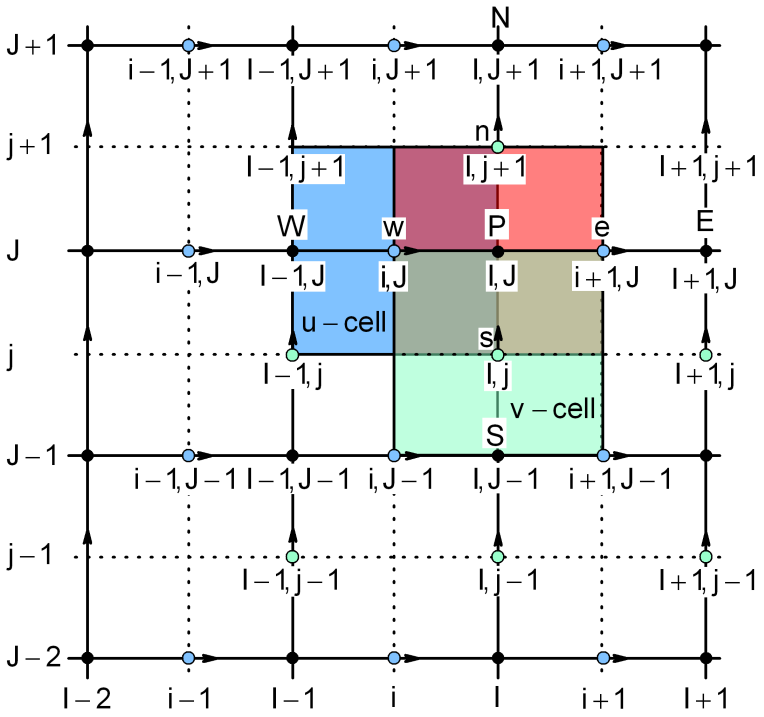

Figure A.4: The two-dimensional, backward staggered grid [68].

where the summation is over all neighbouring cells to the specific cell P.

The normalised absolute residual sum, which is actually used to judge convergence, is defined as follows

$$R_\phi^k \equiv \frac{\sum |r_\phi^k|}{M_\phi}. \tag{A.22}$$

The summation in the Equation (A.22) is done over all cells in the computational domain. The scaling factor M_ϕ used to normalise the residual sum is defined:

$$M_\phi = \sum_p a_p \phi_p^k. \tag{A.23}$$

At each iteration and for each variable, the values R_ϕ^k are computed and printed out. To decide when to terminate the calculations, the requirement

$$max(R_\phi^k) < \lambda, \tag{A.24}$$

stating that all residual have fallen below a tolerance prescribed by the user, must be satisfied.

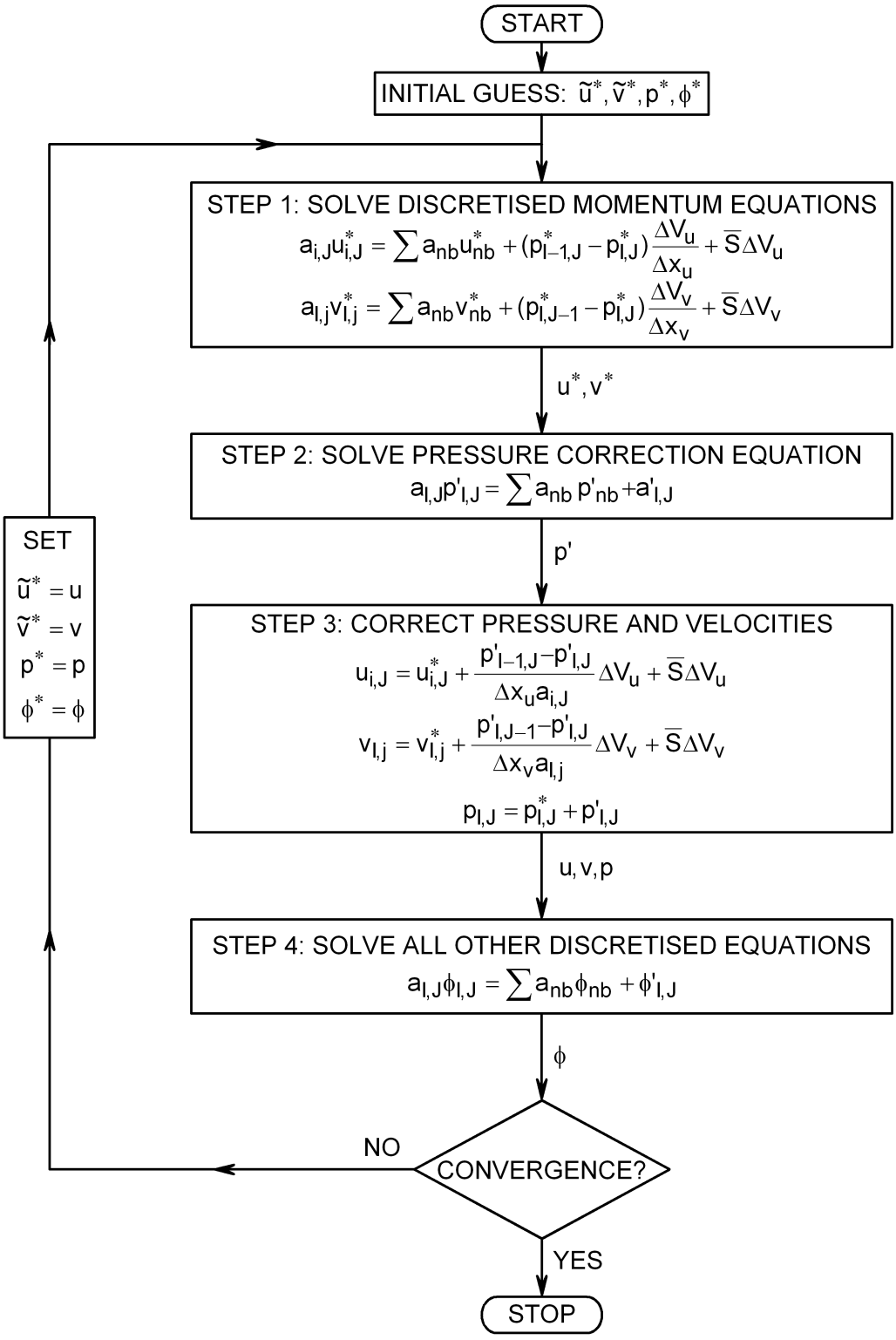

Figure A.5: The SIMPLE algorithm [68].

A.1.2 The finite volume method for time dependent flows

Before the Equation (A.4) can be integrated, i.e. discretised with respect to time, an assumption about the time dependancy of the values ϕ_P and ϕ_{nb} with time has to be made. To calculate the time integral from t to $t + \Delta t$, the values ϕ at time t or $t + \Delta t$, or a combination of these values can be used. This can be generalised by introducing a weighting parameter α between 0 and 1 and the time integral becomes

$$\int_{\Delta t} \phi dt = [\alpha\phi + (1 - \alpha)\phi^0]\Delta t, \tag{A.25}$$

where ϕ^0 and ϕ denote the values at time level t and $t + \Delta t$, respectively.

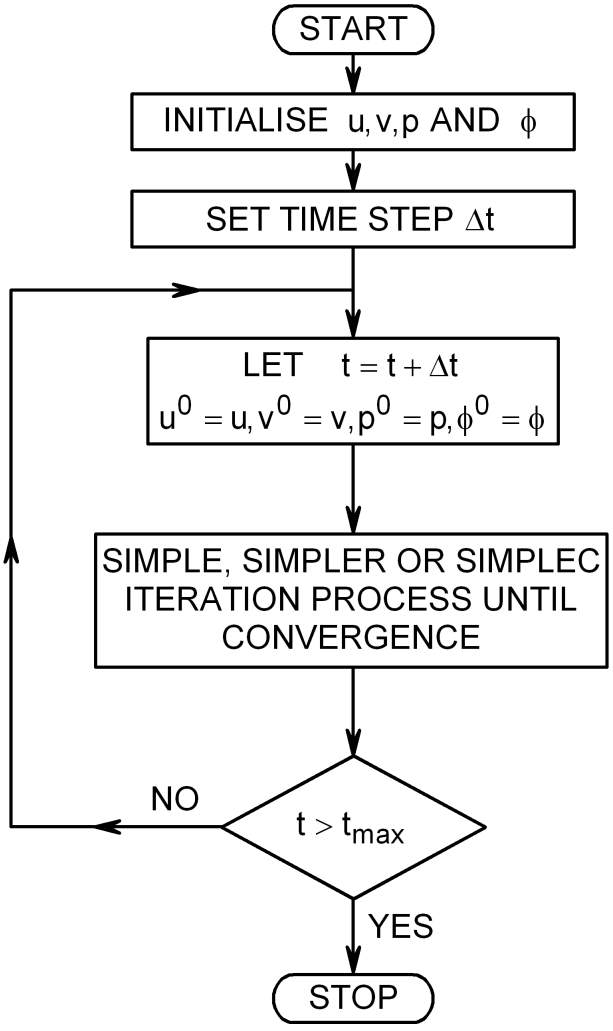

Figure A.6: The transient SIMPLE algorithm, [68].

Now the Equation (A.4) can be discretised and in general form it becomes

$$a_P\phi_P = \sum[a_{nb}(\alpha\phi_{nb} + (1-\alpha)\phi^0_{nb}] + [a^0_P - \sum(1-\alpha)a_{nb}]\phi^0_{nb} + S_u, \tag{A.26}$$

where the discretisation coefficients satisfy the following relation

$$a_P = \alpha(\sum a_{nb} - S_P) + a^0_P. \tag{A.27}$$

Setting $\alpha = 0$ the value ϕ_P (time level $t + \Delta t$) depends on ϕ^0_P and ϕ^0_{nb} (time level t), which gives the explicit discretisation scheme. On the contrary, if α is set equal to 1, the value ϕ_P at time level $t + \Delta t$ depends on values ϕ_{nb} at the same time level and on ϕ^0_P, which results in fully implicit discretisation scheme. A combination of these two schemes is possible, and, e.g. for $\alpha = 1/2$ we have so called Crank-Nicolson discretisation scheme, which is implicit, based on central differencing and it is second order accurate in time. The overall accuracy of the calculation depends, however, also on spatial discretisation, so the Crank-Nicolson scheme is often combined with spatial central differencing scheme.

The SIMPLE algorithm can be extended to transient calculations. The discretised time dependent continuity equation (4.17) will have the same form as (A.20), with the only difference, that the source term $a'_{I,J}$ is now the imbalance, caused not only by the incorrect velocity values, but also includes the time change of the fluid dencity ρ.

In transient flow calculations with the implicit discretisation, the iterative procedure described for steady state calculations such as SIMPLE is applied at each time step until the convergence criteria is satisfied, Figure A.6.

A.2 Discretised integrals for the process quantities

Once the governing equations are solved numerically, the velocity, pressure and the temperature field are known. Since these fields are not continuous, but rather discret fields, the integrals in the Equations (4.30) to (4.33) and (4.46) to (4.51) have also to be discretised.

Thus the the Equation (4.30) representing the mean fluid temperature at cross-section at distance x from the inlet can be discretised using the volumes of all the cells that are located between the current position x and $x + \Delta x$, Figure A.7

$$T_b(x) = \frac{\sum_{i=1}^{N} u_i T_i \Delta V_i}{\sum_{i=1}^{N} u_i \Delta V_i}, \tag{A.28}$$

where N means the number of cells placed in the region x and $x+\Delta x$, that is not constant along the channel. The statement above using the cell volume V_i is more suitable for calculations where the staggered grid is not used, than the definition that would use the cell face surfaces S_i.

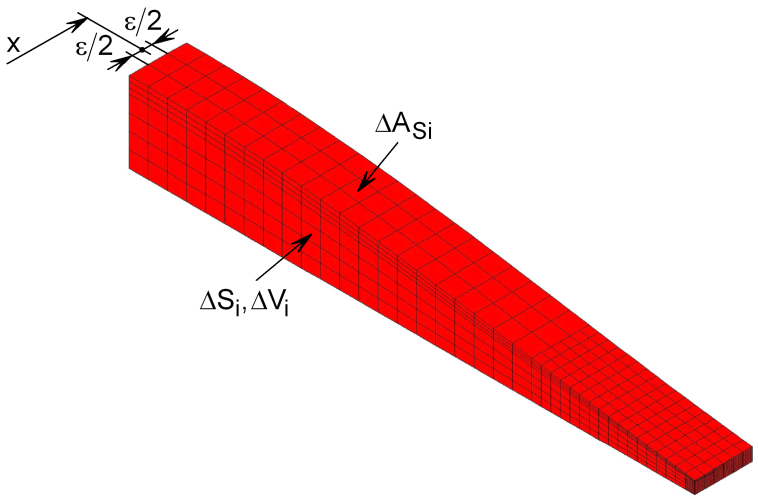

Figure A.7: Definitions of the elementary volume and surface.

Similar, the local heat flux at the wall is calculated as follows

$$\dot{q}(x) = \frac{\sum_{i=1}^{M} q_i \Delta A_{Si}}{\sum_{i=1}^{M} \Delta A_{Si}}, \tag{A.29}$$

where q_i represents the heat flux magnitude calculated at the boundary cell face ΔA_{Si} and M is the number of boundary cells that are placed between x and $x + \Delta x$.

For the average heat flux the equation of the same form as (A.29) is used, with the only difference, that M in this case denote the number of boundary cells, that are placed between $x = 0$ and $x + \Delta x$.

All other integrals defined in the section 4.3 are calculated in a similar way and all the variables defined in the section 4.3 are calculated in a post-processing user subroutine POSDAT.f that is used by the sofware StarCD and is given in Appendix B.

B Definition of the Model for StarCD

```
C*********************************************************************
      PROGRAM GITTER
C*********************************************************************
C DEFINES WHOLE THERMOPLATE MODEL OR A SECTION                        *
C*********************************************************************
      IMPLICIT NONE
      INTEGER NCX,NCZ,JJ,PHI(110),PH(110),M,IT
      INTEGER I,J,K,A,B,N1,N2,N3,N4,N5,N6,N7,N8,NV,NVX,NVZ,NVR
      REAL L,UIN,TIN,TW1,TW2,TT,RHOIN,LX,LZ
      DOUBLE PRECISION SL,SL1,ST,ST1,D,PI,VOL,VOL1
      DOUBLE PRECISION R,R1,R2,R3,R4,R5,X1,X2,XM,XX,XVD,Y1A,Y1B,Y2
      DOUBLE PRECISION F,FF,FF1,F1,F2,F2A,F3,F3A,F3B
      DOUBLE PRECISION F4,F41,F42,F43,FE1,FE2,FA1,FA2
      DOUBLE PRECISION F4A,F41A,F42A,F43A,DD
      DOUBLE PRECISION DX,DZ,XV,YV,ZV
      DOUBLE PRECISION XCS(110),YCS(110),ZCS(110)
      DOUBLE PRECISION XC(110),YC(110),ZC(110)
C---------------------------------------------------------------------*
C OVERALL SIZE AND GEOMETRY PARAMETERS OF THE MODEL HAVE TO BE SPECIFIED *
C---------------------------------------------------------------------*
      PARAMETER (LX=504)
      PARAMETER (LZ=36)
      PARAMETER (SL=42.)
      PARAMETER (SL1=0.)
      PARAMETER (ST=36.)
      PARAMETER (ST1=0.)
      PARAMETER (D=10.)
      PARAMETER (R1=D/2)
      PARAMETER (R2=15.)
      PARAMETER (PI=3.14159)
      PARAMETER (R3=12.)
      PARAMETER (R4=10.)
      PARAMETER (R5=8.1)
      PARAMETER (R=8)
```

```
C-----------------------------------------------------------------------*
C VALUES NEEDED FOR THE BOUNDARY CONDITIONS DEFINITION                  *
C-----------------------------------------------------------------------*
      PARAMETER(L=LX)
      PARAMETER(UIN=0.3)
      PARAMETER(TIN=293)
      PARAMETER(TW1=333)
      PARAMETER(TW2=333)
      PARAMETER(TT=1.E-4)
      PARAMETER(RHOIN=997.561)
      PARAMETER(IT=2000)
C CELL NUMBERS IN X AND Z DIRECTION
      PARAMETER (NCX=2*LX)
      PARAMETER (NCZ=2*LZ)
C CELL SIZE IN X AND Z DIRECTION
      PARAMETER (DX=LX/NCX)
      PARAMETER (DZ=LZ/NCZ)
C NUMBER OV VERTEX LINES IN X AND Z DIRECTION
      PARAMETER (NVX=NCX+1)
      PARAMETER (NVZ=NCZ+1)
      PARAMETER (NVR=NVX*NVZ)
C-----------------------------------------------------------------------*
C INPUT FILES FOR PROSTAR                                               *
C-----------------------------------------------------------------------*
      OPEN(UNIT=11,FILE='VERT1.INP',STATUS='NEW')
      OPEN(UNIT=12,FILE='VERT2.INP',STATUS='NEW')
      OPEN(UNIT=13,FILE='VERT3.INP',STATUS='NEW')
      OPEN(UNIT=14,FILE='VERT4.INP',STATUS='NEW')
      REWIND 11
      REWIND 12
      REWIND 13
      REWIND 14
C-----------------------------------------------------------------------*
C AT EVERY WELDING SPOT A NEV CYLINDRICAL COORDINATE SYSTEM IS DEFINED  *
C-----------------------------------------------------------------------*
      DO J=1,55
      XCS(2*J-1)=SL1+(J-1)*SL/2
      XCS(2*J)=XCS(2*J-1)
      ZCS(2*J-1)=(ST/2)*(1-(-1)**J)
      ZCS(2*J)=ZCS(2*J-1)+2*ST
      ENDDO
      DO J=1,100
      YCS(J)=0.
      ENDDO
```

```
      DO I=1,100
      PHI(I)=-90
      ENDDO
      JJ=4
      DO I=1,95
      IF(XCS(I).LE.(LX-SL1).AND.ZCS(I).LE.(LZ-ST1)) THEN
      JJ=JJ+1
      XC(JJ)=XCS(I)
      YC(JJ)=YCS(I)
      ZC(JJ)=ZCS(I)
      PH(JJ)=PHI(I)
      WRITE(12,*) 'LOCAL',JJ,' CYLI',XC(JJ),YC(JJ),ZC(JJ),0,PH(JJ),0
      ENDIF
      ENDDO
      WRITE(12,*) 'CSYS 1'
C-----------------------------------------------------------------------*
C VERTEX DEFINITION                                                     *
C-----------------------------------------------------------------------*
      DO K=0,1
      DO J=1,NVZ
      A=NVR*K+1+NVX*(J-1)
      B=NVR*K+NVX*J
      DO I=A,B
      NV=I
      XV=0+DX*(I-A)
      ZV=DZ*(J-1)
      FF=ST1*(SL1-XV)/SL1+3*ST
      FF1=ST1*(SL1+XV-LX)/SL1+3*ST
C-----------------------------------------------------------------------*
C FUNCTIONS FOR DESCRIBING OF THE THERMOPLATE SURFACE, EQUATION (5.1)    *
C-----------------------------------------------------------------------*
      F1=D*(1+COS(PI*ZV/ST)*COS(2*PI*(XV-SL1)/SL))/4
C FUNCTIONDEFINING THE FIRST EDGE
      F2=D*(4+COS(PI*ZV/ST)+(2-COS(PI*ZV/ST))*COS(PI*XV/SL1))
     **SIN(PI*XV/(2*SL1))/8
C FUNCTION DEFINING THE LAST EDGE
      F2A=D*(4+COS(PI*ZV/ST)+(2-COS(PI*ZV/ST))*COS(PI*(LX-XV)/SL1))
     **SIN(PI*(LX-XV)/(2*SL1))/8
C FUNCTION DEFINING THE RIGHT EDGE
      F3A=(1-COS(PI*(3*ST+ST1-ZV)/ST1))*COS(PI*(3*ST+ST1-ZV)/ST1)
     **COS(2*PI*(XV-SL1)/SL)
      F3B=-3*SIN(PI*(3*ST-5*ST1-ZV)/(2*ST1))
     *-SIN(3*PI*(3*ST-ST1-ZV)/(2*ST1))
      F3=D*(F3A+F3B)*(1-0.065*(1-COS(2*PI*(3*ST+ST1-ZV)/ST1)))/8
```

```
C FUNCTION DEFINING THE FIRST CORNER
      F41=(1-0.1*(1-(COS(4*PI*(3*ST+ST1-ZV)/ST1)))**0.4)
      F4=4*F2*F3/(1.22*D)*F41
C FUNCTION DEFINING THE LAST CORNER
      F4A=4*F2A*F3/(1.22*D)*F41
C FUNCTION DEFINING THE CONNECTING TUBES
      XM=2*SL1*ACOS(SqRT((COS(PI*ZV/ST)-1)/(COS(PI*ZV/ST)-2)))/PI
      XX=0.8*(XM-SL1)+SL1
      Y1A=R1
      Y1B=SqRT((2*R1)**2-(ZV-R2)**2)/2
      Y2=D*(4+COS(PI*ZV/ST)+(2-COS(PI*ZV/ST))*COS(PI*XX/SL1))
     **SIN(PI*XX/(2*SL1))/8
      FE1=XV*(Y2-Y1A)/XX+Y1A
      FE2=XV*(Y2-Y1B)/XX+Y1B
      FA1=(LX-XV)*(Y2-Y1A)/XX+Y1A
      FA2=(LX-XV)*(Y2-Y1B)/XX+Y1B
C-------------------------------------------------------------------------*
C THERMOPLATE REGIONS                                                     *
C-------------------------------------------------------------------------*
      IF((XV.GE.SL1).AND.(XV.LE.(LX-SL1))) THEN
      IF(ZV.LE.(3*ST)) THEN
      F=F1
      ENDIF
      ENDIF
      IF(XV.LT.SL1.AND.ZV.LT.(3*ST+ST1/2).AND.ZV.LT.FF) THEN
      F=F2
      IF(XV.LT.XX.AND.ZV.LE.R2) THEN
      IF(FE1.GT.F2)THEN
      F=FE1
      ENDIF
      ENDIF
      IF(XV.LT.XX.AND.ZV.GT.R2.AND.ZV.LE.(R2+2*R1)) THEN
      IF(FE2.GT.F2) THEN
      F=FE2
      ENDIF
      ENDIF
      ENDIF
      IF(XV.GT.(LX-SL1).AND.ZV.LT.(3*ST+ST1/2).AND.
     *ZV.LT.FF1) THEN
      F=F2A
      IF(XV.GT.(LX-XX).AND.ZV.LE.R2) THEN
      IF(FA1.GT.F2A)THEN
      F=FA1
      ENDIF
```

```
      ENDIF
      IF(XV.GT.(LX-XX).AND.ZV.GT.R2.AND.ZV.LE.(R2+2*R1)) THEN
      IF(FA2.GT.F2A) THEN
      F=FA2
      ENDIF
      ENDIF
      ENDIF
      IF(XV.GE.SL1/2.AND.XV.LE.(LX-SL1/2).AND.
     *ZV.GT.3*ST.AND.ZV.GE.FF.AND.ZV.GE.FF1) THEN
      F=F3
      ENDIF
      IF(XV.LT.SL1/2.AND.ZV.GE.(3*ST+ST1/2)) THEN
      F=F4
      ENDIF
      IF(XV.GT.(LX-SL1/2).AND.ZV.GE.(3*ST+ST1/2)) THEN
      F=F4A
      ENDIF
      YV=(2*K-1)*F
      F=0
      FF=0
      WRITE(11,*) 'V ',NV,' ',XV,' ',YV,' ',ZV
      ENDDO
      ENDDO
      ENDDO
C-----------------------------------------------------------------------*
C CELL DEFINITION                                                       *
C-----------------------------------------------------------------------*
      DO J=1,NVZ-1
      A=1+NVX*(J-1)
      B=NVX*J
      DO I=A,B-1
      N1=I
      N2=I+1
      N3=I+NVX+1
      N4=I+NVX
      N5=I+NVR
      N6=I+NVR+1
      N7=I+NVR+NVX+1
      N8=I+NVR+NVX
      WRITE(11,*) 'C ',N1,' ',N4,' ',N3,' ',N2,' ',N5,' ',N8,' ',N7,' ',N6
      ENDDO
      ENDDO
C-----------------------------------------------------------------------*
C CELLS TO BE REFINED IN X AND Z DIRECTION                              *
```

```
C-----------------------------------------------------------------------*
      WRITE(13,*) 'CSET ','NEWS ','GRAN ',-R3,R3,-365,365,-10,10,5
      DO I=6,JJ
      WRITE(13,*) 'CSET ','ADD ','GRAN ',-R3,R3,-365,365,-10,10,I
      ENDDO
      WRITE(13,*) 'CREFINE,2,2,1,CSET,0,0,MERG,NOCOUPLE'
      WRITE(13,*) 'CSET,NEWS,GRAN',-R4,R4,-365,365,-10,10,5
      DO I=6,JJ
      WRITE(13,*) 'CSET,ADD,GRAN',-R4,R4,-365,365,-10,10,I
      ENDDO
      WRITE(13,*) 'CREFINE,2,2,1,CSET,0,0,MERG,NOCOUPLE'
C-----------------------------------------------------------------------*
C CELLS TO BE DELETED                                                   *
C-----------------------------------------------------------------------*
      WRITE(13,*) 'CSET ','NEWS ','GRAN ',-R5,R5,-365,365,-10,10,5
      DO I=6,JJ
      WRITE(13,*) 'CSET ','ADD ','GRAN ',-R5,R5,-365,365,-10,10,I
      ENDDO
      WRITE(13,*) 'CDEL CSET'
      WRITE(13,*) 'CSET ALL'
      WRITE(13,*) 'CPLOT'
      WRITE(13,*) ' CSET ALL'
      WRITE(13,*) ' CPLOT'
C-----------------------------------------------------------------------*
C CELLS TO BE REFINED IN Y DIRECTION                                    *
C-----------------------------------------------------------------------*
      WRITE(13,*) ' CREFINE,1,1,10,CSET,0,0,MERG,NOCOUPLE'
      WRITE(13,*) ' CSET ALL'
      WRITE(13,*) ' CPLOT'
C-----------------------------------------------------------------------*
C COUPLES DEFINITION                                                    *
C-----------------------------------------------------------------------*
      DO I=1,20
      X1=-1+(I-1)*50
      X2=50+(I-1)*50
      IF(X1.LE.LX) THEN
      WRITE(13,*) ' CSET NEWS GRAN',X1,X2
      WRITE(13,*) ' CPCR CSET 1'
      ENDIF
      ENDDO
      WRITE(13,*) 'CSET ALL'
      WRITE(13,*) 'CPLOT'
C-----------------------------------------------------------------------*
C CELLS AT THE WALL TO BE REFINED                                       *
```

```
C-----------------------------------------------------------------------*
      WRITE(13,*) ' VSET ALL'
      WRITE(13,*) ' VSET SUBSET GRAN 0.001',
     *LX-0.001,' -50,50,0.001',LZ-0.001
      WRITE(13,*) ' VSET SUBSET SURFACE'
      WRITE(13,*) ' CSET NEWS VSET ANY'
      WRITE(13,*) 'CPLOT'
      WRITE(13,*) 'CREFINE,2,2,3,CSET,0,0,MERG,NOCOUPLE'
      WRITE(13,*) 'CSET ALL'
      WRITE(13,*) 'CPLOT'
      DO I=1,20
      X1=-1+(I-1)*50
      X2=50+(I-1)*50
      IF(X1.LE.LX) THEN
      WRITE(13,*) ' CSET NEWS GRAN',X1,X2
      WRITE(13,*) ' CPCR CSET 1'
      ENDIF
      ENDDO
      WRITE(13,*) 'CSET ALL'
      WRITE(13,*) 'CPLOT'
C-----------------------------------------------------------------------*
C BOUNDARY CONDITIONS                                                   *
C-----------------------------------------------------------------------*
      WRITE(14,*) ' RDEF,1,INLE $ $ $ $ $ $ $ $ $'
      WRITE(14,*) ' RNAM,1,INLET'
      WRITE(14,*) ' RDEF,2,OUTL $ $ $ $ $ $ $ $ $'
      WRITE(14,*) ' RNAM,2,OUTLET'
      WRITE(14,*) ' RDEF,3,WALL $ $ $ $ $ $ $ $ $'
      WRITE(14,*) ' RNAM,3,WALL'
      WRITE(14,*) ' RDEF,4,WALL $ $ $ $ $ $ $ $ $'
      WRITE(14,*) ' RNAM,4,WALL'
      WRITE(14,*) ' RDEF,5,SYMP $ $ $ $ $ $ $ $ $'
      WRITE(14,*) ' RNAM,5,SYMMETRY'
      WRITE(14,*) ' RDEF,6,SYMP $ $ $ $ $ $ $ $ $'
      WRITE(14,*) ' RNAM,6,SYMMETRY'
      WRITE(14,*) ' TEMP,ON'
      WRITE(14,*) ' RADI,OFF'
      WRITE(14,*) ' SOLAR,OFF'
      WRITE(14,*) ' CONJ,OFF'
      WRITE(14,*) ' ACCE,-1,0,0,1,0'
      WRITE(14,*) ' PMAT,1,FLUID,H2O_L,0'
      WRITE(14,*) ' DENS,CONSTANT,997.561'
      WRITE(14,*) ' LVIS,CONSTANT,0.000887'
      WRITE(14,*) ' SPEC,CONSTANT,4181.72'
```

```
      WRITE(14,*) ' COND, CONSTANT,0.620271'
      WRITE(14,*) ' MOLWT,18'
      WRITE(14,*) ' RELAX,0.7,0.3, ,0.95, ,1,1,1, , , , , ,'
      WRITE(14,*) ' SWEEP,10000,10000,10000,100000,,,100,,,'
      WRITE(14,*) ' RESID,0.1,0.1,0.1,0.05, , ,0.1, , , , ,'
      WRITE(14,*) ' WDATA,RESTART,10,0,STAR.PST'
      WRITE(14,*) ' PRFIELD,NONE,,,USER'
      WRITE(14,*) ' ITER',IT,TT
      WRITE(14,*) ' MEMORY MAXCEL 15000000'
      WRITE(14,*) ' MEMORY MAXVRT 15000000'
      WRITE(14,*) ' MEMORY MAXCUT 15000000'
      WRITE(14,*) ' CSET,ALL'
      WRITE(14,*) ' VSET,ALL'
      WRITE(14,*) ' VMER,VSET,,0.0001,,,,,,,LOW,DELETE,C'
      WRITE(14,*) ' VCOMPRESS,ALL $Y'
      WRITE(14,*) ' CCOMPRESS $Y'
      WRITE(14,*) ' CSET,ALL'
      WRITE(14,*) ' VSET,ALL'
      WRITE(14,*) ' CPLOT'
      WRITE(14,*) ' BSET ALL'
      WRITE(14,*) ' BDEL BSET'
      WRITE(14,*) ' RDEF,1,INLET,STANDARD'
      WRITE(14,*) UIN,0,0,1,0,TIN,RHOIN
      WRITE(14,*) ' RTURB,1,NONE'
      WRITE(14,*) ' RINLET,1,MASS,N'
      WRITE(14,*) ' RDEF,3,WALL,STANDARD'
      WRITE(14,*) ' NOSL,STAND,9,'
      WRITE(14,*) ' 0,0,0,1,0'
      WRITE(14,*) ' FIXED',TW1,0
      WRITE(14,*) ' RDEF,4,WALL,STANDARD'
      WRITE(14,*) ' NOSL,STAND,9,'
      WRITE(14,*) ' 0,0,0,1,0'
      WRITE(14,*) ' FIXED',TW2,0



C-----------------------------------------------------------------------*
C BOUNDARIES LOCATION                                                   *
C-----------------------------------------------------------------------*
C INLET
      WRITE(14,*) ' CSET,ALL'
      WRITE(14,*) ' CSET, NEWS, GRAN -2, 2,-10,10',-10,R2+2*R1+0.01
      WRITE(14,*) ' CPLOT'
```

```
      WRITE(14,*) ' ZOOM OFF $REPLOT'
      WRITE(14,*) ' VIEW,-1,0,0 $REPLOT'
      WRITE(14,*) ' BZON,1,,'
      WRITE(14,*) ' BSET ALL'
      WRITE(14,*) ' BSET SUBSET GRAN',-2*L,0.001
      WRITE(14,*) ' BSET INVERT'
      WRITE(14,*) ' BSET SUBSET REGION 1'
      WRITE(14,*) ' BDEL BSET'
C OUTLET
      WRITE(14,*) ' CSET NEWS GRAN',L-2,2*L,-10,10,-10,R2+2*R1+0.01
      WRITE(14,*) ' CPLOT'
      WRITE(14,*) ' VIEW,1,0,0,$REPLOT'
      WRITE(14,*) ' ZOOM OFF $REPLOT'
      WRITE(14,*) ' BZON,2,,'
      WRITE(14,*) ' BSET ALL'
      WRITE(14,*) ' BSET SUBSET GRAN',L-0.001,2*L
      WRITE(14,*) ' BSET INVERT'
      WRITE(14,*) ' BSET SUBSET REGION 2'
      WRITE(14,*) ' BDEL BSET'
C SYMPLANE LEFT
      WRITE(14,*) ' CSET ALL'
      WRITE(14,*) ' CSET NEWS GRAN',-2*L,2*L,-50,50,-50,2
      WRITE(14,*) ' CPLOT'
      WRITE(14,*) ' VIEW,0,0,-1'
      WRITE(14,*) ' ZOOM OFF $REPLOT'
      WRITE(14,*) ' BZON,5,,'
      WRITE(14,*) ' BSET ALL'
      WRITE(14,*) ' BSET SUBSET GRAN',-2*L,2*L,-50,50,-50,0.001
      WRITE(14,*) ' BSET INVERT'
      WRITE(14,*) ' BSET,SUBSET, REGION, 5'
      WRITE(14,*) ' BDEL BSET'
C SYMPLANE RIGHT
      WRITE(14,*) ' CSET ALL'
      WRITE(14,*) ' CSET NEWS GRAN',-2*L,2*L,-50,50,ST-2,2*LZ
      WRITE(14,*) ' CPLOT'
      WRITE(14,*) ' VIEW,0,0,1'
      WRITE(14,*) ' ZOOM OFF $REPLOT'
      WRITE(14,*) ' BZON,6,,'
      WRITE(14,*) ' BSET ALL'
      WRITE(14,*) ' BSET SUBSET GRAN',-2*L,2*L,-50,50,LZ-0.001,2*LZ
      WRITE(14,*) ' BSET INVERT'
      WRITE(14,*) ' BSET,SUBSET, REGION, 6'
      WRITE(14,*) ' BDEL BSET'
C LOWER WALL W1
```

```
      WRITE(14,*) ' CSET ALL'
      WRITE(14,*) ' ZOOM OFF'
      WRITE(14,*) ' CPLOT'
      WRITE(14,*) ' VIEW,0,-1,0,$REPLOT'
      WRITE(14,*) ' BZON,3,,'
      WRITE(14,*) ' BSET ALL'
      WRITE(14,*) ' BSET NEWS GRAN',-2*LX,0.001
      WRITE(14,*) ' BSET ADD GRAN', LX-0.001,2*LX
      WRITE(14,*) ' BSET ADD GRAN', -2*LX,2*LX,-50,50,-LZ,0.001
      WRITE(14,*) ' BSET ADD GRAN', -2*LX,2*LX,-50,50,LZ-0.001,2*LZ
      WRITE(14,*) ' BSET SUBSET REGION 3'
      WRITE(14,*) ' BDEL BSET'
      DO I=5,JJ
      WRITE(14,*) ' VSET NEWS GRAN',-R-0.001,R+0.001,-365,365,-50,50,I
      WRITE(14,*) ' BSET ADD VSET ALL'
      ENDDO
      WRITE(14,*) 'BMOD,BSET,7'
C UPPER WALL W2
      WRITE(14,*) ' CSET ALL'
      WRITE(14,*) ' VIEW,0,1,0,$REPLOT'
      WRITE(14,*) ' BZON,4,,'
      WRITE(14,*) ' BSET ALL'
      WRITE(14,*) ' BSET NEWS GRAN',-2*LX,0.001
      WRITE(14,*) ' BSET ADD GRAN', LX-0.001,2*LX
      WRITE(14,*) ' BSET ADD GRAN', -2*LX,2*LX,-50,50,-LZ,0.001
      WRITE(14,*) ' BSET ADD GRAN', -2*LX,2*LX,-50,50,LZ-0.001,2*LZ
      WRITE(14,*) ' BSET SUBSET REGION 4'
      WRITE(14,*) ' BDEL BSET'
      CLOSE(11)
      CLOSE(12)
      CLOSE(13)
      CLOSE(14)
      END
```

C POSDAT.f

```
C***********************************************************************
      SUBROUTINE POSDAT(KEY,VOL,U,TE,ED,T,P,VIST,DEN,CP,VISM,CON,
     *  F,ICLMAP,ICTID,RESOR,VF,FORCB,IRN,PREFM,LEVEL)
C     POSDAT.f is a StarCD post-processing procedure
C***********************************************************************
C-----------------------------------------------------------------------*
C     STAR VERSION 3.24.000                                             *
C-----------------------------------------------------------------------*
      INCLUDE 'comdb.inc'
      COMMON/USR001/INTFLG(100)
       DIMENSION KEY(-NBMAXU:NCTMXU),VOL(NCTMXU),U(3,-NBMAXU:NCMAXU),
     * TE(-NBMAXU:NCMAXU),ED(-NBMAXU:NCMAXU),T(-NBMAXU:NCTMXU,1+NSCU),
     * P(-NBMAXU:NCMAXU),VIST(-NBMAXU:NCMAXU),DEN(-NBMAXU:NCTMXU),
     * CP(-NBMAXU:NCTMXU),VISM(-NBMXVU:NCMXVU),CON(-NBMXCU:NCMXCU),
     * F(3,-NBMAXU:NCMAXU),ICLMAP(NCTMXU),ICTID(NCTMXU),
     * RESOR(89,-100:100),VF(NCDMXU),FORCB(3,NWLMX),IRN(NWLMX)
C-----------------------------------------------------------------------*
C     VARIABLES DEFINITION                                              *
C-----------------------------------------------------------------------*
      DOUBLE PRECISION P1,P2,P3,P4,P5,P6,P7,P8,PIN,PTIN,PT
      DOUBLE PRECISION T1,T2,T3,T4,T5,TT
      DOUBLE PRECISION TW1,TW2,TWQ1,TWQ2,AREA1,AREA2
      DOUBLE PRECISION HF1,HF2,HFQ1,HFQ2
      DOUBLE PRECISION HF11,HF21,HFQ11,HFQ21
      DOUBLE PRECISION HCF1,HCF2,HCFQ1,HCFQ2
      DOUBLE PRECISION HCFQ11,HCFQ21
      DOUBLE PRECISION TM1(2000,12),TM2(2000,14)
      DOUBLE PRECISION A1,A2
      DOUBLE PRECISION X,DX,G61,G62,G71,G72,G8,VV
      DOUBLE PRECISION G5A,G5B
      DOUBLE PRECISION Z,DZ,Z0,Z1,XMAX,AA,BB,A,B
      INTEGER L,NPP,WR1,WR2,IMAX,IMAX1,N,N1,NPP1
      INTEGER L1(5000)
      INCLUDE 'usrdat.inc'
C DX is the cell size in X direction in mm
      PARAMETER(DX=0.0005)
```

```
C Residual tolerance
      PARAMETER(TT=1.E-4)
C Number of the cross sections, steps in x direction
      PARAMETER(NPP=1008)
C-----------------------------------------------------------------------*
C     ADDITIONAL COMMON BLOCKS                                          *
C-----------------------------------------------------------------------*
      POINTER(P_IRTYP,IRTYP(0:NREGMX))
      COMMON/C06004/P_IRTYP
      POINTER(P_LX,LX(4))
      COMMON /C06013/P_LX
      POINTER(P_INDWL,INDWL(4))
      COMMON/C06014/P_INDWL
      POINTER(P_IBLMAP,IBLMAP(NBMAX))
      COMMON/C1C003/P_IBLMAP
      POINTER(P_IDC,IDC(4))
      COMMON/C33001/P_IDC
      POINTER(P_DRM,DRM(4))
      COMMON/C33004/P_DRM
      POINTER(P_LQ,LQ(6,NCTMAX))
      COMMON /DCO5/P_LQ
      POINTER(P_S,S(3,3,-NBMAX:NCTMAX))
      COMMON /DCO14/P_S
      POINTER(P_CX,CX(3,-NBMAX:NCTMAX))
      COMMON/DCO21/P_CX
      POINTER(P_HCB,HCB(NWSMX,1+NSC))
      POINTER(P_HFB,HFB(NWSMX,1+NSC))
      COMMON /DCO19A/P_HCB
      COMMON /DCO19B/P_HFB
      POINTER(P_SB,SB(3,NBN1MX:NCUTMX+1))
      COMMON/DCO31R2/P_SB
      COMMON /DROP1A/ NDR
      COMMON /DROP3/  TWPHL
      COMMON /INDMP1/ NDIR(-3:3),NDINAB(6)
      COMMON /INDMP2/ NDIN(6)
      COMMON /MPP430/ MASTER,SLAVE,HPCRUN,PARRUN
      COMMON /MPP1/ NOPROC,MYID
      COMMON /SLIPW/  NWSBT
      LOGICAL MASTER,SLAVE,HPCRUN,PARRUN,TWPHL
C-----------------------------------------------------------------------*
C     OUTPUT FILES DEFINITION                                           *
C-----------------------------------------------------------------------*
      IF(INTFLG(1).EQ.0) THEN
      OPEN(85,file='../results1.dat')
```

```
      OPEN(86,file='../results2.dat')
      INTFLG(1) = 1
      ENDIF
C-------------------------------------------------------------------------*
C     THE EVALUATION TAKE PLACE AT AFTER THE LAST ITERATION            *
C-------------------------------------------------------------------------*
      IF(LEVEL.EQ.2) THEN
      IMAX=ITERS+ITSTEP-1
      IF((RESOR(1,1).LT.TT.AND.RESOR(2,1).LT.TT.AND.
     *RESOR(3,1).LT.TT.AND.RESOR(4,1).LT.TT.AND.
     *RESOR(5,1).LT.TT.AND.RESOR(6,1).LT.TT).OR.
     *(ITER.EQ.IMAX)) THEN
C-------------------------------------------------------------------------*
C     INITIALIZING                                                        *
C-------------------------------------------------------------------------*
      T1=0.
      T2=0.
      T3=0.
      T4=0.
      T5=0.
      P1=0.
      P2=0.
      P3=0.
      P4=0.
      P5=0.
      P6=0.
      P7=0.
      PI=0.
      PT=0.
      PIN=0.
      PTIN=0.
      A=0.
      B=DX
      X=DX*1000/2
      HF1=0.
      HF2=0.
      HF11=0.
      HF21=0.
      HFQ1=0.
      HFQ2=0.
      HFQ11=0.
      HFQ21=0.
      HCF1=0.
      HCF2=0.
```

```
      HCFQ1=0.
      HCFQ2=0.
      HCFQ11=0.
      HCFQ21=0.
      POV1=0.
      POV2=0.
      POVQ1=0.
      POVQ2=0.
      DO 100 K=1,NPP
      DO 110 J=1,6
      TM(K,J)=0.
110   CONTINUE
100   CONTINUE
C-------------------------------------------------------------------------*
C     THE EVALUATION TAKES PLACE AT EACH STEP X                           *
C-------------------------------------------------------------------------*
      DO 200 K=1,NPP
        X=DX/2+(K-1)*DX
        A=(K-1)*DX
        B=K*DX
C-------------------------------------------------------------------------*
C     VARIABLES EVALUATED AT CELL CENTRES                                 *
C-------------------------------------------------------------------------*
      DO 210 I=1,NCELL
        IF(CX(1,I).GE.A) THEN
        IF(CX(1,I).LE.B) THEN
C VV is the velocity magnitude for the cell I
        VV=SQRT(U(1,I)**2+U(2,I)**2+U(3,I)**2)
C is the total pressure for the cell I
        PT=P(I)+DEN(I)*(VV**2)/2
C T1 is the volume integral rho*cp*u*T*dV
        T1=T1+DEN(I)*CP(I)*U(1,I)*T(I,1)*VOL(I)
C T2 is the volume integral ro*cp*u*dV
        T2=T2+DEN(I)*CP(I)*U(1,I)*VOL(I)
C T3 is the volume integral u*dV, volume flow rate*dx
        T3=T3+U(1,I)*VOL(I)
C T4 is rho*u*dV, mass flow rate*dx
        T4=T4+U(1,I)*DEN(I)*VOL(I)
C P1 is the volume integral p*dV
        P1=P1+P(I)*VOL(I)
C P2 is the volume integral PT*dV
        P2=P2+PT*VOL(I)
c P3 is the cross-section area
        P3=P3+VOL(I)
```

```
C P4 is the mean density*dV
        P4=P4+DEN(I)*VOL(I)
        ENDIF
        ENDIF
210   CONTINUE
C-------------------------------------------------------------------------*
C     VARIABLES EVALUATED AT WALL BOUNDARIES, THERMOPLATE SURFACE        *
C-------------------------------------------------------------------------*
      DO 220 J=1,NWSBT
        IB=INDWL(J)
        IC=LX(IB)/7
        IP=ICLMAP(IC)
        INDX=MOD(LX(IB),7)
        IBG=LQ(INDX,IC)
        IBP=IBLMAP(-IBG)
        IREG=IRN(IB)
        IBTYP=IRTYP(IREG)
        IF(CX(1,IBG).GE.A.AND.CX(1,IBG).LE.B) THEN
        IF(ABS(HFB(IB,1)).GT.0.000001) THEN
C-------------------------------------------------------------------------*
C     LOWER WALL, W1                                                      *
C-------------------------------------------------------------------------*
        IF(CX(2,IBG).LT.0) THEN
        A1=SQRT((S(3,1,IC))**2+(S(3,2,IC))**2+(S(3,3,IC))**2)
C HF is the heat flux*surface, A<X<B
        HF1=HF1+HFB(IB,1)*A1
C HFQ is the mean heat flux*surface
        HFQ1=HFQ1+HFB(IB,1)*A1
        TWQ1=TWQ1+T(IBG,1)*A1
C POV is the wall surface A<x<B
        POV1=POV1+A1
C POVQ is the wall surface 0<x<B
        POVQ1=POVQ1+A1
        ENDIF
C-------------------------------------------------------------------------*
C     UPPER WALL, W2                                                      *
C-------------------------------------------------------------------------*
        IF(CX(2,IBG).GT.0) THEN
        A2=SQRT((S(3,1,IC))**2+(S(3,2,IC))**2+(S(3,3,IC))**2)
C HF is the heat flux*surface, A<X<B
        HF2=HF2+HFB(IB,1)*A2
C HFQ is the mean heat flux*surface
        HFQ2=HFQ2+HFB(IB,1)*A2
        TWQ2=TWQ2+T(IBG,1)*A2
```

```
C POV is the wall surface A<x<B
        POV2=POV2+A2
C POVQ is the wall surface 0<x<B
        POVQ1=POVQ1+A1
        ENDIF
        ENDIF
        ENDIF
220   CONTINUE
      T5=T1/T2
      HF11=HF1/POV1
      HF21=HF2/POV2
      HFQ11=HFQ1/POVQ1
      HFQ21=HFQ2/POVQ2
      HCF1=HF11/(TW1-T5)
      HCF2=HF21/(TW2-T5)
C-------------------------------------------------------------------------*
C    Introduced for parallel computing (this was needed for StarCD       *
C    version 3.24)                                                       *
         if (nhpc.gt.1) then                                             *
           t1_sum    = dgsum(t1)                                         *
           t2_sum    = dgsum(t2)                                         *
           t3_sum    = dgsum(t3)                                         *
           t4_sum    = dgsum(t4)                                         *
           p1_sum    = dgsum(p1)                                         *
           p2_sum    = dgsum(p2)                                         *
           p3_sum    = dgsum(p3)                                         *
           p4_sum    = dgsum(p4)                                         *
           hf1_sum   = dgsum(hf1)                                        *
           hf2_sum   = dgsum(hf2)                                        *
           hfq1_sum  = dgsum(hfq1)                                       *
           hfq2_sum  = dgsum(hfq2)                                       *
           pov1_sum  = dgsum(pov1)                                       *
           pov2_sum  = dgsum(pov2)                                       *
           povq1_sum = dgsum(povq1)                                      *
           povq2_sum = dgsum(povq2)                                      *
           twq1_sum  = dgsum(twq1)                                       *
           twq2_sum  = dgsum(twq2)                                       *
           if (ihpc.ge.1) then                                           *
               t3    = t3_sum/dx                                         *
               t4    = t4_sum/dx                                         *
               t5    = t1_sum/t2_sum                                     *
               p5    = p1_sum/p3_sum                                     *
               p6    = p2_sum/p3_sum                                     *
               p7    = p4_sum/p3_sum                                     *
```

```
              hf11  = hf1_sum/pov1_sum                                    *
              hf21  = hf2_sum/pov2_sum                                    *
              hfq11 = hfq1_sum/povq1_sum                                  *
              hfq21 = hfq2_sum/povq2_sum                                  *
              tw1   = twq1_sum/pov1_sum                                   *
              tw2   = twq2_sum/pov2_sum                                   *
              hcf1  = hf11/(tw1-t5)                                       *
              hcf2  = hf21/(tw2-t5)                                       *
              hcfq1 = hcfq1+hcf1*dx                                       *
              hcfq2 = hcfq2+hcf2*dx                                       *
              hcfq11= hcfq1/b                                             *
              hcfq21= hcfq2/b                                             *
              IF(K.EQ.1) THEN                                             *
              pin   = p1_sum/p3_sum                                       *
              ptin  = p2_sum/p3_sum                                       *
              ENDIF                                                       *
              g5a   = t3*(pin-p5)/dx                                      *
              g5b   = t3*(ptin-p6)/dx                                     *
              g61   = hfq1_sum                                            *
              g62   = hfq2_sum                                            *
              g71   = povq1_sum                                           *
              g72   = povq2_sum                                           *
              p8    = p8+p3_sum                                           *
          endif                                                           *
          endif                                                           *
C ----- Introduced for parallel computing                                 *
C-----------------------------------------------------------------------*
      TM1(K,1)=X*1000
      TM1(K,2)=HF11
      TM1(K,3)=HF21
      TM1(K,4)=HFQ11
      TM1(K,5)=HFQ21
      TM1(K,6)=HCF1
      TM1(K,7)=HCF2
      TM1(K,8)=HCFQ11
      TM1(K,9)=HCFQ21
      TM1(K,10)=T5
      TM1(K,11)=TW1
      TM1(K,12)=TW2
      TM2(K,1)=X*1000
      TM2(K,2)=P5
      TM2(K,3)=P6
      TM2(K,4)=T3
      TM2(K,5)=T4
```

```
      TM2(K,6)=G61
      TM2(K,7)=G62
      TM2(K,8)=G71
      TM2(K,9)=G72
      TM2(K,10)=P8
      TM2(K,11)=G5A
      TM2(K,12)=G5B
      TM2(K,13)=(G61+G62)/G5A
      TM2(K,14)=(G61+G62)/G5B
C-----------------------------------------------------------------------*
C     Data are written out at each step x                               *
C-----------------------------------------------------------------------*
      IF(K.eq.1) THEN
      WRITE(85,*)' x q1 q2 qm1 qm2 h1 h2 hm1 hm2 tb tw1 tw2'
      WRITE(86,*)' x pm ptm VS MSv Q1 Q2 S1 S2 V P Pt Q/P Q/Pt'
      ENDIF
      WRITE(85,*) (TM1(K,J),J=1,12)
      WRITE(86,*) (TM2(K,J),J=1,14)
C-----------------------------------------------------------------------*
C     Some values have to be restored                                   *
C-----------------------------------------------------------------------*
      T1=0.
      T2=0.
      T3=0.
      T4=0.
      T5=0.
      P1=0.
      P2=0.
      P3=0.
      P4=0.
      P5=0.
      P6=0.
      P7=0.
      PI=0.
      PT=0.
      HF1=0.
      HF2=0.
      HF11=0.
      HF21=0.
      HCF1=0.
      HCF2=0.
      HCF11=0.
      HCF21=0.
      POV1=0.
```

```
      POV2=0.
      TW1=0.
      TW2=0.
      TWQ1=0.
      TWQ2=0.
      t1_sum   = 0
      t2_sum   = 0
      t3_sum   = 0
      t4_sum   = 0
      p1_sum   = 0
      p2_sum   = 0
      p3_sum   = 0
      p4_sum   = 0
      hf1_sum  = 0
      hf2_sum  = 0
      pov1_sum = 0
      pov2_sum = 0
      twq1_sum = 0
      twq2_sum = 0
200   CONTINUE
      ENDIF
      ENDIF
      RETURN
      END
```

D Mesh Test and Other Numerical Details

The complex geometry of the flow channel contains several areas with large gradients of interesting quantities, which requires careful spatial resolutions. This is particularly the case near the walls and in the separation and reattachment regions of the recirculation zones. This demands for an appropriate and expensive discretisation of the computational domain.

To test the discretisation effect on heat transfer, a relatively coarse grid with equal number of points in the y-direction at each x, z-position have been used, Figure 4.1, and subsequently refined by increasing the number of grid points locally, or in the whole domain. Figure D.1 illustrates the case of a grid refinement in the wall region. Figure D.2 shows the effect of grid refinement on the heat transfer coefficient for a larger Reynolds number. For smaller Reynolds numbers, the deviations were still observed, but they were considerable smaller. The curve a) in Figure D.2 lies considerably below the other ones. This is due chiefly to the coarseness of the grid, which results in relatively large errors, particularly in the wall region. The scatter of the curves b) to c) is much smaller and is rooted, on one side, in the physical uncertainty due to the grid size and in the numerical residua, on the other side. The reduction of the physical uncertainty by a refinement of the grid is expected to result in a correspondingly larger error due to the numerical residua, and an optimum regarding the reliability of the numerical results is expected when these uncertainties are the same, or at least of the same order of magnitude. A criterion for and objective judgement of the resulting uncertainty can scarcely be formulated. For this reason, and with regard to the flood of the data to be processed, the discretisation a) has been adopted in the numerical simulations.

The algorithm used was SIMPLE, a scalar solver type and conjugate gradient method (see e.g. StarCD Methodology Handbook [7] and Versteeg and Malalasekera [68]), at a maximal residual tolerance $\lambda = 10^{-4}$.

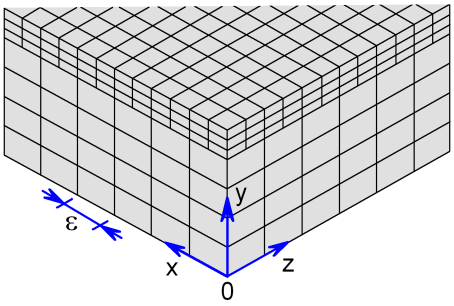

Figure D.1: Illustration of the grid used in the numerical simulations.

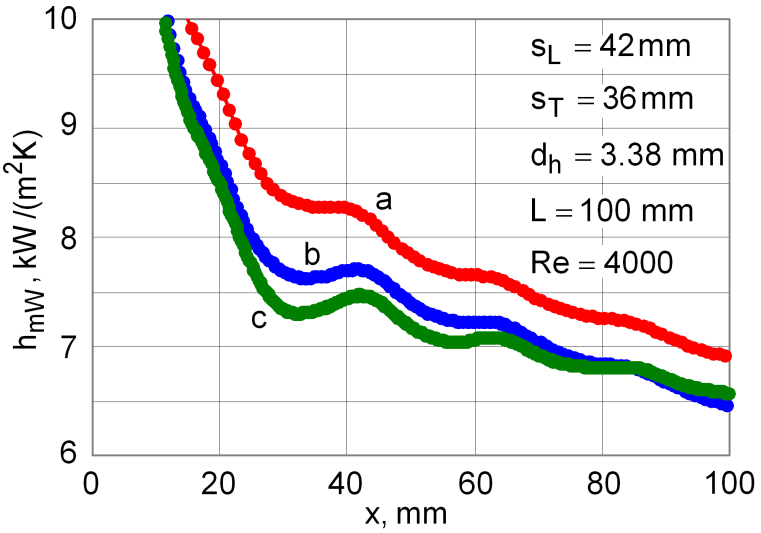

Figure D.2: Effect of mesh size on the numerical results: a) equidistant mesh, refined at wall (actually used, Figure D.1), b) like a), but the number of cells doubled in all three directions, c) like b), but the number of cells doubled in all three directions.

E Constants

Table E.1: Constants used in Equation (5.3) with $I = J = K = L = 2$ and $M = m = 0$.

$c_{0,0,0,0,0}$	-371.939	$c_{1,0,0,0,0}$	4779.99	$c_{2,0,0,0,0}$	-14562.2
$c_{0,0,0,1,0}$	2.7805	$c_{1,0,0,1,0}$	-32.5245	$c_{2,0,0,1,0}$	90.3223
$c_{0,0,0,2,0}$	-0.001084	$c_{1,0,0,2,0}$	0.0129844	$c_{2,0,0,2,0}$	-0.03698
$c_{0,0,1,0,0}$	51611.7	$c_{1,0,1,0,0}$	-645786	$c_{2,0,1,0,0}$	$2.018 \cdot 10^6$
$c_{0,0,1,1,0}$	-552.129	$c_{1,0,1,1,0}$	6433.27	$c_{2,0,1,1,0}$	-17765.4
$c_{0,0,1,2,0}$	0.22232	$c_{1,0,1,2,0}$	-2.65846	$c_{2,0,1,2,0}$	7.55836
$c_{0,0,2,0,0}$	$-1.316 \cdot 10^6$	$c_{1,0,2,0,0}$	$2.017 \cdot 10^7$	$c_{2,0,2,0,0}$	$-7.1599 \cdot 10^7$
$c_{0,0,2,1,0}$	25898.1	$c_{1,0,2,1,0}$	-305430	$c_{2,0,2,1,0}$	850628
$c_{0,0,2,2,0}$	-10.026	$c_{1,0,2,2,0}$	120.587	$c_{2,0,2,2,0}$	-343.563
$c_{0,1,0,0,0}$	12213.6	$c_{1,1,0,0,0}$	-161076	$c_{2,1,0,0,0}$	512002
$c_{0,1,0,1,0}$	-99.9053	$c_{1,1,0,1,0}$	1181.18	$c_{2,1,0,1,0}$	-3304.62
$c_{0,1,0,2,0}$	0.03971	$c_{1,1,0,2,0}$	-0.480533	$c_{2,1,0,2,0}$	1.37835
$c_{0,1,1,0,0}$	$-1.79387 \cdot 10^6$	$c_{1,1,1,0,0}$	$2.385 \cdot 10^7$	$c_{2,1,1,0,0}$	$-7.84 \cdot 10^7$
$c_{0,1,1,1,0}$	20357.9	$c_{1,1,1,1,0}$	-239478	$c_{2,1,1,1,0}$	666282
$c_{0,1,1,2,0}$	-8.23688	$c_{1,1,1,2,0}$	99.6535	$c_{2,1,1,2,0}$	-285.594
$c_{0,1,2,0,0}$	$5.80779 \cdot 10^7$	$c_{1,1,2,0,0}$	$-9.229 \cdot 10^8$	$c_{2,1,2,0,0}$	$3.326 \cdot 10^9$
$c_{0,1,2,1,0}$	-963007	$c_{1,1,2,1,0}$	$1.151 \cdot 10^7$	$c_{2,1,2,1,0}$	$-3.234 \cdot 10^7$
$c_{0,1,2,2,0}$	372.797	$c_{1,1,2,2,0}$	-4543.44	$c_{2,1,2,2,0}$	13053.7
$c_{0,2,0,0,0}$	-121519	$c_{1,2,0,0,0}$	$1.675 \cdot 10^6$	$c_{2,2,0,0,0}$	$-5.502 \cdot 10^6$
$c_{0,2,0,1,0}$	891.516	$c_{1,2,0,1,0}$	-10735.7	$c_{2,2,0,1,0}$	30432.7
$c_{0,2,0,2,0}$	-0.35433	$c_{1,2,0,2,0}$	4.35689	$c_{2,2,0,2,0}$	-12.6416
$c_{0,2,1,0,0}$	$2.0514 \cdot 10^7$	$c_{1,2,1,0,0}$	$-2.898 \cdot 10^8$	$c_{2,2,1,0,0}$	$9.797 \cdot 10^8$
$c_{0,2,1,1,0}$	-185038	$c_{1,2,1,1,0}$	$2.223 \cdot 10^6$	$c_{2,2,1,1,0}$	$-6.279 \cdot 10^6$
$c_{0,2,1,2,0}$	74.1139	$c_{1,2,1,2,0}$	-912.556	$c_{2,2,1,2,0}$	2647.22
$c_{0,2,2,0,0}$	$-7.988 \cdot 10^8$	$c_{1,2,2,0,0}$	$1.27 \cdot 10^{10}$	$c_{2,2,2,0,0}$	$-4.527 \cdot 10^{10}$
$c_{0,2,2,1,0}$	$8.7854 \cdot 10^6$	$c_{1,2,2,1,0}$	$-1.072 \cdot 10^8$	$c_{2,2,2,1,0}$	$3.0568 \cdot 10^8$
$c_{0,2,2,2,0}$	-3358.9	$c_{1,2,2,2,0}$	41659.2	$c_{2,2,2,2,0}$	-121107

F Numerical Results

Table F.1: Simulation results for model parameters given in Tables 4.1 and 4.2.

s_L [mm]	s_T [mm]	δ [mm]	Re [-]	Nu [-]	Δp [Pa]	s_L [mm]	s_T [mm]	δ [mm]	L [mm]	Nu [-]	Δp [Pa]
28	36	3.4	50	4.45	67.4	63	25	4.2	500	10.53	258.6
28	36	3.4	200	5.58	335.8	63	25	4.2	1000	18.36	897.
28	36	3.4	500	8.95	1038.4	63	25	4.2	2000	30.53	2887.6
28	36	3.4	750	11.46	1797.0	63	25	4.2	3000	39.20	6200.7
28	36	3.4	1000	13.88	2755.4	63	25	6.3	50	5.78	4.4
28	36	3.4	1500	17.91	4961.2	63	25	6.3	500	14.03	102.8
28	36	3.4	2000	21.68	7725.4	63	25	6.3	1000	24.66	340.4
28	36	3.4	2500	25.49	10985.4	63	25	6.3	2000	38.48	1163.7
28	36	3.4	3000	29.27	14867.3	63	25	6.3	3000	49.16	2603.8
28	36	3.4	3500	32.66	19176.7	63	25	8.4	50	6.34	2.0
28	36	3.4	3800	36.23	22488.9	63	25	8.4	500	17.72	54.1
28	36	3.4	4000	36.76	24154.3	63	25	8.4	1000	29.14	176.0
35	30	3.4	50	4.96	49.7	63	25	8.4	2000	45.21	645.6
35	30	3.4	1000	15.95	2528.6	63	25	8.4	3000	57.35	1420.9
35	30	3.4	2000	34.67	2228.3	63	30	4.2	50	5.05	15.9
35	30	6.3	50	5.18	9.3	63	30	4.2	500	9.80	331.9
35	30	6.3	1000	24.11	557.3	63	30	4.2	1000	18.31	1100.9
35	30	6.3	2000	37.70	1679.4	63	30	4.2	2000	29.39	3965.3
35	35	3.4	50	4.42	55.1	63	30	4.2	3000	35.56	7796.5
35	35	3.4	1000	14.29	2495.3	63	30	6.3	50	5.58	5.0
35	35	3.4	2000	21.84	6940.1	63	30	6.3	500	14.08	128.6
35	35	6.3	50	4.71	10.2	63	30	6.3	1000	24.81	471.3
35	35	6.3	1000	21.36	534.3	63	30	6.3	2000	36.09	1559.1
35	35	6.3	2000	33.41	1587.4	63	30	6.3	3000	45.17	3189.1
35	36	3.4	50	4.18	57.2	63	30	8.4	50	6.07	2.2
35	36	3.4	200	5.33	295.9	63	30	8.4	500	18.30	69.0
35	36	3.4	500	9.24	970.9	63	30	8.4	1000	29.0	245.2
35	36	3.4	750	11.84	1683.3	63	30	8.4	2000	42.26	818.8
35	36	3.4	1000	14.34	2543.3	63	30	8.4	3000	52.20	1675.9
35	36	3.4	1500	18.63	4688.7	63	35	4.2	50	4.88	17.8
35	36	3.4	2000	21.98	7195.4	63	35	4.2	500	9.61	383.1
35	36	3.4	2500	25.69	10057.5	63	35	4.2	1000	16.99	1187.2
35	36	3.4	3000	28.40	13367.5	63	35	4.2	2000	26.34	3817.6
35	36	3.4	3500	31.39	17135.9	63	35	4.2	3000	32.06	7319.6
35	36	3.4	3800	33.71	18963.0	63	35	6.3	50	5.33	5.6
35	36	3.4	4000	34.00	21510.6	63	35	6.3	500	13.49	145.2

s_L [mm]	s_T [mm]	δ [mm]	Re [-]	Nu [-]	Δp [Pa]	s_L [mm]	s_T [mm]	δ [mm]	L [mm]	Nu [-]	Δp [Pa]
35	40	3.4	50	4.16	59.3	63	35	6.3	1000	22.85	474.2
35	40	3.4	1000	12.76	2467.6	63	35	6.3	2000	32.69	1475.4
35	40	3.4	2000	19.56	6281.6	63	35	6.3	3000	40.26	2832.0
35	40	6.3	50	4.38	10.6	63	35	8.4	50	5.76	2.5
35	40	6.3	1000	18.97	521.9	63	35	8.4	500	17.38	75.2
35	40	6.3	2000	29.91	1546.9	63	35	8.4	1000	26.95	245.2
40	30	3.4	50	2.74	28.8	63	35	8.4	2000	38.92	764.3
40	30	3.4	1000	6.23	1398.9	63	35	8.4	3000	48.32	1488.5
40	30	3.4	2000	7.52	4009.6	63	36	3.4	50	4.61	34.0
40	30	6.3	50	5.40	8.1	63	36	3.4	100	5.14	73.9
40	30	6.3	1000	24.01	544.2	63	36	3.4	200	6.29	184.1
40	30	6.3	2000	37.17	1644.2	63	36	3.4	300	6.97	371.5
40	35	3.4	50	4.57	48.8	63	36	3.4	400	7.67	519.7
40	35	3.4	1000	14.45	2433.7	63	36	3.4	500	8.43	729.4
40	35	3.4	2000	21.96	6795.9	63	36	3.4	750	11.82	1314.4
40	35	6.3	50	4.91	9.0	63	36	3.4	1000	14.29	2016.0
40	35	6.3	1000	21.47	523.2	63	36	3.4	1500	19.19	3873.3
40	35	6.3	2000	33.31	1550.5	63	36	3.4	2000	23.29	6219.0
40	40	3.4	50	4.31	53.4	63	36	3.4	2500	26.55	8902.7
40	40	3.4	1000	13.06	2409.2	63	36	3.4	3000	29.22	11867.2
40	40	3.4	2000	19.84	6667.7	63	36	3.4	3500	31.68	15203.2
40	40	6.3	50	4.54	9.7	63	36	3.4	3800	33.19	17381.8
40	40	6.3	1000	19.32	510.7	63	36	3.4	4000	34.03	18808.0
40	40	6.3	2000	29.98	1500.8	70	25	4.2	50	5.06	13.0
42	20	3.4	50	5.40	30.7	70	25	4.2	500	10.89	214.9
42	20	3.4	200	8.03	172.0	70	25	4.2	1000	15.9	675.8
42	20	3.4	500	12.02	699.3	70	25	4.2	2000	28.85	2049.3
42	20	3.4	750	17.60	1564.1	70	25	4.2	3000	37.42	4059.3
42	20	3.4	1000	21.95	2672.5	70	25	6.3	50	5.61	4.1
42	20	3.4	1500	29.41	5577.7	70	25	6.3	500	12.59	77.7
42	20	3.4	2000	35.45	9617.3	70	25	6.3	1000	22.25	258.4
42	20	3.4	2500	38.86	13485.5	70	25	6.3	2000	36.62	800.1
42	20	3.4	3000	42.25	18045.5	70	25	6.3	3000	47.14	1715.6
42	20	3.4	3500	46.17	23505.6	70	25	8.4	50	6.13	1.8
42	20	3.4	4000	49.13	29796.0	70	25	8.4	500	15.95	41.5
42	25	3.4	50	5.08	35.9	70	25	8.4	1000	27.12	129.4
42	25	3.4	200	7.03	223.4	70	25	8.4	2000	42.66	421.6
42	25	3.4	500	11.66	827.9	70	25	8.4	3000	54.33	895.8
42	25	3.4	750	15.59	1551.17	70	30	4.2	50	4.94	14.5
42	25	3.4	1000	19.38	2498.1	70	30	4.2	500	9.55	274.1
42	25	3.4	1500	23.55	4661.7	70	30	4.2	1000	16.58	896.6
42	25	3.4	2000	28.12	7377.0	70	30	4.2	2000	30.29	3195.0
42	25	3.4	2500	33.45	11008.2	70	30	4.2	3000	36.85	6574.6
42	25	3.4	3000	35.72	14256.4	70	30	6.3	50	5.44	4.5
42	25	3.4	3500	39.12	18622.0	70	30	6.3	500	12.77	105.6
42	25	3.4	4000	42.38	23465.0	70	30	6.3	1000	23.60	366.4
42	30	3.4	50	4.81	41.5	70	30	6.3	2000	36.36	1337.8
42	30	3.4	200	5.94	257.3	70	30	6.3	3000	45.64	2816.4
42	30	3.4	500	10.54	855.8	70	30	8.4	50	5.86	1.9

s_L [mm]	s_T [mm]	δ [mm]	Re [-]	Nu [-]	Δp [Pa]	s_L [mm]	s_T [mm]	δ [mm]	L [mm]	Nu [-]	Δp [Pa]
42	30	3.4	750	14.01	1565.5	70	30	8.4	500	15.97	51.2
42	30	3.4	1000	17.06	2439.3	70	30	8.4	1000	27.08	173.0
42	30	3.4	1500	20.47	4420.7	70	30	8.4	2000	41.23	635.8
42	30	3.4	2000	24.43	6953.1	70	30	8.4	3000	50.71	1388.0
42	30	3.4	2500	28.06	9851.9	70	35	4.2	50	4.81	16.2
42	30	3.4	3000	31.44	13033.4	70	35	4.2	500	8.87	328.0
42	30	3.4	3500	34.48	16748.9	70	35	4.2	1000	16.04	1037.3
42	30	3.4	4000	37.42	21357.0	70	35	4.2	2000	27.19	3719.1
42	36	2.5	50	4.37	116.4	70	35	4.2	3000	33.13	7268.8
42	36	2.5	200	4.99	668.2	70	35	6.3	50	5.26	5.1
42	36	2.5	500	7.48	2113.9	70	35	6.3	500	12.58	124.8
42	36	2.5	750	10.47	3715.1	70	35	6.3	1000	22.99	441.7
42	36	2.5	1000	12.01	5652.6	70	35	6.3	2000	33.39	1447.0
42	36	2.5	1500	15.36	9897.2	70	35	6.3	3000	41.23	2836.2
42	36	2.5	2000	18.05	15081.6	70	35	8.4	50	6.71	7.7
42	36	2.5	2500	20.79	21089.8	70	35	8.4	500	13.17	115.9
42	36	2.5	3000	23.30	27926.8	70	35	8.4	1000	16.53	323.3
42	36	2.5	3500	25.67	35598.7	70	35	8.4	2000	29.27	990.9
42	36	2.5	4000	27.88	43908.0	70	35	8.4	3000	43.49	2061.0
42	36	3.4	50	4.51	48.5	70	36	3.4	50	4.49	31.0
42	36	3.4	200	5.29	275.7	70	36	3.4	100	5.34	66.3
42	36	3.4	500	9.28	920.2	70	36	3.4	200	6.72	155.0
42	36	3.4	750	12.13	1624.4	70	36	3.4	300	7.24	276.5
42	36	3.4	1000	14.27	2453.6	70	36	3.4	400	7.47	424.1
42	36	3.4	1500	18.12	4448.6	70	36	3.4	500	7.85	586.9
42	36	3.4	2000	21.74	6855.0	70	36	3.4	750	10.61	1091.9
42	36	3.4	2500	25.03	9706.8	70	36	3.4	1000	13.19	1750.5
42	36	3.4	3000	28.03	12925.1	70	36	3.4	1500	18.57	3514.6
42	36	3.4	3500	30.92	16580.6	70	36	3.4	2000	23.37	5839.4
42	36	3.4	3800	32.4	18824.1	70	36	3.4	2500	27.61	8723.8
42	36	3.4	4000	33.55	20657.4	70	36	3.4	3000	30.58	11867.1
42	36	4.2	50	4.62	27.3	70	36	3.4	3500	32.96	15162.6
42	36	4.2	200	6.04	160.4	70	36	3.4	3800	34.36	17381.4
42	36	4.2	500	10.84	536.6	70	36	3.4	4000	35.15	18775.7
42	36	4.2	750	13.81	955.7	77	20	4.2	50	5.20	11.0
42	36	4.2	1000	16.36	1455.3	77	20	4.2	500	11.35	165.4
42	36	4.2	1500	20.95	2667.0	77	20	4.2	1000	15.28	412.8
42	36	4.2	2000	25.12	4163.1	77	20	4.2	2000	24.7	1145.8
42	36	4.2	2500	28.85	5929.9	77	20	4.2	3000	33.78	2203.7
42	36	4.2	3000	32.30	7891.1	77	20	6.3	50	5.71	3.4
42	36	4.2	3500	35.48	10128.1	77	20	6.3	500	13.19	56.0
42	36	4.2	4000	38.39	12629.5	77	20	6.3	1000	19.89	146.9
42	36	6.3	50	4.86	9.0	77	20	6.3	2000	33.23	436.2
42	36	6.3	200	8.26	53.1	77	20	6.3	3000	43.79	834.6
42	36	6.3	500	14.17	190.1	77	20	8.4	50	6.22	1.5
42	36	6.3	750	17.84	343.2	77	20	8.4	500	15.10	26.5
42	36	6.3	1000	21.30	528.4	77	20	8.4	1000	24.56	73.0
42	36	6.3	1500	27.47	995.6	77	20	8.4	2000	40.00	220.7
42	36	6.3	2000	32.85	1573.1	77	20	8.4	3000	51.59	428.4

s_L [mm]	s_T [mm]	δ [mm]	Re [-]	Nu [-]	Δp [Pa]	s_L [mm]	s_T [mm]	δ [mm]	L [mm]	Nu [-]	Δp [Pa]
42	36	6.3	2500	38.37	2286.2	77	20	8.4	50	5.14	12.3
42	36	6.3	3000	42.23	3086.6	77	25	8.4	500	10.96	191.8
42	36	6.3	3500	46.00	3940.54	77	25	8.4	1000	14.79	531.7
42	36	6.3	4000	49.79	4933.7	77	25	8.4	2000	26.51	1688.8
42	36	8.4	50	5.10	4.2	77	25	8.4	3000	35.92	3212.5
42	36	8.4	200	10.40	25.0	77	25	6.3	50	5.59	3.8
42	36	8.4	500	17.00	92.9	77	25	6.3	500	12.61	66.6
42	36	8.4	750	21.89	172.0	77	25	6.3	1000	20.81	214.5
42	36	8.4	1000	26.27	269.4	77	25	6.3	2000	35.11	635.5
42	36	8.4	1500	33.95	512.7	77	25	6.3	3000	45.99	1243.3
42	36	8.4	2000	40.53	818.1	77	25	8.4	50	6.07	1.7
42	36	8.4	2500	46.40	1185.2	77	25	8.4	500	14.75	32.8
42	36	8.4	3000	51.70	1644.5	77	25	8.4	1000	25.55	107.0
42	36	8.4	3500	56.48	2125.4	77	25	8.4	2000	41.68	326.3
42	36	8.4	4000	61.02	2631.3	77	25	8.4	3000	52.93	668.7
42	40	3.4	50	4.23	52.8	77	30	4.2	50	5.03	13.8
42	40	3.4	200	5.11	290.1	77	30	4.2	500	10.11	228.9
42	40	3.4	500	8.78	946.5	77	30	4.2	1000	15.27	733.5
42	40	3.4	750	11.49	1656.7	77	30	4.2	2000	27.78	2490.5
42	40	3.4	1000	13.36	2464.4	77	30	4.2	3000	36.69	5065.0
42	40	3.4	1500	16.96	4463.3	77	30	6.3	50	5.49	4.2
42	40	3.4	2000	20.39	6897.5	77	30	6.3	500	11.96	87.6
42	40	3.4	2500	23.24	9697.7	77	30	6.3	1000	21.71	303.1
42	40	3.4	3000	26.03	12883.2	77	30	6.3	2000	35.78	997.6
42	40	3.4	3500	28.62	16451.2	77	30	6.3	3000	45.69	2152.7
42	40	3.4	4000	31.08	20400.1	77	30	8.4	50	5.92	1.9
42	45	3.4	50	4.07	56.6	77	30	8.4	500	15.48	45.9
42	45	3.4	200	4.86	297.9	77	30	8.4	1000	26.26	157.4
42	45	3.4	500	7.96	948.7	77	30	8.4	2000	41.92	512.1
42	45	3.4	750	10.23	1631.8	77	30	8.4	3000	53.23	1134.5
42	45	3.4	1000	12.25	2460.0	77	36	3.4	50	4.87	29.0
42	45	3.4	1500	15.35	4384.2	77	36	3.4	500	8.45	507.4
42	45	3.4	2000	18.89	6887.7	77	36	3.4	750	9.89	952.7
42	45	3.4	2500	21.13	9536.7	77	36	3.4	1500	17.98	3098.1
42	45	3.4	3000	23.71	12657.5	77	36	3.4	2000	23.92	5543.6
42	45	3.4	3500	26.19	16187.4	77	36	3.4	2500	28.42	8312.2
42	45	3.4	4000	28.59	20058.7	77	36	3.4	3000	31.79	11692.7
42	50	3.4	50	3.88	59.9	77	36	3.4	3500	34.80	14917.1
42	50	3.4	200	4.68	305.9	77	36	3.4	3800	35.98	17215.9
42	50	3.4	500	7.48	959.1	77	36	3.4	4000	37.11	18637.6
42	50	3.4	750	9.33	1641.2	84	20	4.2	50	5.12	10.6
42	50	3.4	1000	11.05	2437.0	84	20	4.2	500	11.05	155.7
42	50	3.4	1500	14.12	4399.6	84	20	4.2	1000	14.76	383.4
42	50	3.4	2000	16.96	6754.1	84	20	4.2	2000	22.97	1019.9
42	50	3.4	2500	19.55	9448.4	84	20	4.2	3000	30.78	1905.0
42	50	3.4	3000	22.96	12916.3	84	20	6.3	50	5.60	3.3
42	50	3.4	3500	25.12	16297.7	84	20	6.3	500	12.85	52.3
42	50	3.4	4000	27.16	19977.1	84	20	6.3	1000	18.75	133.9
45	30	3.4	50	4.93	38.5	84	20	6.3	2000	30.77	380.1

s_L [mm]	s_T [mm]	δ [mm]	Re [-]	Nu [-]	Δp [Pa]	s_L [mm]	s_T [mm]	δ [mm]	L [mm]	Nu [-]	Δp [Pa]
45	30	3.4	1000	16.01	2325.4	84	20	6.3	3000	40.90	723.1
45	30	3.4	2000	24.35	6701.0	84	20	8.4	50	6.09	1.5
45	30	6.3	50	5.56	7.0	84	20	8.4	500	14.57	24.6
45	30	6.3	1000	24.13	527.4	84	20	8.4	1000	22.98	65.5
45	30	6.3	2000	36.87	1500.1	84	20	8.4	2000	37.29	191.3
45	35	3.4	50	4.66	43.6	84	20	8.4	3000	48.47	367.3
45	35	3.4	1000	14.516	2354.8	84	25	4.2	50	5.08	11.7
45	35	3.4	2000	21.96	6606.9	84	25	4.2	500	10.79	177.2
45	35	6.3	50	5.08	78.0	84	25	4.2	1000	14.28	456.4
45	35	6.3	1000	21.54	509.3	84	25	4.2	2000	23.99	1443.8
45	35	6.3	2000	33.12	1508.8	84	25	4.2	3000	33.06	2687.6
45	40	3.4	50	4.43	48.1	84	25	6.3	50	5.50	3.6
45	40	3.4	1000	13.23	2343.7	84	25	6.3	500	12.46	60.6
45	40	3.4	2000	20.05	6504.7	84	25	6.3	1000	19.06	174.2
45	40	6.3	50	4.70	8.8	84	25	6.3	2000	32.45	533.5
45	40	6.3	1000	19.54	498.4	84	25	6.3	3000	42.79	1014.1
45	40	6.3	2000	30.10	1459.7	84	25	8.4	50	5.95	1.6
49	25	4.2	50	5.44	17.2	84	25	8.4	500	14.15	28.9
49	25	4.2	500	12.16	401.5	84	25	8.4	1000	23.81	90.2
49	25	4.2	1000	21.61	1412.1	84	25	8.4	2000	39.24	268.7
49	25	4.2	2000	31.29	4679.8	84	25	8.4	3000	50.14	520.0
49	25	4.2	3000	38.55	9149.9	84	30	4.2	50	5.03	12.9
49	25	6.3	50	6.04	5.5	84	30	4.2	500	10.34	203.9
49	25	6.3	500	17.36	162.8	84	30	4.2	1000	14.03	608.9
49	25	6.3	1000	27.22	577.0	84	30	4.2	2000	25.77	2023.9
49	25	6.3	2000	39.41	1878.7	84	30	4.2	3000	34.61	3994.2
49	25	6.3	3000	49.23	3772.8	84	30	6.3	50	5.42	4.0
49	25	8.4	50	6.59	2.5	84	30	6.3	500	11.73	72.6
49	25	8.4	500	20.99	87.2	84	30	6.3	1000	20.00	247.7
49	25	8.4	1000	32.08	303.2	84	30	6.3	2000	33.81	766.9
49	25	8.4	2000	46.41	997.2	84	30	6.3	3000	43.87	1543.9
49	25	8.4	3000	56.96	1972.8	84	30	8.4	50	5.83	1.8
49	30	4.2	50	5.15	19.86	84	30	8.4	500	14.01	37.7
49	30	4.2	500	11.50	452.2	84	30	8.4	1000	24.72	123.4
49	30	4.2	1000	19.01	1378.1	84	30	8.4	2000	40.18	399.3
49	30	4.2	1000	19.01	1378.1	84	30	8.4	2000	40.18	399.3
49	30	4.2	2000	27.51	4191.8	84	30	8.4	3000	50.64	787.4
49	30	4.2	3000	34.12	8042.1	84	36	3.4	200	6.41	128.6
49	30	6.3	50	6.00	6.2	84	36	3.4	500	9.14	434.9
49	30	6.3	500	15.60	165.0	84	36	3.4	750	9.73	818.2
49	30	6.3	1000	23.86	512.1	84	36	3.4	1500	16.79	2691.2
49	30	6.3	2000	34.70	1571.9	84	36	3.4	2000	22.22	4727.5
49	30	6.3	3000	43.84	3073.3	84	36	3.4	2500	26.73	7045.7
49	30	8.4	50	7.29	9.1	84	36	3.4	3000	30.72	9790.8
49	30	8.4	500	12.74	163.7	84	36	3.4	3500	34.41	12975.2
49	30	8.4	1000	19.05	443.6	84	36	3.4	3800	36.36	15208.9
49	30	8.4	2000	35.85	1338.9	84	36	3.4	4000	37.74	16636.4
49	30	8.4	3000	48.61	2585.2	91	20	4.2	50	5.04	10.2
49	35	4.2	50	4.85	22.3	91	20	4.2	500	10.73	147.6

s_L [mm]	s_T [mm]	δ [mm]	Re [-]	Nu [-]	Δp [Pa]	s_L [mm]	s_T [mm]	δ [mm]	L [mm]	Nu [-]	Δp [Pa]
49	35	4.2	500	10.77	479.3	91	20	4.2	1000	14.29	358.6
49	35	4.2	1000	16.92	1363.5	91	20	4.2	2000	21.68	926.0
49	35	4.2	2000	24.62	3955.36	91	20	4.2	3000	28.87	1691.6
49	35	4.2	3000	30.78	7463.3	91	20	6.3	50	5.49	3.17
49	35	6.3	50	5.19	7.3	91	20	6.3	500	12.51	49.3
49	35	6.3	500	14.44	175.3	91	20	6.3	1000	17.82	123.3
49	35	6.3	1000	21.59	508.4	91	20	6.3	2000	28.94	338.2
49	35	6.3	2000	31.57	1503.8	91	20	6.3	3000	38.24	632.6
49	35	6.3	3000	40.14	2895.76	91	20	8.4	50	5.95	1.4
49	35	8.4	50	5.50	3.4	91	20	8.4	500	14.09	22.9
49	35	8.4	500	17.57	87.1	91	20	8.4	1000	21.76	59.4
49	35	8.4	1000	25.87	256.8	91	20	8.4	2000	35.05	168.5
49	35	8.4	2000	38.76	779.3	91	20	8.4	3000	45.67	319.12
49	35	8.4	3000	49.83	1530.0	91	25	4.2	50	5.00	11.25
49	36	3.4	50	4.66	41.9	91	25	4.2	500	10.56	165.1
49	36	3.4	100	5.26	98.84	91	25	4.2	1000	13.92	412.45
49	36	3.4	200	5.55	250.0	91	25	4.2	2000	22.00	1175.7
49	36	3.4	300	6.32	418.0	91	25	4.2	3000	30.48	2244.7
49	36	3.4	400	7.67	623.8	91	25	6.3	50	5.39	3.5
49	36	3.4	500	9.03	847.7	91	25	6.3	500	12.23	55.7
49	36	3.4	750	12.03	1538.9	91	25	6.3	1000	17.56	146.3
49	36	3.4	1000	14.43	2337.2	91	25	6.3	2000	30.06	445.4
49	36	3.4	1500	18.48	4284.5	91	25	6.3	3000	40.18	837.3
49	36	3.4	2000	21.89	6635.9	91	25	8.4	50	5.83	1.5
49	36	3.4	2500	25.07	9339.9	91	25	8.4	500	13.75	26.2
49	36	3.4	3000	28.09	12529.4	91	25	8.4	1000	21.99	73.1
49	36	3.4	3500	30.90	16000.6	91	25	8.4	2000	36.57	220.8
49	36	3.4	3800	32.50	18324.7	91	25	8.4	3000	47.57	425.3
49	36	3.4	4000	33.46	19816.8	91	30	4.2	50	4.96	12.3
50	30	3.4	50	4.94	35.3	91	30	4.2	500	10.26	185.4
50	30	3.4	1000	16.05	2209.0	91	30	4.2	1000	13.30	493.7
50	30	3.4	2000	24.99	6543.6	91	30	4.2	2000	23.47	1671.6
50	30	6.3	50	5.64	6.25	91	30	4.2	3000	32.54	3136.1
50	30	6.3	1000	24.51	508.55	91	30	6.3	50	5.33	3.78
50	30	6.3	2000	36.87	1544.6	91	30	6.3	500	11.76	63.8
50	35	3.4	50	4.72	39.7	91	30	6.3	1000	18.30	203.45
50	35	3.4	1000	14.50	2261.6	91	30	6.3	2000	31.69	609.5
50	35	3.4	2000	22.13	6398.0	91	30	6.3	3000	42.12	1212.3
50	35	6.3	50	5.23	7.14	91	30	8.4	50	5.65	1.7
50	35	6.3	1000	21.73	493.1	91	30	8.4	500	13.24	30.9
50	35	6.3	2000	33.13	1458.5	91	30	8.4	1000	23.03	102.3
50	40	3.4	50	4.53	43.9	91	30	8.4	2000	39.07	314.98
50	40	3.4	1000	13.32	2274.7	91	30	8.4	3000	39.07	314.98
50	40	3.4	2000	20.12	6314.5	91	36	3.4	50	4.74	25.8
50	40	6.3	50	4.87	7.9	91	36	3.4	200	6.25	119.4
50	40	6.3	1000	19.66	484.3	91	36	3.4	500	9.38	387.4
50	40	6.3	2000	30.16	1414.2	91	36	3.4	1500	15.42	2242.2
56	25	4.2	50	5.35	15.4	91	36	3.4	2500	24.92	5678.8
56	25	4.2	500	10.93	327.3	91	36	3.4	3000	28.65	7750.4

s_L [mm]	s_T [mm]	δ [mm]	Re [-]	Nu [-]	Δp [Pa]	s_L [mm]	s_T [mm]	δ [mm]	L [mm]	Nu [-]	Δp [Pa]
56	25	4.2	1000	20.66	1179.0	91	36	3.4	3500	32.23	10069.2
56	25	4.2	2000	31.71	4164.1	91	36	3.4	4000	35.51	12886.1
56	25	4.2	3000	39.45	8740.9	112	20	4.2	50	4.87	9.58
56	25	6.3	50	5.94	4.9	112	20	4.2	500	9.97	132.7
56	25	6.3	500	15.81	131.2	112	20	4.2	1000	13.29	316.2
56	25	6.3	1000	26.37	473.5	112	20	4.2	2000	19.06	784.4
56	25	6.3	2000	39.07	1711.2	112	20	4.2	3000	25.03	1385.4
56	25	6.3	3000	48.91	3573.5	112	20	6.3	50	5.26	2.9
56	25	8.4	50	6.78	2.2	112	20	6.3	500	11.68	43.8
56	25	8.4	500	19.16	68.1	112	20	6.3	1000	15.98	106.3
56	25	8.4	1000	30.00	238.9	112	20	6.3	2000	25.06	276.5
56	25	8.4	2000	45.14	867.2	112	20	6.3	3000	32.99	501.7
56	25	8.4	3000	57.51	1771.9	112	20	8.4	50	5.67	1.3
56	30	4.2	50	5.13	17.5	112	20	8.4	500	13.07	20.2
56	30	4.2	500	10.73	391.9	112	20	8.4	1000	18.94	50.1
56	30	4.2	1000	19.23	391.9	112	20	8.4	2000	30.41	134.9
56	30	4.2	2000	28.52	4147.4	112	20	8.4	3000	39.64	248.1
56	30	4.2	3000	34.73	7982.5	112	25	4.2	50	4.79	9.2
56	30	6.3	50	5.64	5.6	112	25	4.2	500	9.43	125.1
56	30	6.3	500	15.26	152.5	112	25	4.2	1000	12.53	300.8
56	30	6.3	1000	24.85	515.4	112	25	4.2	2000	17.60	757.6
56	30	6.3	2000	35.61	1618.9	112	25	4.2	3000	22.97	1350.7
56	30	6.3	3000	44.15	3167.25	112	25	6.3	50	5.09	2.8
56	30	8.4	50	6.13	2.5	112	25	6.3	500	11.06	41.37
56	30	8.4	500	19.25	80.5	112	25	6.3	1000	14.86	101.7
56	30	8.4	1000	29.31	270.1	112	25	6.3	2000	23.05	269.0
56	30	8.4	2000	42.68	862.1	112	25	6.3	3000	30.86	496.7
56	30	8.4	3000	53.29	1730.9	112	25	8.4	50	5.43	1.2
56	35	4.2	50	6.45	70.7	112	25	8.4	500	12.32	19.1
56	35	4.2	500	9.61	968.3	112	25	8.4	1000	17.45	48.0
56	35	4.2	1000	11.68	2532.4	112	25	8.4	2000	28.39	132.5
56	35	4.2	2000	17.31	6833.2	112	25	8.4	3000	37.73	247.5
56	35	4.2	3000	25.00	12674.4	112	30	4.2	50	4.77	9.86
56	35	6.3	50	5.31	6.3	112	30	4.2	500	9.32	135.3
56	35	6.3	500	14.16	162.5	112	30	4.2	1000	12.28	331.3
56	35	6.3	1000	22.22	493.7	112	30	4.2	2000	17.29	868.5
56	35	6.3	2000	31.92	1482.8	112	30	4.2	3000	23.27	1682.3
56	35	6.3	3000	39.80	2843.6	112	30	6.3	50	5.05	3.0
56	35	8.4	50	5.70	2.9	112	30	6.3	500	10.91	45.1
56	35	8.4	500	17.66	82.3	112	30	6.3	1000	14.61	113.9
56	35	8.4	1000	26.35	251.6	112	30	6.3	2000	23.26	329.4
56	35	8.4	2000	38.56	769.6	112	30	6.3	3000	32.04	627.6
56	35	8.4	3000	48.74	1510.37	112	30	8.4	50	5.37	1.3
56	36	3.4	50	4.63	37.5	112	30	8.4	500	12.13	20.9
56	36	3.4	100	5.14	83.9	112	30	8.4	1000	17.19	54.8
56	36	3.4	200	6.32	221.3	112	30	8.4	2000	29.239	166.5
56	36	3.4	300	6.61	393.7	112	30	8.4	3000	39.06	310.5
56	36	3.4	400	7.53	582.1	112	36	3.4	50	4.68	22.9
56	36	3.4	500	8.98	778.5	112	36	3.4	200	5.67	102.4

s_L [mm]	s_T [mm]	δ [mm]	Re [-]	Nu [-]	Δp [Pa]	s_L [mm]	s_T [mm]	δ [mm]	L [mm]	Nu [-]	Δp [Pa]
56	36	3.4	750	11.87	1423.6	112	36	3.4	500	8.86	312.8
56	36	3.4	1000	14.42	2205.5	112	36	3.4	750	10.59	532.8
56	36	3.4	1500	18.90	4144.6	112	36	3.4	1000	11.65	780.9
56	36	3.4	2000	22.44	6445.7	112	36	3.4	1500	13.64	1421.9
56	36	3.4	2500	25.48	9128.3	112	36	3.4	2000	15.88	2257.3
56	36	3.4	3000	28.34	12072.4	112	36	3.4	2500	18.68	3212.7
56	36	3.4	3500	31.02	15599.6	112	36	3.4	3000	22.23	4538.9
56	36	3.4	3800	32.58	17854.8	112	36	3.4	3500	25.65	5947.2
56	36	3.4	4000	33.53	19349.0	112	36	3.4	3800	28.28	7078.7
63	25	4.2	50	5.22	14.1	112	36	3.4	4000	29.23	7534.9

Acknowledgements

The present dissertation arose during my activity as a scientific coworker at the Institute of Thermal Process Engineering and Plant Technology, University of Paderborn, Germany. Thereby I was supported by many persons and at this place I want to express my gratitude to all of them.

First of all, I would like to thank my supervisor, Prof. Dr.-Ing Jovan Mitrović, for his comprehensive support, motivating discussions, encouragement and kindly help, not only concerning the work at the Insitute, but also in everyday life. He was able to recognise my professional abilities and helped its further developing.

Dr.rer.nat. Henning Raach iducted me into the world of Computational Fluid Dynamics and I would like to thank him for his generous support, kindness and friendliness.

I am grateful to the Ms. Rong Fan, Ms. Yan Li, Mr. Philipp Grimm and Mr. Waldemar Heckel and Mr. Azer Nazdrajić, who chose the Computational Fluid Dynamics as a subject of their bachelor's thesis and student research projects and me as their tutor. A number numerical experiments that were used for creating the Nusselt number correlation in this thesis were conducted by them.

Further, I gratefully acknowledge the help that I recieved from all my colleagues, scientific coworkers, secretaries and technical staff from the Institute. Especially I would like to thank Mr. Axel Keller from PC^2 Paderborn center for parallel computing.

Furthermore, I would like to mention all my schoolteachers and university professors who taught me during my education, especially Prof. Dr.-Ing. Branislav B. Bačlić, from the University of Novi Sad, Serbia.

And last but not least I would like to thank my wife Sladjana and my sons Darko und Oliver for their continuous support and encouragement, in spite of the long periods of my absence they had to put up with.

Paderborn, July 2008

Boban Maletić